A Comparison of Data Fusion Techniques for Target Detection with a Wide Azimuth Sonar

by

Kent Russell Engebretson

B.S., Electrical Engineering
United States Air Force Academy
(1993)

Submitted to the Department of
ELECTRICAL ENGINEERING AND COMPUTER SCIENCE
In Partial Fulfillment of the Requirements
For the Degree of

MASTER OF SCIENCE
at the

MASSACHUSETTS INSTITUTE OF TECHNOLOGY
May, 1995

Signature of Author: _____
Department of Electrical Engineering and Computer Science
May, 1995

Certified by: _____
Kenneth M. Houston
Principal Member of Technical Staff, C. S. Draper Laboratory
Technical Supervisor

Certified by: _____
Dr. Dan E. Dudgeon
Lincoln Laboratory
Thesis Supervisor

Accepted by: _____
Professor F. R. Morgenthaler
Chairman Departmental Graduate Committee

A Comparison of Data Fusion Techniques for Target Detection with a Wide Azimuth Sonar

by

Lieutenant Kent Russell Engebretson, United States Air Force

B.S., Electrical Engineering
United States Air Force Academy
(1993)

Submitted to the
Department of Electrical Engineering and Computer Science
in partial fulfillment of the requirements
for the degree of
Master of Science

Abstract

A group at the Charles Stark Draper Laboratory developed a concept for a mine reconnaissance platform called Intelligent Sonobuoy. This platform utilizes a low frequency sonar with wide aspect angle coverage. Furthermore the platform is designed to drift past an area of interest and thus obtain multiple detections from each sonar target. This thesis examines methods of fusing together those detections into a composite map of the target field in order to detect and localize those sonar targets.

A technique based on hypothesis testing and maximum likelihood estimation is first derived and then applied to simulated data. Lastly, the system is validated on actual test data obtained in Mendum's Pond, New Hampshire during the summer and Fall of 1994. This system is shown to be effective at resolving targets to within a few meters.

A competing approach based on the Hough transform is next examined. This clustering technique is applied to find the change in target location with respect to the buoy's position. The system works for simulated test data with a small number of detections. System performance declines rapidly as the number of detections increases and the system does not work well with the actual test data.

Thesis Supervisor:	Dr. Dan Dudgeon Lincoln Laboratory
Company Supervisor:	Kenneth M. Houston Draper Laboratory

Acknowledgment

May 12, 1995

This thesis was prepared at the Charles Stark Draper Laboratory, Inc., under CSR Project number C - 318.

Acknowledgments

First and foremost, I would like to thank my immediate supervisor, Ken Houston. He kept me from straying too far from the beaten path and helped me up when I stumbled. Without him, this thesis would not have been possible.

I would also like to thank my MIT advisor, Dr. Dan Dudgeon. His insight gave me many new ideas as I hit dead ends in my research.

I need to also thank the rest of the Intelligent Sonobuoy group, especially: Mark Dzwonczyk, who first brought me here and then left the day after I arrived; Michael LeBlanc, although he almost transformed me into a C programmer against my will; Pete Kerrebrock, who hefted many pounds of equipment with me from the bottom of Mendum's pond; and last, but not least, our fearless leader, Shawn Burke whose incredible drive and leadership skills continue to amaze me.

In addition to all this intellectual support, I also would have been lost without all the emotional support I received along the way. The guys at 13 Bigelow have always been there for me and it was a wonderful home away from home. My real family in Wisconsin, though separated by miles, are always with me in spirit and I knew that I always had their love and support. Lastly I would like to thank Rebecca, the love of my life, whose constant messages meant more than she could possibly know.

Above all, I would like to thank my Lord and Savior who has taught me humility and diligence along this difficult journey, but has walked with me every step of the way.

Contents

List of Figures

List of Tables

1. Introduction

Due to a changing global political environment, the U.S. Navy has placed an increased importance on mine warfare. The collapse of the Soviet Union has led to a increased number of regional conflicts for which the U.S. Warfare Strategy must adapt. [1] A new emphasis has been placed on power projection and the ability to fight in smaller scale, conventional conflicts such as Operation Desert Storm in Southwest Asia. Military downsizing has caused a removal of overseas assets and an increased dependence on power projection. One such method of power projection deemed important by military authorities is that of Marine Expeditionary Warfare. The ability to transport troops and place them on a hostile shore is an important option for military planners as the number of overseas military bases continues to decrease. Integral to the success of Marine Expeditionary Warfare is the concept of mine warfare, which includes both offensive mining and mine countermeasures.

Operation Desert Storm in early 1991 demonstrated glaring deficiencies in mine warfare and particularly in mine countermeasures (MCM). The presence of approximately 1,300 Iraqi mines interspersed throughout the Persian Gulf eliminated the possibility of any plans for an amphibious operation. Furthermore on 17 February 1991, a $25K magnetic-acoustic mine caused $15M of damage to the Aegis cruiser, USS Princeton. [2] In response to these shortcomings the U.S. Navy has placed an increased emphasis on mine-countermeasures, especially in littoral, or coastal, environments. [1]

Conventional mine-hunting techniques use sophisticated ship-board sonar systems to detect mines. A need for more rapid response has recently led to development of helicopter-based mine reconnaissance. A major problem with these methods is that they are risky and involve placing human assets near a potentially hostile coast. These conventional systems have a very low area coverage rate which increases the time needed to search a potential minefield. The area coverage rate drops even lower in littoral environments, so human operators are in a dangerous position for an even longer period of time.

Based on the above reasons, the top priority in the U.S. Navy Mine Warfare Plan is to " . . . develop a clandestine mine surveillance, reconnaissance, and detection capability that uses a variety of systems to provide knowledge of the full dimensions of the mine threat without exposing the reconnaissance platforms." [1]

1.1 Thesis Motivation

Internal research done at the Charles Stark Laboratory has been directed at creating a platform to safely, rapidly, and effectively detect, localize and classify mines in a littoral environment. The overall conceptual approach involves deploying a set of sonobuoys with a surface craft or low-flying helicopter. The buoys then drift through the area of interest, such as a known minefield or an intended assault location. The buoys contain on-board processing ability necessary to obtain sonar detections. A GPS-based navigational system determines the track of the buoy. The resulting list of detections and position data is relayed to a host ship or aircraft via an RF link where a global map of the sonar environment is created. The area coverage rate is greatly enhanced through the use of many buoys and the inherent drifting of the buoys through the area of interest. Overlapping coverage helps ensure multiple detections of the sonar targets. The host platform then performs additional processing to convert lists of detections from the individual buoys into a global map of the target field. Finally, planning software determines safe areas or areas in which to concentrate conventional mine-sweeping assets.

The baseline sonobuoy concept uses a conventional SSQ-62 buoy which has proven successful in anti-submarine warfare. The original buoys are modified to include a cylindrical receive array. The on-board processing in the buoys performs matched-filtering, beamforming, and other signal processing operations necessary to detect targets. An characteristic of the sonar system is that while the sonar detections have relatively good range accuracy, the angle resolution is limited to knowledge of the beam in which the detection was made. With 32 beams comprising 360 degree coverage, the angle resolution is

equal to 11.25 degrees. Further signal processing has provided a monopulse estimate which improves on that angle resolution.

1.2 Problem Statement

The goal of this research is to examine methods to localize sonar targets from the detection list. This list contains the ping number, beam, range, SNR, and monopulse estimate. The location of the sonobuoy at each ping is also known. The core problem becomes one of data fusion. As the buoy drifts past a sonar target, multiple detections of the object are observed. This allows an inherent integration gain which may improve the signal to noise ratio and reduce the probability of a false alarm. The overall idea is similar to that of a synthetic aperture radar (SAR). A breakdown in the similarity occurs because of the fundamental importance of phase information to SAR which is lost in the sonar environment. Experiments using synthetic aperture sonar have been impractical because of this dependence on phase. Therefore, incoherent methods must be adopted. The sonobuoy at each ping location can be considered a separate sensor which is both spatially and temporally separated from the other sensors. These sensors thus are independent and identical. In essence the problem has become how to best utilize the overlap in detection data given the constraints regarding the accuracy of detection data and position data, as well as the loss of phase information.

1.3 Overview of Analysis

This study begins by describing the Intelligent Sonobuoy project. The design of the sonobuoy defines the various constraints imposed on target detection and localization. The background places particular emphasis on those subsystems which have direct implications on target localization. In particular, the sonar characteristics, signal processing, and the role of map building receive specific consideration.

A prototype sonobuoy designed and constructed at Draper Laboratory was tested during the summer and fall of 1994. Information about the

prototype is provided as needed to comprehend the data composition. The data itself is analyzed next. The types of errors inherent to the system affect the design of target localization algorithms. This section discusses the errors inherent in range, azimuth angle, and buoy position.

Various techniques for localizing targets are presented in section 3, and comprise the bulk of the thesis. Discussion of these techniques includes a brief background behind the theory of the algorithm and its application to this problem.

After all of the algorithms have been introduced, the various advantages and disadvantages of the procedures are discussed. Comparisons are made based on accuracy, resilience to noise, and target resolution.

2. Background

The Intelligent Sonobuoy project was formulated as a direct response to the deficiencies in current mine countermeasure (MCM) capabilities. This concept is "different from other minefield reconnaissance concepts currently being developed for the U.S. Navy. . . ." [3] The Intelligent Sonobuoy concept addresses those deficiencies by creating a low-cost platform for mine reconnaissance which provides a higher area coverage rate and lower threat to human assets than conventional mine hunting techniques.

2.1 Intelligent Sonobuoy System Concept

The Intelligent Sonobuoy concept entails using a set of sonobuoys for mine reconnaissance. The mission concept is depicted pictorially in Figure 2-1. Information about ocean currents and the physical geometry of the area of interest is first gathered. Planning software on the host platform then determines the seeding pattern for the buoys based on this information so that full coverage of the target field is obtained. A set of sonobuoys are then deployed according to this seeding pattern. The sonobuoys are based on conventional, SSQ-62 buoys used for anti-submarine warfare so traditional deployment platforms such as helicopters or surface ships may be utilized. Unlike conventional MCM methods, these assets are only required during the deployment process.

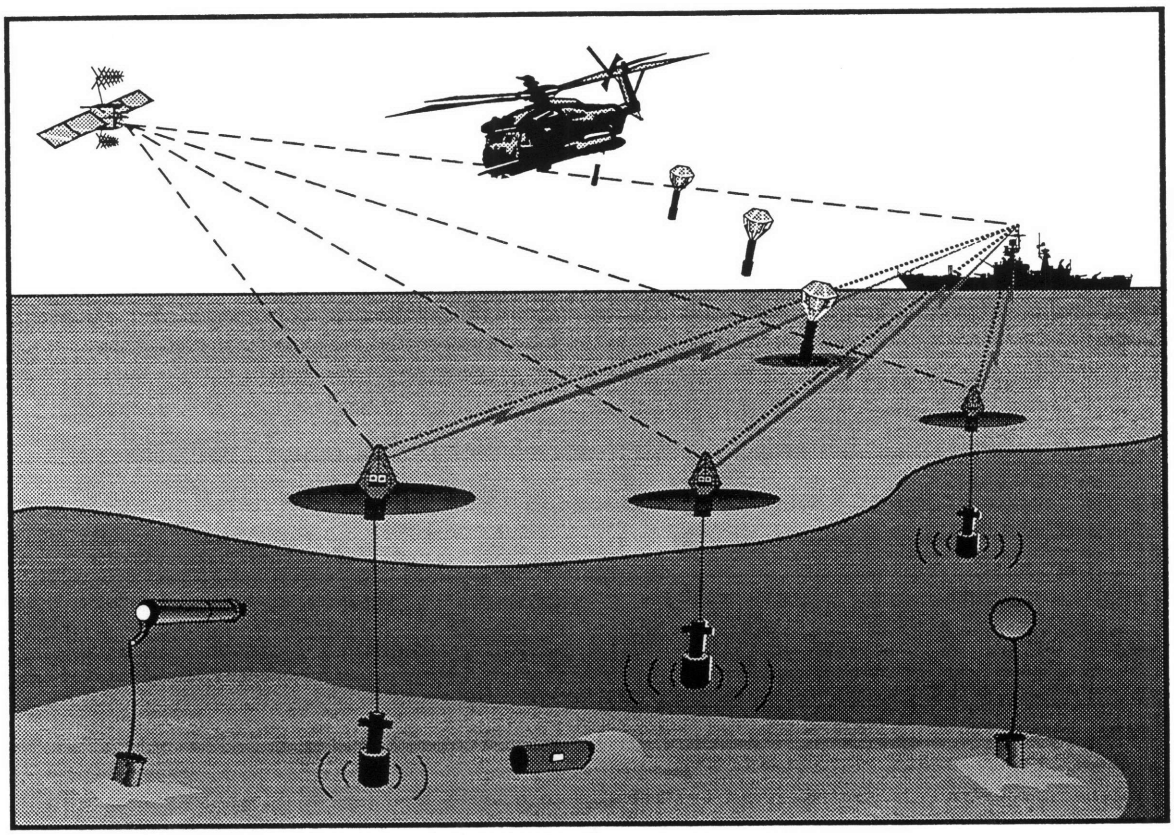

Figure 2-1 Intelligent Sonobuoy Mission Concept

After splashdown, floats inflate and the sonar arrays lower on wave motion-isolating tethers. Each buoy contains a wide-bandwidth omni-directional projector array, wide-bandwidth multibeam receive array, compass, depth sensor, batteries, analog signal conditioning, and digital processing subsystems in the underwater section. An RF link, antenna, CA-code GPS receiver, and differential GPS receiver reside in the float.

The buoys drift through the target field for up to eight hours, depending on battery life. The projector array sends out coded pseudo-random noise transmissions which reduces mutual interference between buoys. This also enables multistatic operation whereby a sonobuoy utilizes the sonar transmissions from nearby sonobuoys as well as its own. The multibeam receive array obtains sonar returns from the reflected transmissions. On-board processing creates detections from these returns, while the GPS receivers determine the sonobuoy's track. At periodic intervals, the detection list and navigation data are transferred to the host platform through the RF

link. At the end of the mission, a software scuttle ensures security in case enemy forces capture the buoy. The sonobuoys may then be recovered and later programmed for reuse.

2.1.1 Sonar Characteristics

The characteristics of the sonar projector array and receiver array greatly affect detection performance. The sonar projector is consistent with the existing AN/SSQ-62 sonobuoy. A 21 degree nominal vertical beamwidth was chosen to illuminate the horizontal plane and reduce the effects of multipath reflections. The vertical beamwidth thus determines the minimum detection radius on the sea bottom. The appropriate geometry illustrating this point is shown in Figure 2-2.

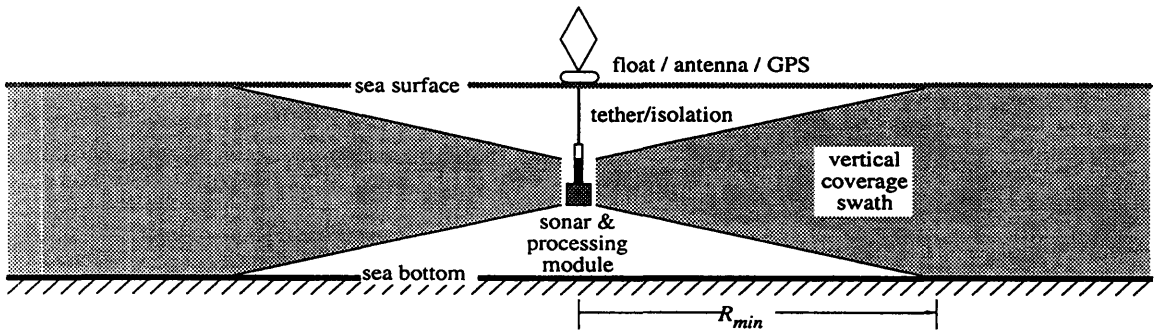

Figure 2-2 Horizontal View of Sonobuoy in Operation

The transmission blanking interval also affects the minimum range. The sonar array does not receive signals while pings are transmitted, so the length of the active transmission introduces a period of silence in the sonar return. Once the transmission blanking interval is over, the minimum range is defined by the geometry shown in Figure 2-2. Sonar characteristics and the water medium the signals are propagating through both affect the maximum range.

The wide-bandwidth, multibeam receive array is unique among sonar receivers currently in use. The fully-populated array contains 16 staves constructed of poly-vinylidene fluoride (PVDF) material. These receive staves are shaded vertically to provide the same vertical beamwidth as the projector.

Groups of 5 or 6 staves are combined during beamforming to create 32 overlapping beams with 17 degree beamwidths and 11.25 degree separation between centers. [4] The angle estimate to target is determined solely by beam number. Strong detections may appear in multiple beams.

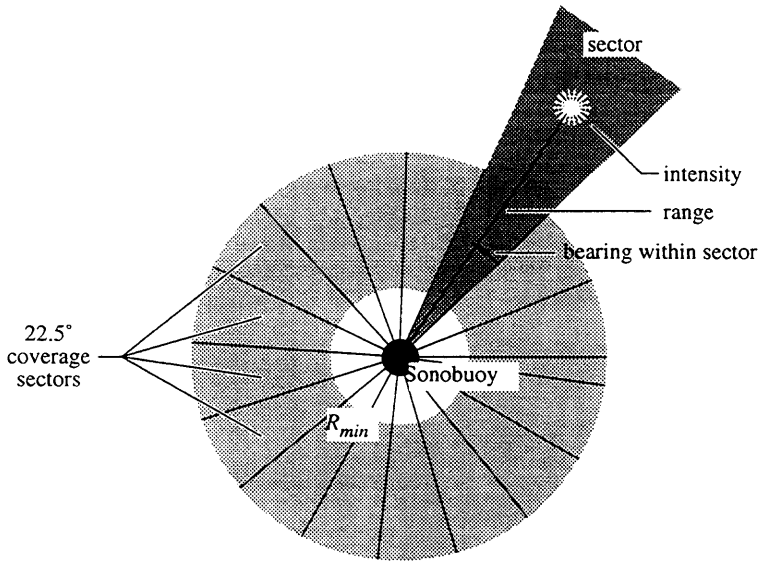

Figure 2-3 Top View Showing 360 Degree Coverage

Another important characteristic of the Intelligent Sonobuoy sonar concept is multi-aspect operation. Figure 2-4 shows a plot of the relative target positions with respect to the buoy's reference frame. This plot shows that the target is within the sonobuoys field of view for many ping cycles. Conceivably, each location could result in a detection, depending on the target geometry and other factors. In comparison, an ideal side-scan sonar will ensonify a point target only once. For Intelligent Sonobuoy, multiple detections of the same target, in essence, allows the target to be tracked within the field of view. The multiplicity of detections provides an incoherent integration gain which may be used to significantly lower the false-alarm rate.

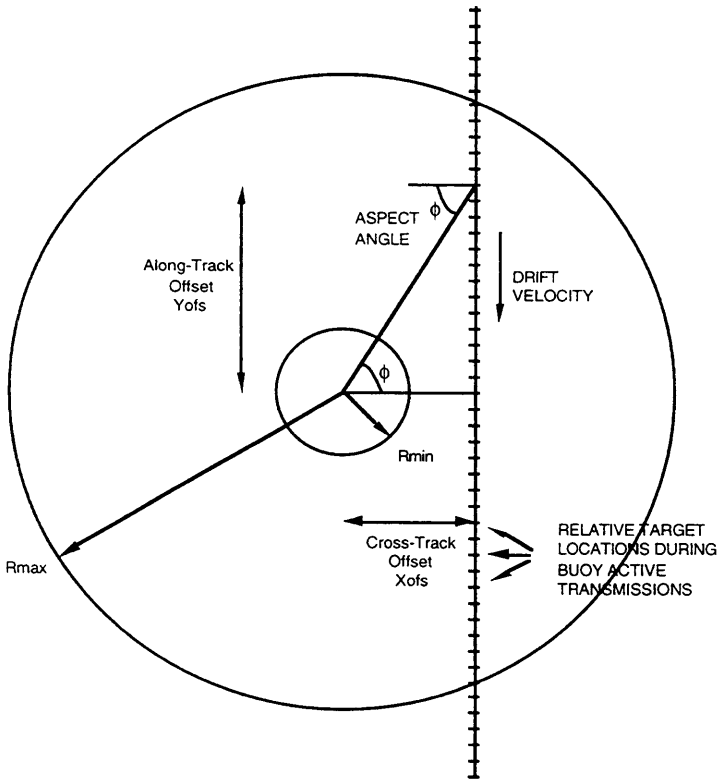

Figure 2-4 Top view of Buoy Drift Geometry With Respect to Target

Aspect angle coverage refers to the total range of aspect angles as a sonobuoy drifts by an target. The number of possible detections is determined by the minimum and maximum ranges of the sonar and also by the cross-track offset. The variation of aspect angle as a function of cross-track offset is shown in Figure 2-5. This figure shows that for a cross track offset of 500 meters, the aspect angle coverage is 120 degrees, while at 100 meters, the coverage increases to 170 degrees. In comparison, side-scan sonars may have a coverage rate of only 90 degrees or less.

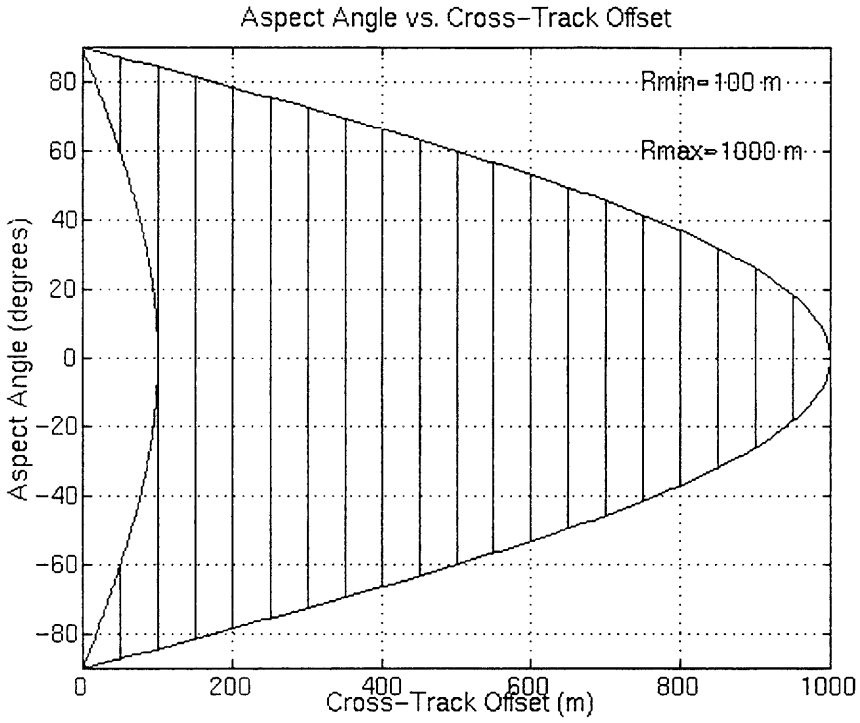

Figure 2-5 Aspect Angle vs. Cross Track Offset

A high rate of aspect angle coverage can be very important in obtaining high target returns. Certain sonar targets display a high level of aspect angle dependency. This is especially true of man-made objects which commonly have right angles and flat surfaces. An example of this phenomenon may be observed with a cylindrical target. Cylinders are characterized by strong detections reflected from the sides and end-caps. This property is readily observed in Figure 2-6. This figure shows the measured free-field target strength for a mine-like shaped cylinder at 10 KHz. [5] The peak values of the target strength in this plot are approximately -6 dB and the target strength beamwidths are about 8°. It is interesting to note that the plot is asymmetric and that there are only 3 main lobes instead of 4.

A sonar with narrow aspect angle coverage, such as a side-scan sonar, would need to be designed to make detections at -25 dB target strength. Intelligent Sonobuoy, on the other hand, has a much higher rate of coverage. In fact, by seeding the buoys such that they are placed at half the maximum range of the sonar, upwards of 320 degree coverage may be obtained. This

makes detecting sonar targets much easier because there is a high probability of at least one detection on a main lobe. The sonar thus may be designed to make detections at a much higher target strength than would be necessary with lower aspect angle coverage.

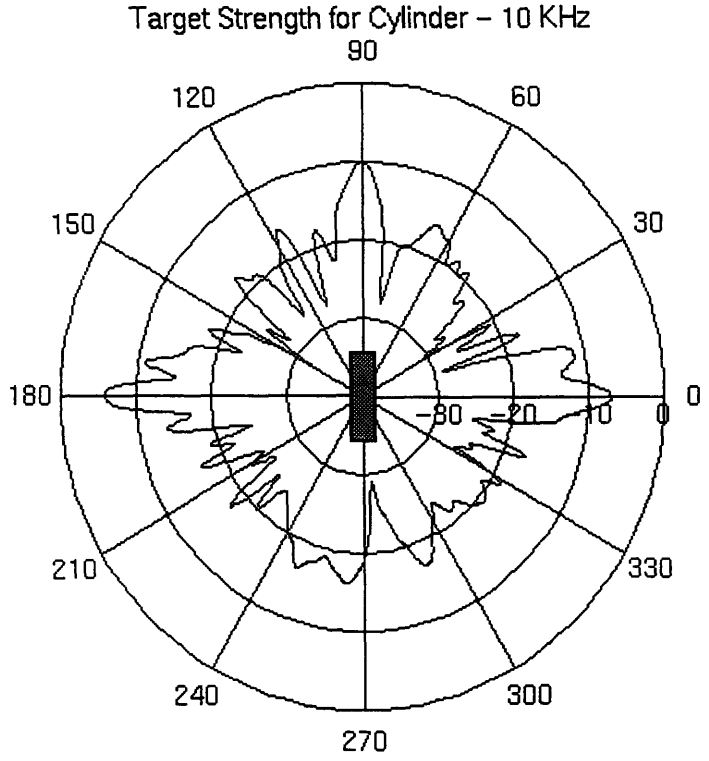

Figure 2-6 Target Strength for Cylinder at 10 KHz

The aspect angle granularity refers to the increment in aspect angles between consecutive pings. In order to make a detection, the target strength of the object must exceed a given threshold and the sonar has to sample the target strength while it exceeds the threshold. In essence, the aspect angle granularity is interpreted as the sampling rate as a function of angle. Ideally, the granularity is fine enough so that the specular lobes in the return are detected.

A plot of aspect angle granularity appears in Figure 2-7. This plot shows that the granularity is typically below one degree. The worst case scenario of nearly 6 degrees only appears for small cross track distances at

their closest point of approach. The target strength beamwidth of the cylinder is approximately 8 degrees, so this value is more than adequate.

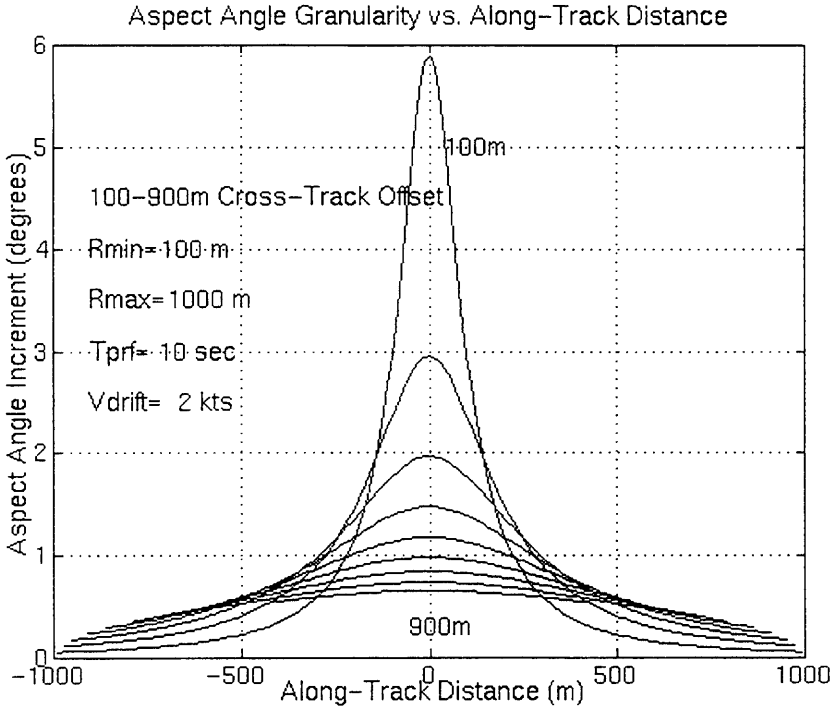

Figure 2-7 Aspect Angle Granularity

2.1.2 Signal Processing

Signal processing converts raw sonar receive data into detections. Both analog and digital signal processing are used to derive the low-level target returns from the much higher levels of background noise. The analog signal processing is first performed after the signals are received. As shown in Figure 2-8, the analog signal processing consists of: pre-amplification, time-varying gain (TVG) emphasis, anti-alias filtering, and A/D conversion. The time-varying gain boosts weaker signals which occur later in the return data.

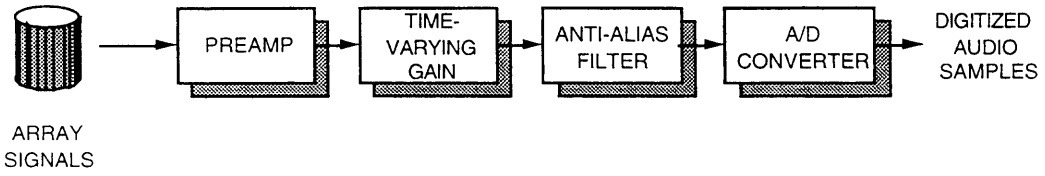

Figure 2-8 Analog Signal Processing

After the signal conditioning has been performed, a series of digital processing techniques are used to extract detections from the data. These techniques include gain compensation, matched filtering, beamforming, demodulation, energy detection, reverberation estimation and normalization, thresholding, and monopulse angle estimation. The goal is to obtain a list of detections with a signal energy much higher than the background noise.

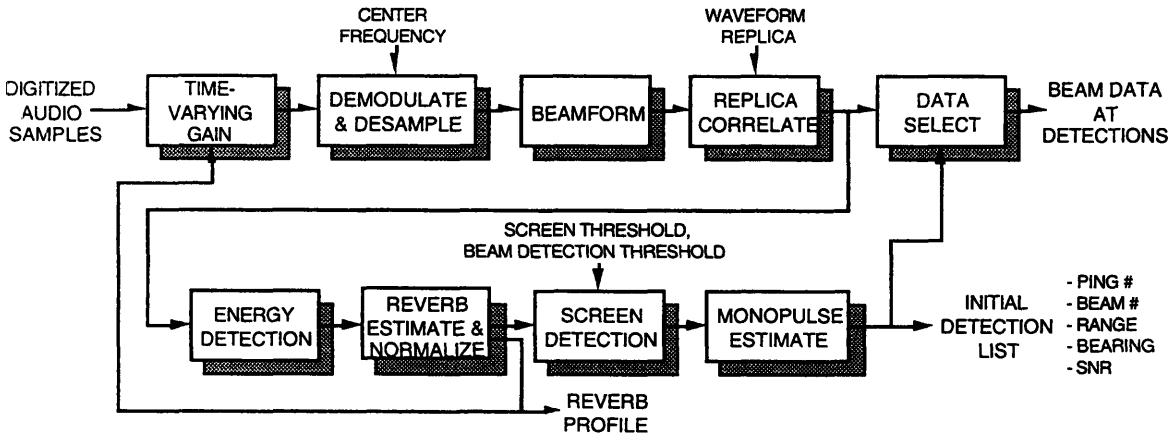

Figure 2-9 Digital Signal Processing and Energy Detection

2.1.3 Map Generation

The ultimate goal of the entire system is to transform the list of detections provided by the signal processing into a map of the target field. Each buoy creates a local map of its own environment. Local maps from all the buoys are then combined to create a global map of the entire field of interest. This global map may then be used by tactical planners or an automated tactical planning system to determine areas of low concentration of mines, or areas in which to concentrate mine sweepers and other mine countermeasure assets.

2.2 Data Collection

After forming the concept described above, the Intelligent Sonobuoy group at Draper Laboratory designed and built a prototype buoy. Then, they conducted tests of the prototype during the summer and fall of 1994. The

purpose of the data collection effort was to create a data set to be used the evaluation of the Intelligent Sonobuoy sonar and signal processing systems. More specifically, the test was designed to achieve the following goals:

(1) Acquiring a library of geocoded multi-aspect angle sonar returns against mine-like and calibrated targets in a meaningful acoustic environment.

(2) Evaluating the Intelligent Sonobuoy sonar and signal processing systems' detection performance against these targets.

(3) Evaluating the Intelligent Sonobuoy system's local map generation algorithms for target registration over multi-aspect looks.

2.2.1 Sonobuoy Prototype

Only one prototype buoy was built, which therefore negates the possibility of testing multistatic operation. As this was a proof-of-concept vehicle, certain other modifications to the original system concept were also made. The basic subsystems for the sonobuoy remain intact, though. The sonobuoy was permanently fixed to a test barge to provide propulsion due to the lack of sufficient currents in the lake. The depth of the buoy was set at approximately 21 feet. The sonar receive array was surrounded by a hydrodynamic shroud to reduce water resistance. Most electronic equipment such as the power amplifier and data acquisition system were located above the surface on the barge. Additional test equipment and computers were also placed on the barge. Other changes more directly affected sonobuoy performance. The sonar receive array contained only 10 of the 16 elements necessary for a fully populated array. The active elements were located adjacent to one another to provide 13 of the desired 32 beams. As a result, the receive array constantly faced left. There was no float section for the buoy since the entire barge was used as a float. The GPS antennas were positioned on the top of the barge for optimal line of sight to the necessary satellites and the differential GPS ground station.

2.2.2 Mendum's Pond Test Site

The prototype sonobuoy was tested at the AUSI (Autonomous Undersea Systems Institute) field test support facilities at Mendum's Pond.

Mendum's Pond is a freshwater lake in southern New Hampshire, approximately 1.5 km long and 0.7 km wide. The water is highly stratified with sound speeds ranging from 1490 m/sec at the surface to 1436 m/sec at the bottom. Although the water is murky with visibility less than one meter at the bottom, there is very little vegetation. The target field extends over 180,000 square meters with an average depth of 45 ft. The bottom is typically mud sediment, with granite outcroppings. [6]

The test facility also contains a variety of sonar targets used in sonobuoy testing. Among these are three inert mine-like targets. The southeast target is inside a shipping frame and lies in 15 meters of water. The northwest target is located in 13 meters of water. Lastly, the southwest target is located in about 14 meters of water. [7] The approximate positions of these mine casings are known; however, the amount of silt covering the mines is unknown. In addition to these targets, two calibrated spheres, -11 dB and -20 dB, were tethered in the pond at approximately mid-water column.

Navigation at the test site was performed in several different ways. The primary method is the GPS system listed above. Located with the sonar array on the barge is the GPS receive antenna and differential receive antenna. In addition, a differential transmit station was located on the western shore of the pond at a site surveyed by AUSI. This station included a GPS receiver and antenna, an amplifier, and a differential transmit antenna. AUSI used a different system on the barge for navigation purposes and it was also used as a secondary navigation system for the sonobuoy. They adopted the Miniranger Falcon IV by Motorola as an RF navigation system which displays data in the Universal Transverse Mercator format. [7] Conversions were then made between the two types of data formats.

2.2.3 Sample Test Data

Members of the Intelligent Sonobuoy group, together with AUSI, tested the prototype buoy throughout the summer and fall of 1994. The test plan involved first performing a series of pings from a moored location in the center of the lake to determine the optimal set of waveform performance. A series of

5 different linear FM waveforms were chosen for active transmissions and were cycled repeatedly. These were 5 msec, 5000 Hz; 10 msec, 5000 Hz; 20 msec, 5000 Hz, 40 msec, 5000 Hz; and 40 msec, 7000 Hz. The group then cast the barge off from the mooring and drove it in a series of transit runs around the target field. The ping interval was set at approximately 6 seconds and an average of 900 pings were obtained for each run.

A sample of the beam-level receive data is shown in Figure 2-10. The blanking interval is clearly visible in this plot. The ping transmission in this figure lasted 20 msec and corresponds to approximately 30 meters. Thus no detections may be made within that first 30 meters. Every spike in the normalized signal energy above a certain threshold is declared a detection. The placement of the threshold must be low enough to allow detections of targets with a low target strength to pass, while at the same time it must be high enough to reduce the amount of background noise classified as detections. This tradeoff is made more apparent in Chapter 4.

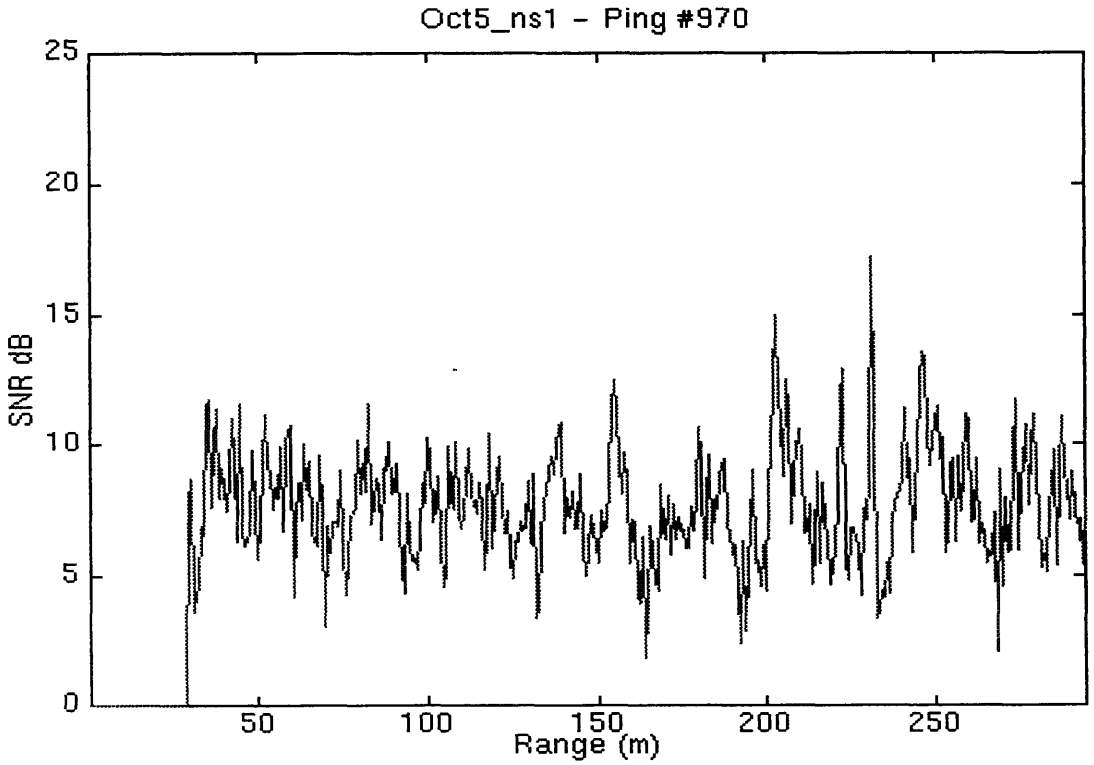

Figure 2-10 Normalized Signal Energy

Another method of displaying the detection data is shown in Figure 2-11. This plot, called a B-Scan, shows a waterfall type display of detections for a particular run. The B-Scan plots detections for a given ping as a function of range. The plot does not differentiate among beams or aspect angle, but merely plots the maximum value of normalized energy in each range bin for each ping. This format reveals the changes in detections from ping to ping.

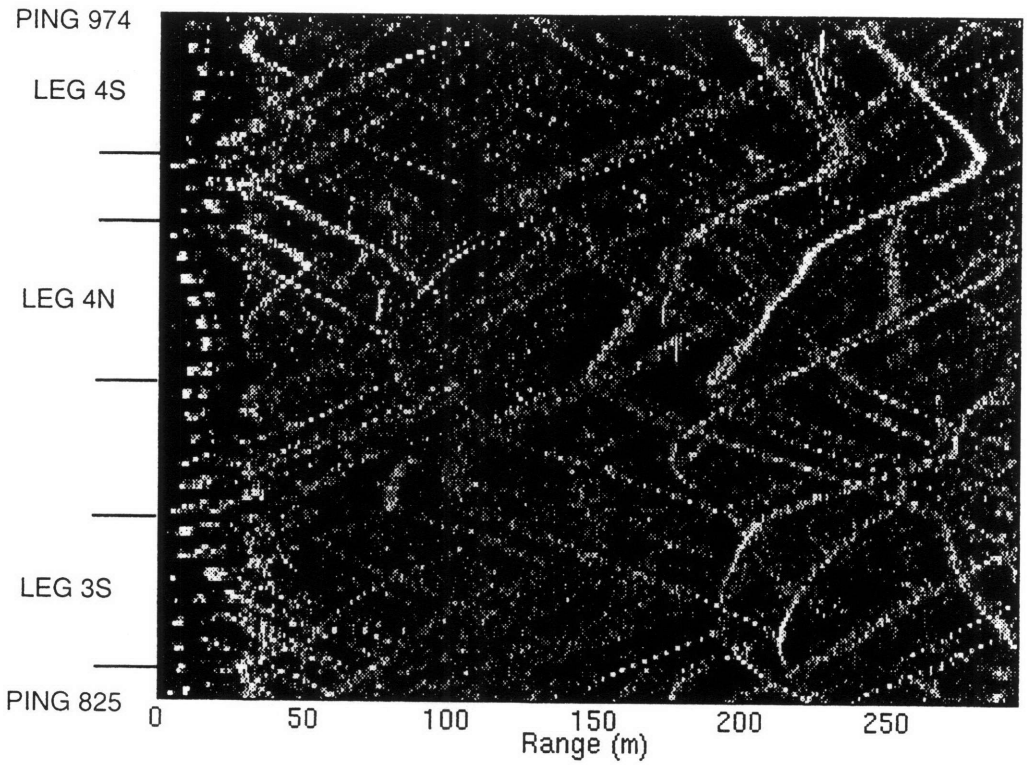

Figure 2-11 B-Scan Example for Pings 825-974, October 5, Transit NS1

The structure of the data in the B-Scan is easily explained though the geometry involved. If the sonobuoy proceeds in a straight line, the distance to the target defines a hyperbola. A simplified view of the B-Scan geometry is shown in Figure 2-12. This figure is a plot of ping number versus range to target over a 40 ping interval. The buoy is assumed to have a constant 100 meter cross-track offset and a constant vertical speed of 10 meters per ping.

In actual testing, the buoy did not move in a constant direction. This causes deviation from the exact hyperbola shape in the tracks plotted in Figure 2-11. The tracks are piecewise constant, though, and thus targets may

clearly be tracked from this data. Two items merit additional attention. First, the buoy's performance is evident from the strong detections still observed at ranges up to 300 meters. The high number of detections is also noteworthy. Each of the numerous serpentine tracks corresponds to a sonar target in the environment. This is clearly more than the expected number of known mine-like targets. The high number of clutter objects with significant target strength levels increases the difficulty of the localization and classification processes.

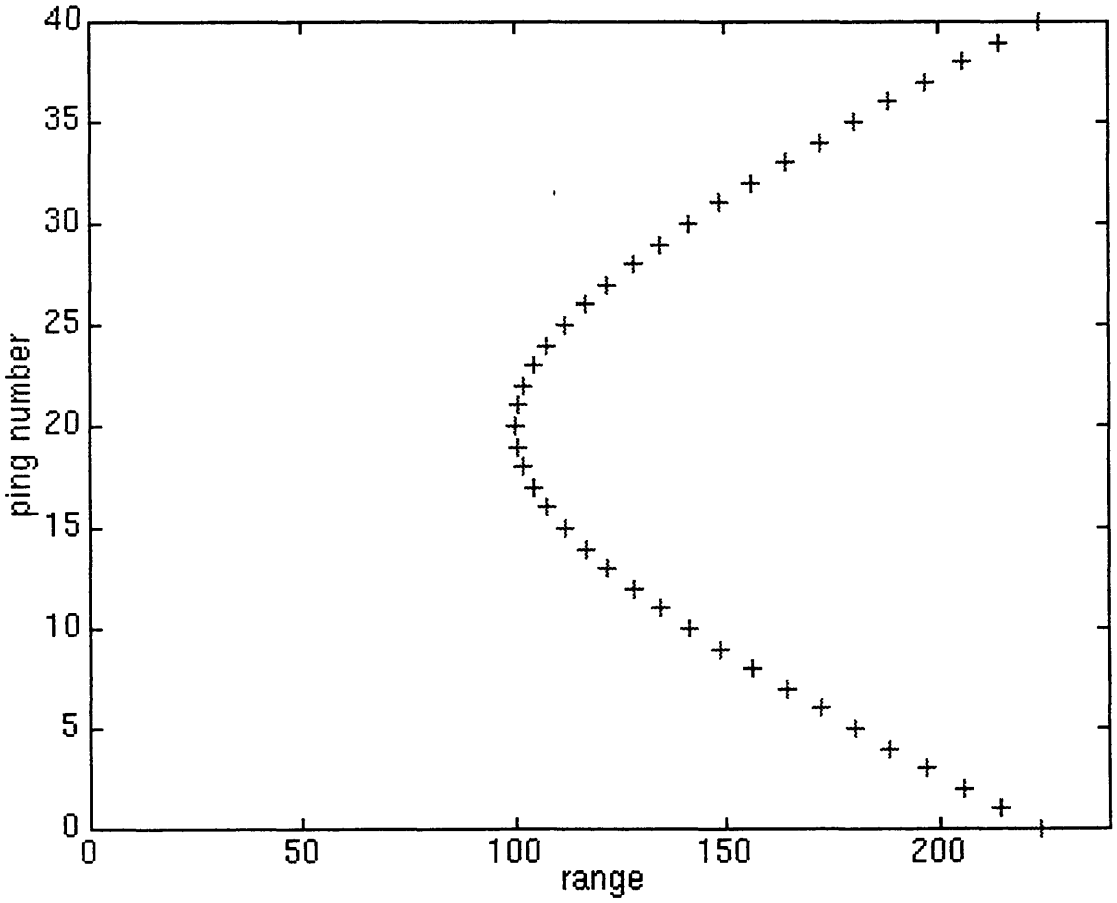

Figure 2-12 B-Scan Geometry

2.3 Error Characteristics

Various sources of error contribute to the final output. These errors must be accounted for when selecting an appropriate technique for map building. For this problem, the errors may be broken down into errors in the

sonar measurements and errors in the position of the buoy. The measurement error is further subdivided into errors in range and errors in azimuth. Additional error is caused by various noise sources. These sources of noise include background noise in the environment, the noise of the barge motor, self-noise created by the sonar array as it travels through the water, and electronic noise produced by the generator and other assorted electronic systems.

2.3.1 Range error

Several factors contribute to the range error of the sonobuoy. The range to target is determined by the time delay shown in the normalized energy display such as is shown in Figure 2-10. The resolution of the measurement depends largely on the bandwidth of the signal. The Intelligent Sonobuoy prototype used a center frequency of 8500 Hz. The sampling rate of our system was 27.4 KHz, with 16 bits per sample. Another source of error in the range estimate is caused by variations in the speed of sound. The speed of sound is assumed to be constant in this design, while this is not the case. The speed of sound depends on many parameters, including: depth, the season, geographic location, and time of day. [8] For this testing, all the parameters are relatively constant with the exception of depth. Several studies have been performed which show that the speed of sound in water depends almost entirely on three parameters: temperature, salinity and pressure. [8] Both the temperature and pressure of the water vary with its depth. The sound velocity profiles performed at Mendum's Pond record variations in the speed of sound from 1436 m/sec to 1490 m/sec. A more accurate determination of speed of sound was not necessary for this problem, because the inaccuracies associated with the position vastly outweigh the errors in the range estimate.

A common problem with sonar range estimates is caused by a phenomenon known as multipath. The echoes from a target arrive at a time equal to the speed of sound multiplied by the distance to the target and back. A problem arises because the sound may travel in more than one path. This problem, called multipath, is common in shallow water because the depth of

the water channel is small in relation to the horizontal range to target. [8] Multipath returns may echo off the surface or bottom of the water channel. These reflections appear after the primary detection and therefore act as detections at a greater range. A structure to the multipath detections should be evident in the B-Scan data. As the data in B-scan plot in Figure 2-11 suggests, multipath reflections did not appear to be too significant in these tests. A possible reason for this is that the multipaths were reduced by the horizontal beamwidths of the projector and receiver which eliminated those multipaths widely separated in angle.

A final source of error in the range estimate is caused by the geometry of the sonar return. The range estimate to target is assumed in this analysis to be the distance along the horizontal plane which contains the target. The actual distance along this plane will actually be somewhat less than the range estimate, depending on the height of the target in the water column and the range to the target. Figure 2-13 displays this scenario. The greatest error likely to be caused by this approximation would occur for a target on the bottom of the lake at a range equal to the minimum range allowable by the vertical beamwidth. This deviation at this point is a few meters, and is easily correctable.

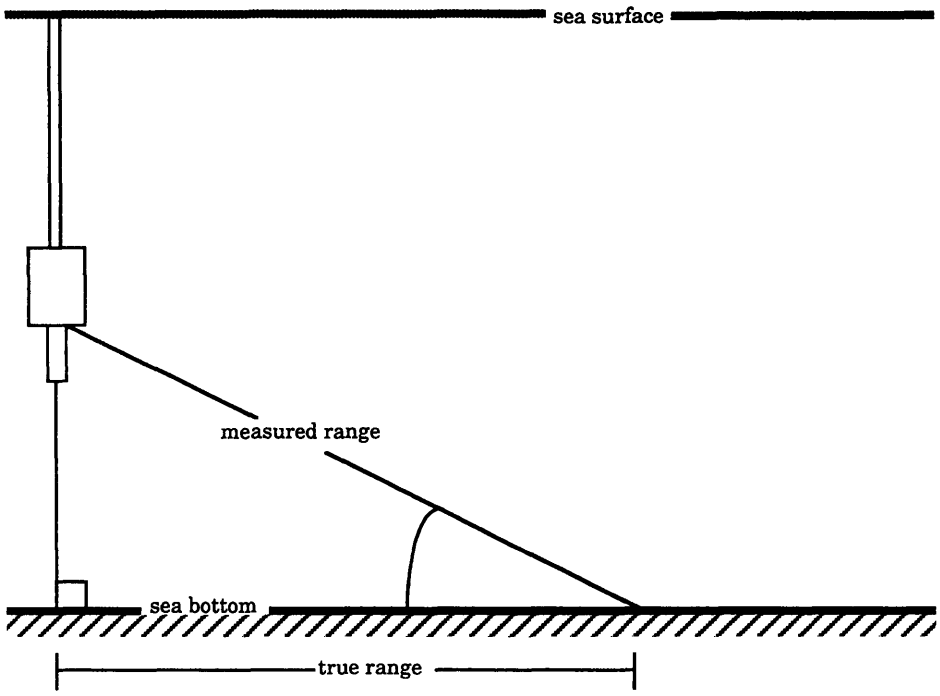

Figure 2-13 Range Approximation

2.3.2 Azimuth error

With the sonobuoy project, there are two primary sources of angle estimates. The first estimate is based solely on the beam which records the detection. As reported earlier, the beamwidth of each beam is 17 degrees and there is an 11.25 degree separation between centers. Thus a detection for a given beam may lie anywhere within an 17 degree sector with uniform probability. Compounding this problem is the fact that strong echoes show as detections on multiple beams. This increases the uncertainty of the angle estimate.

The monopulse estimate is an attempt to correct this problem. The monopulse estimate is an estimate of the exact angular position to target. This estimate is explained more in section 3-3. The variance of the monopulse estimate decreases with increasing SNR and is given by Equation 1. [9]

$$\text{var}\ \theta = \mathrm{K} * \left(\frac{\text{beamwidth}^2}{3} \right) * \left(\frac{1}{1+\text{snr}} \right) \tag{1}$$

K is a factor depending on the specifics of the noise.

2.3.3 Position error

The position error refers to errors in the buoy position as it is pinging. An accurate estimate of the buoy position is fundamental to creating an accurate map. Obviously the range and bearing to a target are meaningless if the starting point is unknown.

The position data for Intelligent Sonobuoy system is based on the Global Positioning System (GPS). A conventional CA code receiver was located on the barge along with the differential receive antenna. A duplicate GPS receiver was placed at a surveyed location on the shore with the differential transmission antenna. Differential corrections sent out by this antenna correct for deviations caused by propagation through the atmosphere and errors intentionally injected at the source. When working correctly, this system should provide a variance of position on the order of less than a meter. [10] The geometry of the lake created problems which caused actual performance to deteriorate from that ideal. GPS satellites generally track in a position south of our test area. The GPS system requires line of sight for transmission. Therefore, for best operation, the GPS antenna needs to have an unobstructed view toward the south. Unfortunately this was not possible in the test range at Mendum's Pond. Improvements made in site selection increased the reliability of the data, but some serious glitches remained. These discontinuities in the position data occur whenever the GPS receiver switches satellite constellations. Four GPS satellite are used to create a fix, but if one of those satellites is out of view, it is replaced by a different satellite. When the new constellation of satellites is used to determine the position, a jump occurs

in the differentially corrected position data. Gradually the satellites in the new constellation track back to the proper course, but this may take 10-15 seconds, or several pings. When the previously obstructed satellite reappears, the receiver switches back to the original constellation and another discontinuity occurs.

An even greater problem occurs if multiple satellites are obstructed from view. This was not a problem on the barge since the center of the lake provided open access to the sky in all directions. The shore station was located in a fixed location along the edge of the lake and its view was partially obstructed by nearby trees. On several occasions, the number of satellites acquired by the GPS receiver at the shore location dropped below four and a position fix was not made. When this happened, the GPS system located on the barge could no longer take advantage of the differential corrections, so the standard deviation of the position measurement increased to over 30 meters.

A plot of the first 200 pings of the October 5th North-South run appears in Figure 2-14. Here the discontinuities in position are clearly observed. The first major break at 2150 east, 1760 north shows an example of the type of error which occurs during a change of satellites. At first there is a large jump, and then the position slowly tracks onto the proper location.

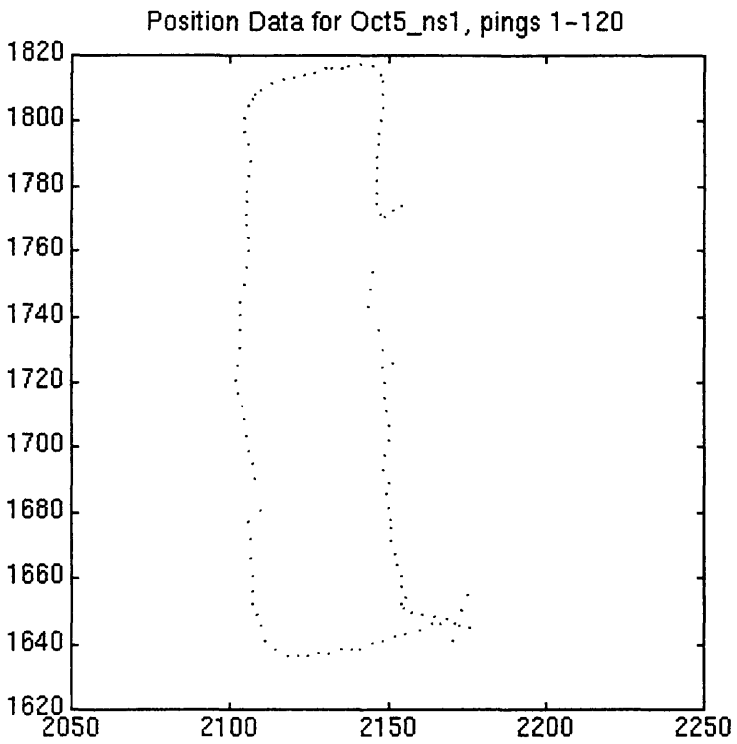

Figure 2-14 Buoy Position during pings 1-120 of Oct. 5, NS1

Creating maps obviously requires first filtering or smoothing this navigational data to remove the known discontinuities. A filtering program designed for this purpose removes those discrepancies and replaces them with appropriate values. First the instantaneous velocity for each position is calculated. The position data from the buoy is converted from latitude and longitude to UTM coordinates. Then the instantaneous velocity for each point is determined by comparing its position to the previous position. A plot of the instantaneous velocity for the first 400 data points appears in Figure 2-15. Here the jumps in position data are clearly observed. These points are located by comparing the instantaneous velocity to a threshold. There are both high and low values for the threshold and these values are determined by the known barge dynamics. Data points were observed at approximately one second intervals and the inertia of the barge does not allow drastic changes in that amount of time. The points outside the acceptable range are then rejected and replaced by more appropriate values. More specifically, each rejected point is replaced by a new value which is equal to the mean of the points surrounding it.

A split-windowed mean of the instantaneous velocity is used so that nearby data points do not influence the mean. A plot of the new, smoothed velocity vector also appears in Figure 2-15. The spikes in the data are clearly removed.

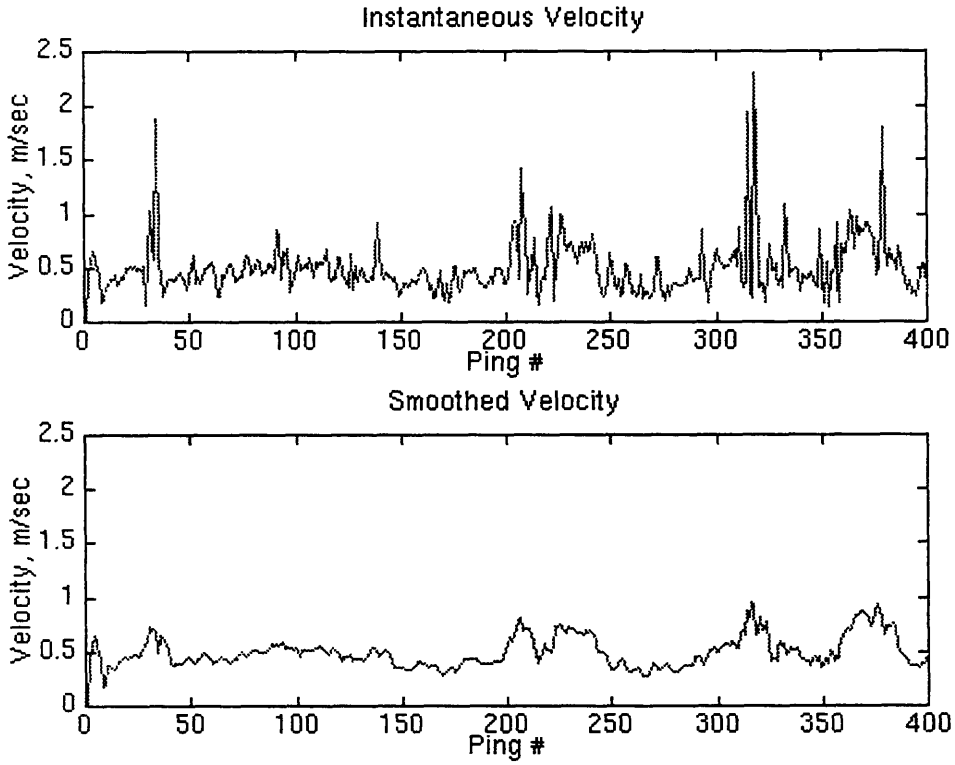

Figure 2-15 Instantaneous Velocity, Original and Filtered Version

The final step is to calculate a new set of positions for the rejected points. This is accomplished using the smoothed velocity combined with the compass heading data. The revised position data can be seen in Figure 2-16. The discrete jumps in position data have now been successfully removed, while the finer-scale changes in position have been retained. These characteristics in position data are important for the integration of data between pings.

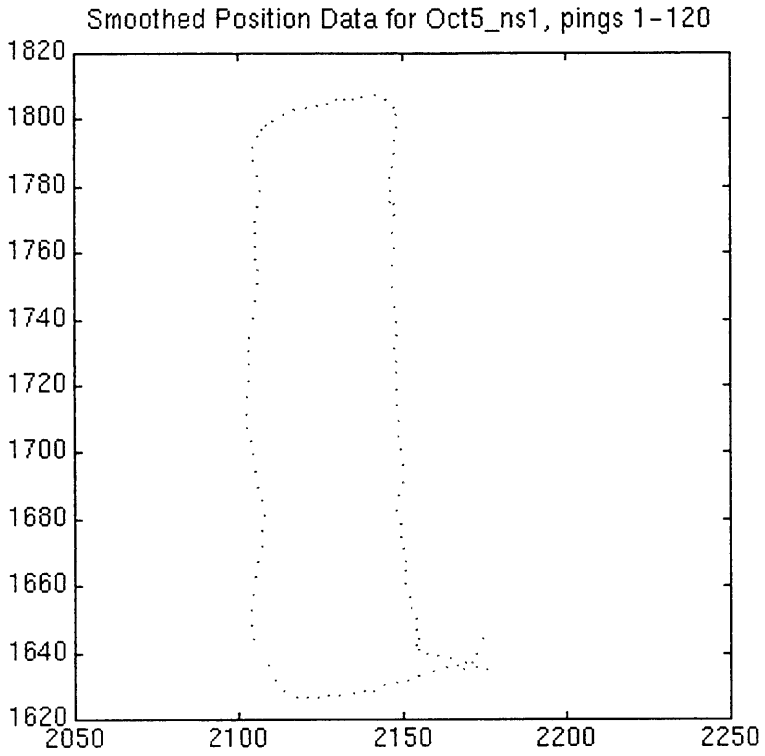

Figure 2-16 Position Data after Filtering

3. Data Fusion / Map Building Algorithms

The previous chapters have introduced the basic problem which needs to be solved. This problem is to detect and localize mines and mine-like objects in the sonar environment. In particular, the analysis will focus on data obtained during testing at Mendum's Pond in 1994. The sonar measurements of the target field are characterized by rather accurate information concerning the range, but relatively little information regarding the azimuth of the detection. The sonar platform at each ping may be modeled as a separate sensor both temporally and spatially separated from the others. The problem then becomes one of combining data from these different sensors into a composite map. Techniques for combining the information from several sensors are a concern of multisensor data fusion. [11]

Multisensor data fusion is often very useful when data is noisy. Frequently, many signals and sensors working together produce superior results when compared to a single sensor. A study by Willet, et. al. showed that the gains from a fused system are minimal is a statistically well-behaved environment, but can be quite substantial in noisier environments. [12] Overlap in area coverage can also improve detection performance. The redundant information contained in the overlap helps to reduce ambiguity in a noisy environment. [13] Also, spatially separated sensors reduce the probability that a target is blocked from view.

In an effort to encourage the use of data fusion in target discrimination and tracking, the Assistant Secretary of Defense for C^3I (Command, Control, Communications, and Intelligence) set up a panel to codify data fusion terminology. The definition formulated from that panel has since evolved into the following:

> *A multilevel, multifaceted process dealing with the automatic detection, association, correlation, estimation, and combination of data and information from single and multiple sources.* [14]

There are four levels in a classic data fusion hierarchy. The goal of Level 1 fusion is to achieve a refined position and identity estimate by combining individual sensor position and identity estimates. Therefore, Level 1 processing is all that is necessary to detect and localize mines in this problem. In Level 1 processing, sensor outputs must be combined to produce the desired target discrimination and position estimate. Different fusion algorithms may be used for each of these tasks and they may have separate architectures as well. A diagram listing Level 1 processing algorithms is shown in Figure 3-1.

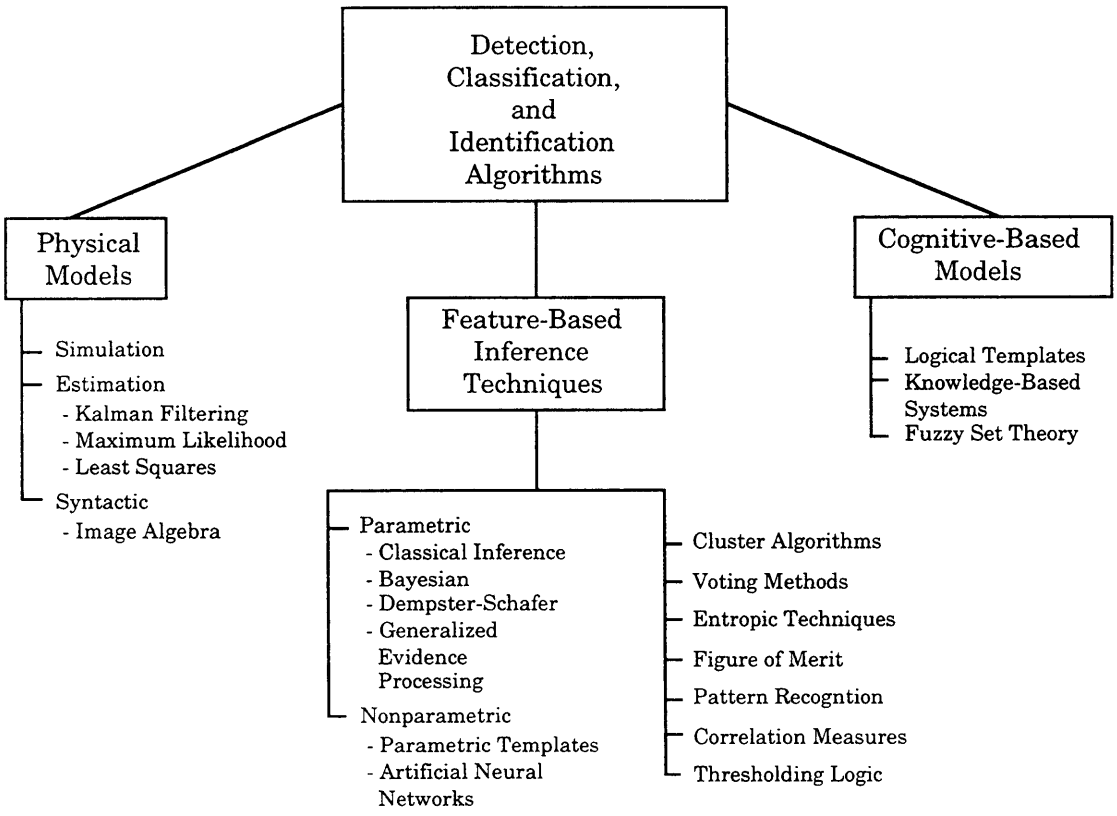

Figure 3-1 Taxonomy of Level 1 Algorithms

The types of algorithms available for a given problem depends highly on certain parameters in the problem, such as the type of data and any a priori information about that data. Physical models involve using features which are easily measurable and recognizable, such as the radar cross section as a function of aspect angle. These methods involve comparing the measurements to predicted values suggested by the model. Feature-based inference

techniques accomplish classification by transforming information into knowledge of its identity. Feature-based classification methods may be further subdivided into parametric, nonparametric, and other methods. Lastly, cognitive-based models attempt to model human thought patterns.

In addition to choosing an appropriate fusion algorithm, a system designer must also select a proper data fusion architecture. The data fusion architecture is composed of the individual processing components and their interconnections. The design of this architecture again depends on the problem and the types of data being combined.

There are three main types of data fusion architectures: sensor-level fusion, also referred to as postindividual sensor processing fusion and autonomous fusion; central-level fusion, also referred to as preindividual sensor processing fusion and centralized fusion; and hybrid fusion, which is a combination of the previous two architectures. [14]

The architecture for sensor level fusion is shown in Figure 3-2. In this architecture, decisions regarding target classification and identification are made at a low level, before combining with other sensors for target tracking and association purposes. This architecture is optimal when the sensors use different physical phenomena to make detections. As a result, the sensors are less likely to arrive at false alarms caused by the same types of clutter or noise. Further advantages of sensor-level architectures include a reduced workload on the central processor, flexibility in the structure and number of sensors, and ease of transition for adding data fusion to an existing multisensor architecture.

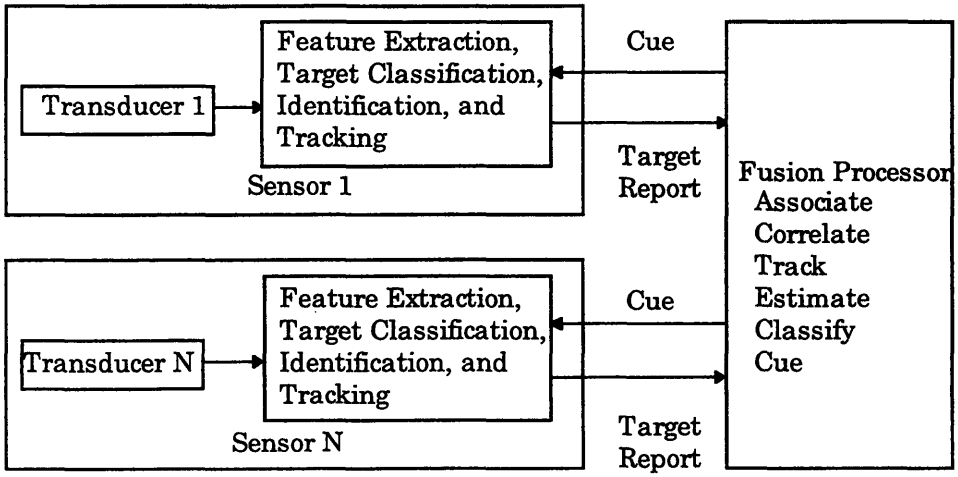

Figure 3-2 Sensor-Level Fusion Architecture

For central-level fusion, each sensor transmits minimally processed data to the central processor. A diagram showing this architecture is shown in Figure 3-3. Central-level fusion is optimal for target tracking purposes. One reason for this is that all the data is combined before making decisions, so multiple hypothesis tracking is more readily performed. Other advantages of central-level fusion include more effective object discrimination if the sensors use the same physical phenomena, increased reliability of signal processing hardware, and the possibility of reduced cost and power consumption since fewer processors should be needed.

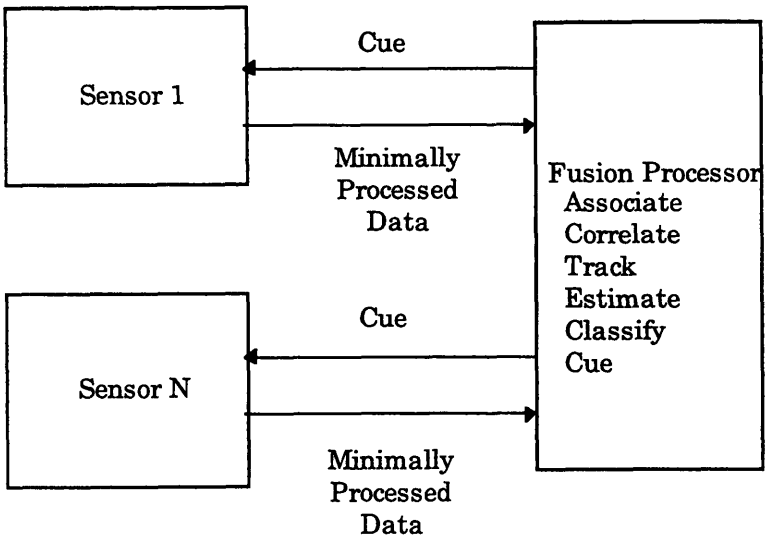

Figure 3-3 Central-Level Fusion Architecture

Hybrid fusion architectures can combine the advantages of both sensor-level and central-level architectures. The main drawbacks of this architecture are increased complexity and increased data transmission requirements.

3.1 Model of problem

The map building subroutines must localize and map target locations from the array of detection data. This array includes the ping number, beam number, range to detection, monopulse angle estimate, signal to noise ratio (SNR) of detection, and absolute energy level. This data is assumed to contain a majority of relevant information from the sonar return, but some information has been lost in this data reduction. This loss is assumed to be low and greatly outweighed by the increased computational benefits. In creating the detection lists, a degree of sensor-level fusion has already been performed.

A sample of the data available for processing appears in Table 1. The number of detections per ping is determined by the threshold used for the signal to noise ratio, as well as by the sonar parameters and the geometry of the underwater environment. This table reflects a simulation in which the target field consisted of one cylinder.

Ping #	Beam #	Range (m)	Bearing (degrees)	SNR (dB)	Echo Level (dB)
1	1	131.02	216.33	32.85	54.21
1	6	96.62	253.76	10.86	53.83
1	6	110.26	250.88	10.55	53.81
1	13	158.12	340.40	45.56	67.47
2	1	126.26	216.03	37.55	54.21
2	6	105.51	249.94	8.12	53.48
2	13	153.40	339.93	45.54	67.77
3	1	114.81	209.64	17.59	54.13
3	13	98.68	339.39	15.11	54.07
3	13	148.67	339.42	45.56	67.90

Table 1 Example of Detection Array

In addition to the detection array, a list of sensor position data is also provided. This array includes time, latitude, longitude, and heading for each ping number.

The lack of a sufficiently precise estimate of angle creates an added problem which must be dealt with. As stated previously, the range estimate is relatively precise, while the azimuth estimate is not. This lack of angle accuracy hampers attempts at data association and clustering of multiple measurements. Since the accuracy of the angle estimate is known only by the beam in which the detection occurred, the region of uncertainty for the measurement is an arc, such as is shown in Figure 3-4. The buoy location and angular position, the range to detection and beam in which the detection occurred all combine to determine the arc location and orientation. The width of the arc is equivalent to the beamwidth, which in this case is 17 degrees. The width of the arc in meters is directly proportional to the range estimate of the detection.

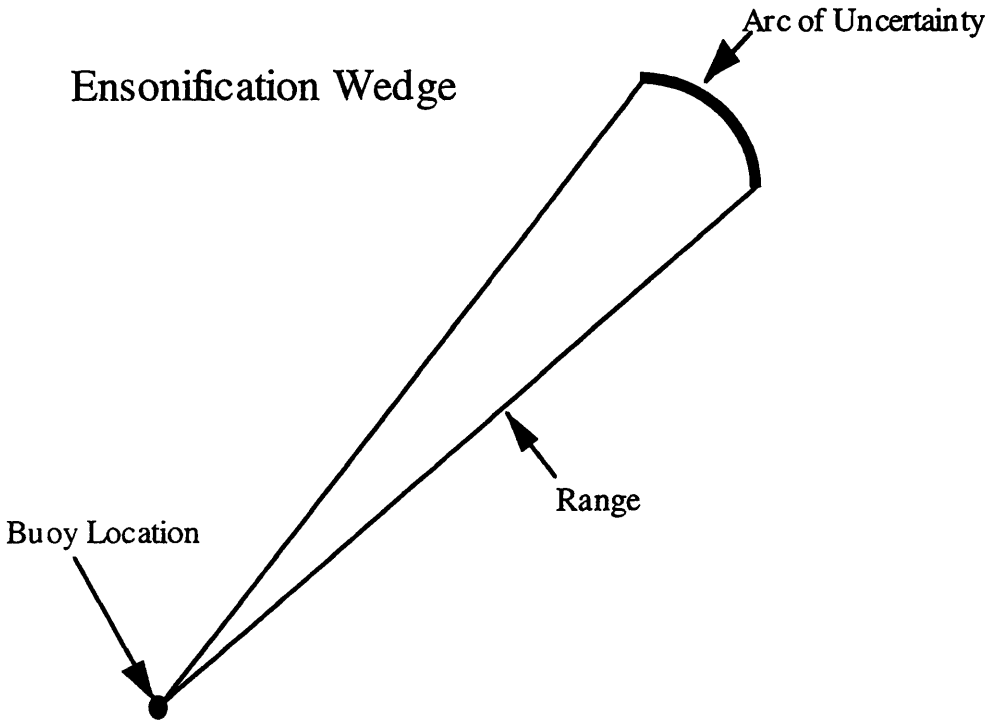

Figure 3-4 Region of Azimuthal Uncertainty

The uncertainties in range and azimuth result in a rather imprecise knowledge of target localization from just one detection. Furthermore, separate detections of the same object will be obtained on separate pings and thus separate buoy positions, so an accurate estimate of the target location cannot be determined from only one ping. Since each buoy position is defined as a sensor, the remaining processing must be done at the central-level. Thus, central-level data fusion algorithms must be developed to localize the sonar targets.

The type of algorithm depends on the data available. Many different algorithms would suit this purpose. Due to the amount of uncertainty in a single detection, an algorithm must be able to combine multiple detections into a single target localization. Noisy and incomplete data hampers attempts at physical modeling. Also, the lack of a priori information regarding the target environment, especially concerning the number of targets, reduces the ability to estimate the sonar returns. For these reasons, feature-based methods are more likely to be appropriate for this problem. Again, the lack of information

regarding the a priori probabilities controls the selection of an appropriate algorithm. In addition to the lack of a priori probabilities, a measure of the uncertainties regarding individual detections is difficult to quantize. These problems hinder attempts at parametric methods. Other feature-based methods which can work under such situations include nonparametric methods, clustering algorithms, figures of merit, pattern recognition, correlation measures, and thresholding logic.

3.2 Maximum-Likelihood Energy Integration

One method to determine an estimate of the target locations has been developed based on principles of hypothesis testing and maximum likelihood estimation. The background for this method starts as a physical model of the sonar environment; however, the composition of the data and uncertainties regarding target numbers and position result in more of a feature-based algorithm.

3.2.1 Derivation of Algorithm

As mentioned above, the derivation of this algorithm results from principles of hypothesis testing. The questions we are trying to answer is whether or not a target is present and where that target is. First it is necessary to form the hypotheses. Hypothesis H_0 is known as the null hypothesis and corresponds to no target present. Hypothesis H_1 states that a target is present. A decision rule must now be established to determine between these two hypotheses.

There are four possible outcomes every time a decision is made. These are:

1. H_0 true, choose H_0.	"Correct Non-detection"
2. H_0 true, choose H_1.	"False Alarm"
3. H_1 true, choose H_1.	"Correct Detection"
4. H_1 true, choose H_0.	"Miss"

Of these four possibilities, outcomes 1 and 3 correspond to correct choices while outcomes 2 and 4 correspond to incorrect choices. Actually, in probability terms, outcome 2 is known as a false alarm, outcome 3 is known as a detection, and outcome 4 is known as a miss. A decision criterion must now be established to attach a relative importance to each possible outcome. For example, in cancer testing, the most important outcome would be to minimize the probability of a miss. The other error, that of a false alarm, is less important, since additional tests may be performed to confirm the presence or absence of the disease.

One such criterion is called Bayes' risk. In this method, a cost is placed on each possible outcome. The cost of making an error is assumed to be greater than the cost of making a correct decision. The object is then to minimize the expected value of the cost. The expected value of the cost is called the risk and is equal to the sum of the probability of each outcome. The outcomes are also weighted by the appropriate cost and the a priori probabilities. In mathematical terms:

$$\begin{aligned} \text{Risk} = {} & C_{00}P_0 \Pr(\text{say } H_0 \mid H_0 \text{ is true}) \\ & + C_{10}P_0 \Pr(\text{say } H_1 \mid H_0 \text{ is true}) \\ & + C_{11}P_1 \Pr(\text{say } H_1 \mid H_1 \text{ is true}) \\ & + C_{01}P_1 \Pr(\text{say } H_0 \mid H_1 \text{ is true}) \end{aligned} \tag{2}$$

This criterion may now be used as a rule to divide the observation space into the two parts. A resulting decision rule between the two regions appears below.

If

$$P_1(C_{01} - C_{11})p_{r|H_1}(R \mid H_1) \geq P_0(C_{10} - C_{00})p_{r|H_0}(R \mid H_0), \tag{3}$$

Then conclude H_1 is true, otherwise conclude H_0 is true.

Another way to express this statement is:

$$\frac{p_{r|H_1}(R \mid H_1)}{p_{r|H_0}(R \mid H_0)} \begin{array}{c} \text{Choose } H_1 \\ > \\ < \\ \text{Choose } H_0 \end{array} \frac{P_0(C_{10} - C_{00})}{P_1(C_{01} - C_{11})} \tag{4}$$

The quantity on the left is known as the likelihood ratio and is given by:

$$\Lambda(R) = \frac{p_{r|H1}(R \mid H_1)}{p_{r|H0}(R \mid H_0)} \tag{5}$$

This number is a ratio of two functions of a random variable, and thus is a random variable itself. It is also one dimensional, regardless of the dimensionality of the observation, R.

The quantity on the right is the threshold of the test and is given by:

$$\eta = \frac{P_0(C_{10} - C_{11})}{P_1(C_{01} - C_{00})} \tag{6}$$

Since the natural logarithm is a monatonic function and both sides of are positive, an equivalent test is:

$$\ln \Lambda(R) \begin{array}{c} H_1 \\ > \\ < \\ H_0 \end{array} \ln \eta \tag{7}$$

In this problem, the prior probabilities, P_0 and P_1, are unknown and assumed to be equal. Also, the cost function has been simplified as follows: $C_{10} = C_{01} = 1$, $C_{01} = C_{00} = 0$. These assumptions comprise what is known as maximum likelihood criteria.

In the basic sonar problem, the decision to be made is whether or not a mine is present. Therefore, it is a binary hypothesis testing problem, where

hypothesis H_1 is that a mine is present and hypothesis H_0 is that no mine is present. Maximum likelihood criteria is assumed as shown above. The only unknowns remaining are the probability density functions under the two hypotheses. A simpler example will first be presented, followed by extensions which correspond more directly to the problem defined in section 3.1.

Example 1:

Assume that there is only one measurement and the target position is known. For this problem, the hypothesis test is used to determine whether or not a target is present at a given range.

The probability density functions under both signals are defined by the envelope of the complex Gaussian signal. The density functions both have zero mean and different variances.

Hypotheses:

H_1: $Z = S + V$

H_0: $Z = V$

Assumptions:

S, V complex Gaussian signals

$E(SV) = 0$

$E(S) = E(V) = 0$

$\mathrm{Var}(Z \mid H_1) = \sigma_s^2 + \sigma_v^2$

$\mathrm{Var}(Z \mid H_0) = \sigma_v^2$

The probability density function for z given H_1 is:

$$p_{z|H_1}(Z \mid H_1) = \frac{1}{2\pi(\sigma_s^2 + \sigma_v^2)^{1/2}} \exp\left(-\frac{1}{2(\sigma_s^2 + \sigma_v^2)} (|Z|^2) \right) \qquad (8)$$

The probability density function for z given H_0 is:

$$p_{z|H_0}(Z \mid H_0) = \frac{1}{2\pi\sigma_v} \exp\left(-\frac{1}{2\sigma_v^2}\left(|Z|^2\right)\right) \tag{9}$$

Thus the likelihood ratio function for this example may be expressed as:

$$\Lambda(Z) = \frac{\frac{1}{2\pi\left(\sigma_s^2+\sigma_v^2\right)^{1/2}} \exp\left(-\frac{1}{2\left(\sigma_s^2+\sigma_v^2\right)}\left(|Z|^2\right)\right)}{\frac{1}{2\pi\sigma_v} \exp\left(-\frac{1}{2\sigma_v^2}\left(|Z|^2\right)\right)} \begin{matrix} H_1 \\ > \\ < \\ H_0 \end{matrix} 1 \tag{10}$$

Now, taking applying the natural logarithm to both sides yields:

$$\ln \Lambda(Z) = \left[\ln \frac{1}{2\pi\left(\sigma_s^2+\sigma_v^2\right)^{1/2}} + \left(-\frac{1}{2\left(\sigma_s^2+\sigma_v^2\right)}\left(|Z|^2\right)\right)\right] - \left[\ln \frac{1}{2\pi\sigma_v} + \left(-\frac{1}{2\sigma_v^2}\left(|Z|^2\right)\right)\right] \begin{matrix} H_1 \\ > \\ < \\ H_0 \end{matrix} 0 \tag{11}$$

Combining like terms:

$$-\frac{1}{2}\left(|Z|^2\left(\frac{1}{\sigma_s^2+\sigma_v^2} - \frac{1}{\sigma_v^2}\right)\right) \begin{matrix} H_1 \\ > \\ < \\ H_0 \end{matrix} -\ln\left(\frac{\sigma_v}{\left(\sigma_s^2+\sigma_v^2\right)^{1/2}}\right) \tag{12}$$

Finally:

$$\frac{|Z|^2}{\sigma_v^2} \begin{matrix} H_1 \\ > \\ < \\ H_0 \end{matrix} -2\left(\frac{\sigma_s^2+\sigma_v^2}{\sigma_s^2}\right)\ln\left(\frac{\sigma_v}{\left(\sigma_s^2+\sigma_v^2\right)^{1/2}}\right) = \gamma_1 \tag{13}$$

Therefore, the signal energy is normalized by the background noise variance and compared to a threshold. If the signal energy exceeds the threshold, then a detection is declared. In practice, the threshold is adjustable to achieve a desired probability of detection and probability of false alarm. This procedure for setting the threshold represents what is known as Neyman-Pearson criteria.

Example 2:

Assume that only a single measurement is made, but the target position is unknown. The position of the target then becomes an unknown, non-random variable. In example 3 we will determine the target location through maximum likelihood estimation techniques.

The error in range is now considered. This error consists of both the range measurement error and the navigational error of the buoy. The range error may be modeled as a Gaussian function and simply adds a term to the target present hypothesis.

The probability density function for z given H_1 is:

$$p_{z|H_1,\sigma_r}(Z \mid H_1) = \frac{1}{2\pi\left(\sigma_s^2+\sigma_v^2\right)^{1/2}}\frac{1}{\sqrt{2\pi}\sigma_r}\exp\left(-\frac{1}{2\left(\sigma_s^2+\sigma_v^2\right)}\left(|Z|^2\right)\right)\exp\left(-\frac{1}{2\sigma_r^2}\left(r_0-r(x,y)\right)^2\right) \tag{14}$$

In this formula, r_0 is the measured range to the target, r(x,y) is the range from the buoy to a pixel (x,y) in the plane, and σ_r is the RMS sum of the sonar range resolution and positional accuracy.

The probability density function for z given H_0 is:

$$p_{z|H_0}(Z \mid H_0) = \frac{1}{2\pi\sigma_v}\exp\left(-\frac{1}{2\sigma_v^2}\left(|Z|^2\right)\right) \tag{15}$$

Thus the likelihood ratio function for this example may be expressed as:

$$\Lambda(Z) = \frac{\frac{1}{2\pi\left(\sigma_s^2+\sigma_v^2\right)^{1/2}}\frac{1}{\sqrt{2\pi}\sigma_r}\exp\left(-\frac{1}{2\left(\sigma_s^2+\sigma_v^2\right)}\left(|Z|^2\right)\right)\exp\left(-\frac{1}{2\sigma_r^2}\left(r_0-r(x,y)\right)^2\right)}{\frac{1}{2\pi\sigma_v}\exp\left(-\frac{1}{2\sigma_v^2}\left(|Z|^2\right)\right)} \begin{matrix} H_1 \\ > \\ < \\ H_0 \end{matrix} 1 \tag{16}$$

Applying the natural logarithm to both sides and combining like terms:

$$-\frac{1}{2}\left(|Z|^2\left(\frac{1}{\sigma_s^2+\sigma_v^2}-\frac{1}{\sigma_v^2}\right)\right)-\frac{1}{2}\left(\frac{r_0-r(x,y)^2}{\sigma_r^2}\right) \begin{matrix} H_1 \\ > \\ < \\ H_0 \end{matrix} -\ln\left(\frac{\sigma_v}{\sqrt{2\pi}\sigma_r\left(\sigma_s^2+\sigma_v^2\right)^{1/2}}\right)=\gamma_2 \tag{17}$$

Finally:

$$\frac{|Z|^2}{\sigma_v^2}-\frac{\left(r_0-r(x,y)\right)^2}{\sigma_r^2} \begin{matrix} H_1 \\ > \\ < \\ H_0 \end{matrix} -2\left(\frac{\sigma_s^2+\sigma_v^2}{\sigma_s^2}\right)\ln\left(\frac{\sigma_v}{\sqrt{2\pi}\sigma_r\left(\sigma_s^2+\sigma_v^2\right)^{1/2}}\right)=\gamma_2 \tag{18}$$

This equation describes the likelihood function for each point in the target range. In essence, the error in the position estimate has created an additional term on the left hand side of the equation which causes the likelihood of a target to decrease as the range to the point (x, y) deviates from the measured range, r_0.

Example 3:

Assume that there are multiple detections and the target position is unknown.

This final case examines the remaining extension to the problem at hand, which is to fuse multiple measurements together under the constraints

of navigational uncertainty. The target position will be estimated by maximizing the energy over the entire plane.

Hypotheses:

H_1: $Z_n = S_n + V_n$
H_0: $Z_n = V_n$

Assumptions:

S_n, V_n complex Gaussian signals
$E(S_n V_n) = 0$
$E(S_n) = E(V_n) = 0$
$Var(Z_n \mid H_1) = \sigma_s^2 + \sigma_v^2$
$Var(Z_n \mid H_0) = \sigma_v^2$
$Var(Range) = \sigma_r^2$
Detections are independent

Since the detections are assumed to be independent of one another, the resulting joint probability density function is equal to the product of the individual probability densities.

$$p_{z_1,z_2,\ldots,z_N}(Z_1,Z_2,\ldots,Z_N) = p_{z_1}(Z_1)p_{z_2}(Z_2)\ldots p_{z_N}(Z_N) \tag{19}$$

This problem is simplified even further since all the individual probability density functions are identical and Gaussian.

The probability density function for z given H_1 is:

$$p_{z|H_1,\sigma_r}(Z \mid H_1) = \prod_{i=1}^{N} \left\{ \frac{1}{2\pi(\sigma_s^2+\sigma_v^2)^{1/2}} \frac{1}{\sqrt{2\pi}\sigma_r} \exp\left(-\frac{1}{2(\sigma_s^2+\sigma_v^2)}\left(|Z_i|^2\right)\right) \exp\left(-\frac{1}{2\sigma_r^2}\left(r_i - r(x,y)\right)^2\right)\right\} \tag{20}$$

The probability density function for z given H_0 is:

$$p_{z|H_0}(Z \mid H_0) = \prod_{i=1}^{N} \left\{ \frac{1}{2\pi\sigma_v} \exp\left(-\frac{1}{2\sigma_v^2} \left(|Z_i|^2 \right) \right) \right\} \tag{21}$$

Thus the likelihood ratio function for this example may be expressed as:

$$\Lambda(Z) = \frac{\prod_{i=1}^{N} \left\{ \frac{1}{2\pi\left(\sigma_s^2 + \sigma_v^2\right)^{1/2}} \frac{1}{\sqrt{2\pi}\sigma_r} \exp\left(-\frac{1}{2\left(\sigma_s^2 + \sigma_v^2\right)} \left(|Z_i|^2 \right) - \frac{1}{2\sigma_r^2} \left(r_i - r(x,y) \right)^2 \right) \right\}}{\prod_{i=1}^{N} \left\{ \frac{1}{2\pi\sigma_v} \exp\left(-\frac{1}{2\sigma_v^2} \left(|Z_i|^2 \right) \right) \right\}} \begin{matrix} H_1 \\ > \\ < \\ H_0 \end{matrix} 1 \tag{22}$$

Applying the natural logarithm to both sides yields:

$$\ln \Lambda(Z) = N \ln \frac{1}{2\pi\left(\sigma_s^2 + \sigma_v^2\right)^{1/2}} + N \ln \frac{1}{\sqrt{2\pi}\sigma_r} - N \ln \frac{1}{2\pi\sigma_v} - \frac{1}{2\left(\sigma_s^2 + \sigma_v^2\right)} \sum_{i=1}^{N} |Z_i|^2 + \\ - \frac{1}{2\sigma_r^2} \sum_{i=1}^{N} \left(r_i - r(x,y)^2 \right) + \frac{1}{2\sigma_v^2} \sum_{i=1}^{N} |Z_i|^2 \begin{matrix} H_1 \\ > \\ < \\ H_0 \end{matrix} 0 \tag{23}$$

Combining like terms:

$$-\frac{1}{2}\left(\frac{1}{\sigma_s^2 + \sigma_v^2} - \frac{1}{\sigma_v^2} \right) \sum_{i=1}^{N} |Z_i|^2 - \frac{1}{2} \sum_{i=1}^{N} \frac{\left(r_i - r(x,y) \right)^2}{\sigma_r^2} \begin{matrix} H_1 \\ > \\ < \\ H_0 \end{matrix} - N \ln \left(\frac{\sigma_v}{\sqrt{2\pi}\sigma_r \left(\sigma_s^2 + \sigma_v^2\right)^{1/2}} \right) \tag{24}$$

Rewriting equation [24]:

$$\sum_{i=1}^{N}\left[\frac{|Z_i|^2}{\sigma_v^2}-\frac{(r_i-r(x,y))^2}{\sigma_r^2}\right]\underset{H_0}{\overset{H_1}{\gtrless}}-2N\left(\frac{\sigma_s^2+\sigma_v^2}{\sigma_s^2}\right)\ln\left(\frac{\sigma_v}{\sqrt{2\pi}\sigma_r(\sigma_s^2+\sigma_v^2)^{1/2}}\right)=\gamma_3 \quad (25)$$

The estimate of the target location is determined by first performing this hypothesis test for every point (x,y) in the map plane and then finding the point which has the maximum value of energy in the plane. This point is then compared to the detection threshold to determine whether a target is present. Thus, an approximately similar expression for determining the existence and location of a target is the following:

$$\left[\max_{x,y} E(x,y)\right]\underset{H0}{\overset{H1}{\gtrless}}\gamma_{map} \quad (26)$$

where E(x,y) is the following energy summation:

$$E(x,y)=\sum_{i=1}^{N_{det}}\left[\frac{|z(n_i,b_i,r_i)|^2-\sigma_v^2}{\sigma_v^2}-\frac{(r_i-r(x,y))^2}{\sigma_r^2}\right]=\sum_{i=1}^{N_{det}}\left[SNR_i-\frac{(r_i-r(x,y))^2}{\sigma_r^2}\right] \quad (27)$$

and

N_{det} = number of detections passing screening threshold

n_i = ping number at which detection i occurred

b_i = beam in which detection i occured

r_i = observed range at detection i

$z(n_i, b_i, r_i)$ = measured signal at point of detection i

$\frac{|z(n_i, b_i, r_i)|^2 - \sigma_v^2}{\sigma_v^2}$ = SNR_i = estimated signal to noise ratio for detection i

$r(x,y)$ = range between map pixel at x,y and estimated array position for ping n_i where (x,y) are within 17 degree sector of the beam in which the detection occurred

γ_{map} = global map detection threshold

An additional constraint is that $E_i(x,y) > 0$; i.e. no negative energy summations are allowed.

3.2.2 Description of Algorithm

In other words, the algorithm involves integrating energy in the x-y plane. Each detection results in a concentration of energy in the form of an arc. The position of the buoy, range to detection, and beam number determine the location and orientation of the arc. The energy contained in the arc is determined by the signal to noise ratio of the detection. The probability density function of the arc, which describes the errors in range and angle, governs its shape.

In this example, the uniform probability of the azimuth causes the height of the arc to be constant along its width. The cross-section of the arc is determined by the probability density function of the range, however. The peak of the arc is equal to the signal to noise ratio of the detection and this value decreases quadratically with the range deviation. The width of the arc is directly proportional to the variance in the position measurement. Figure 3-5 illustrates the composition of the arcs. The arc in this figure is 17 degrees wide

and the buoy location is at [1900,1700], 158 meters away from the centerline of the arc. The signal to noise ratio of the arc is 10, so this is the maximum height of the arc and is the value at its centerline. The range standard deviation is set at 0.75 meters.

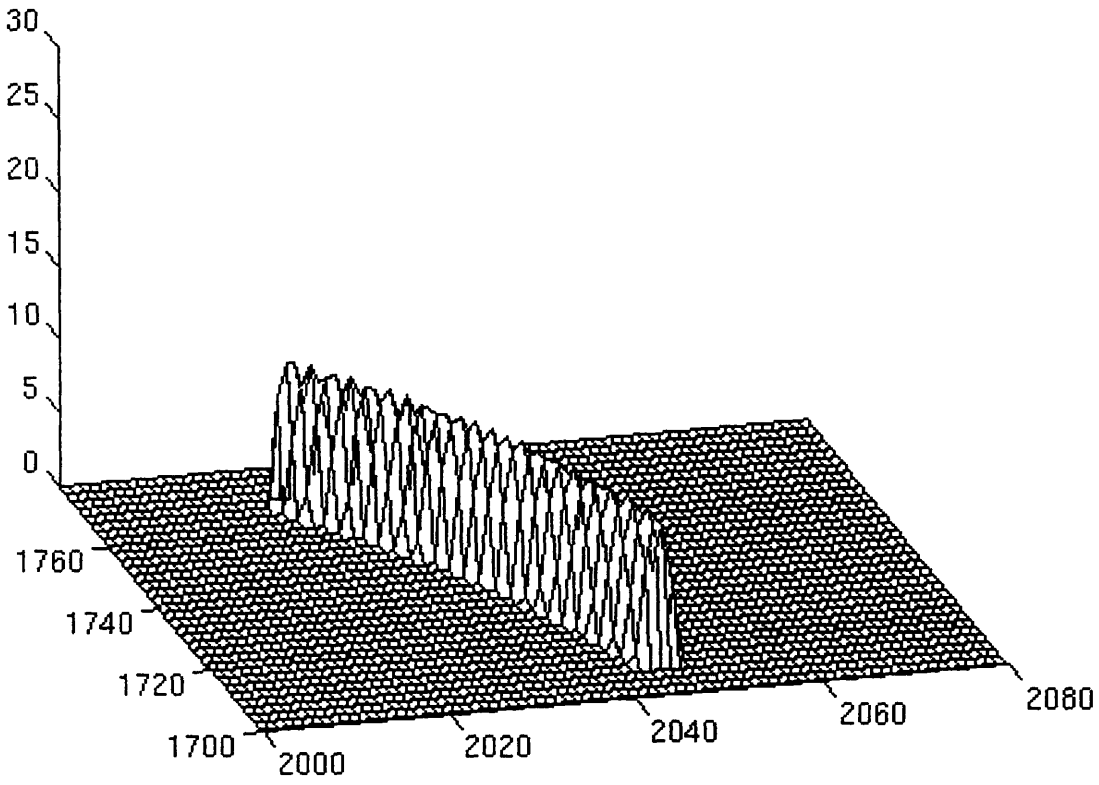

Figure 3-5 Three-dimensional View of Arc Structure

With just one arc, the position of the target in Figure 3-5 can only be determined within about 30 meters in the East-West direction and almost 70 meters in the North-South direction. As the buoy moves through the water it receives multiple detections of the same target. For each detection, another arc is added to the energy array of the target field. Multiple detections of the same target tend to intersect at the one point. The intersection of the arcs determines the location of the target. The method is analogous to triangulation of a location using multiple measurements. Figure 3-6 illustrates this technique.

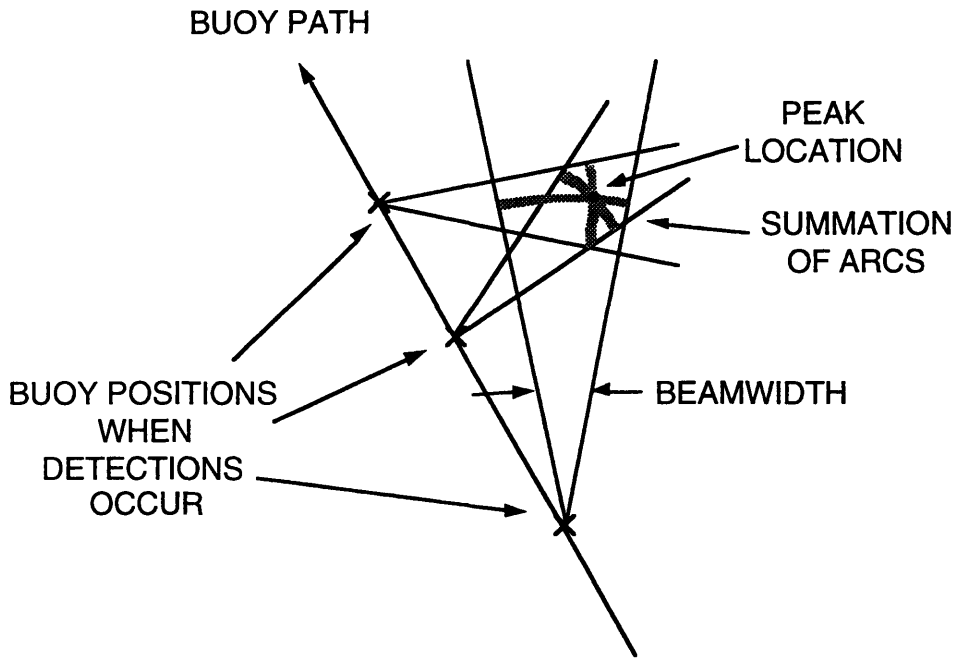

Figure 3-6 Map Construction Technique

The algorithm which implements this technique is shown in Figure 3-7. First the ends of the arc are found to determine whether the detection is in the area of interest. If so, then the energy contribution of every pixel within the arc is computed using equation [27]. Lastly, this energy contribution is added to the map plane.

In the absence of noise and positional error, two detections are all that is required to exactly locate the target source of those detections. The aspect angle granularity and aspect angle coverage explained in chapter 2 indicate that multiple detections of the same target are likely. This hypothesis is further supported by Figure 2-11, the B-Scan of the data. The B-Scan clearly shows tracks in the data that are created by multiple detections of the same target in consecutive pings. Additional detections of the same target further contribute to the peak and in doing so provide more resilience to noise and errors in measurement and buoy position.

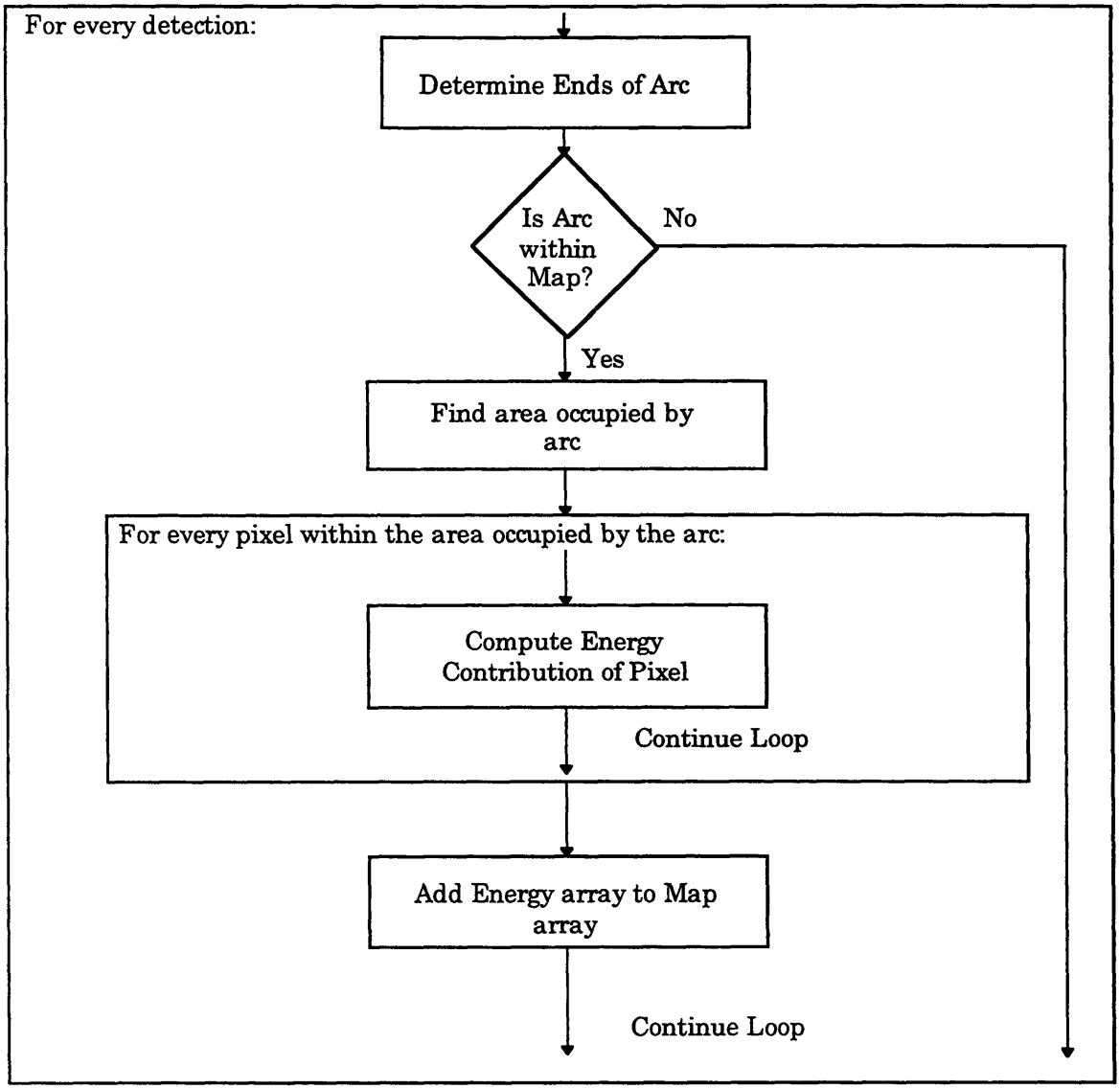

Figure 3-7 Energy Integration Algorithm

3.2.3 Simulated Data

This concept is clarified through the use of the following simulation. In the simulation, one cylinder has been placed in the target field at the coordinates [2050,1750]. The sonobuoy travels due North at a constant horizontal position of 2100 meters East. The buoy starts at 1600 meters North and transmits a ping every 5 meters until it reaches 1800 meters North. Therefore the simulation consists of 41 pings. The simulation geometry is depicted in Figure 3-8. This particular simulation takes into

account ambient noise, surface scattering, and bottom scattering, but assumes there is no positional error.

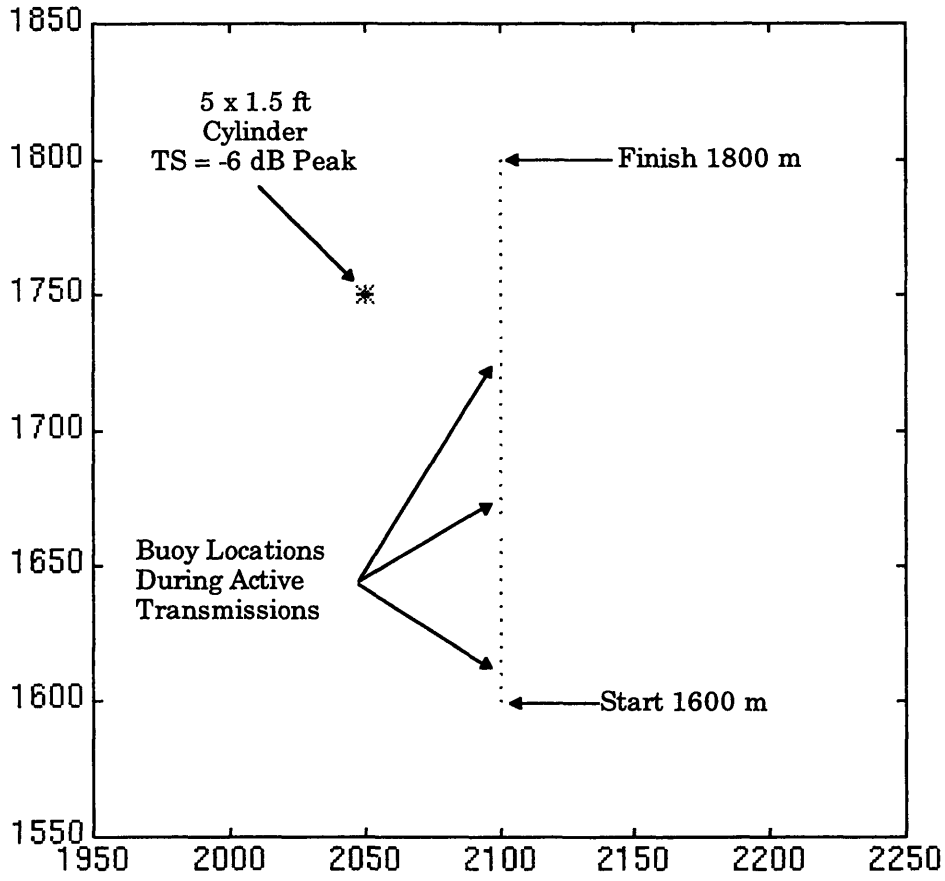

Figure 3-8 Simulation Geometry

The resulting energy-domain map made from this simulation is shown in Figure 3-9. This plot clearly shows the position of the cylinder at the proper location, [2050, 1750]. The vertical bar on the right side of the image is a key to the color map. The color map has been chosen to be bi-directional with dark values on both ends. This choice is effective because the structure of the energy is such that any dark colors at the high end of the color map are necessarily surrounded by lighter colors. In addition, the peak of the color map is scaled to the peak energy value in the plane. A similar color map will be used for all subsequent maps, except when noted otherwise.

Other characteristics of the plot deserve attention. First, the structure of the noise is very important. While the detections associated with the target tend to peak in one location, spurious detections caused by noise are distributed more evenly throughout the plane. This feature provides significant resistance to noise corruption. The maximum value of the energy at the target peak is almost 250, while the peak of the background does not rise about 100. The great separation between signal and noise is more readily seen in Figure 3-10. This map is a close-up of the area in the vicinity of the target. The color map has been adjusted to suppress the appearance of background noise. In essence, a threshold has been placed on the map to only display those pixels with an energy value greater than 95.

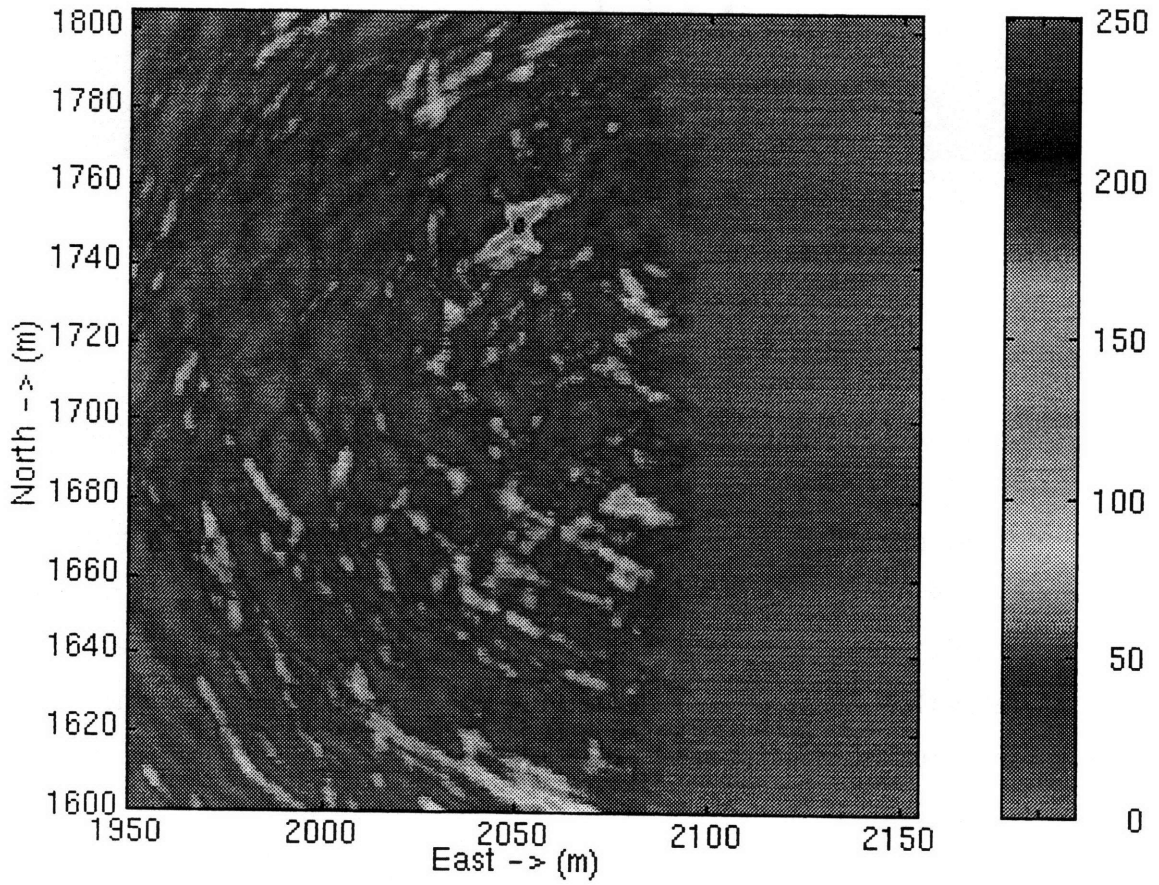

Figure 3-9 Energy Map using Cylinder Simulation

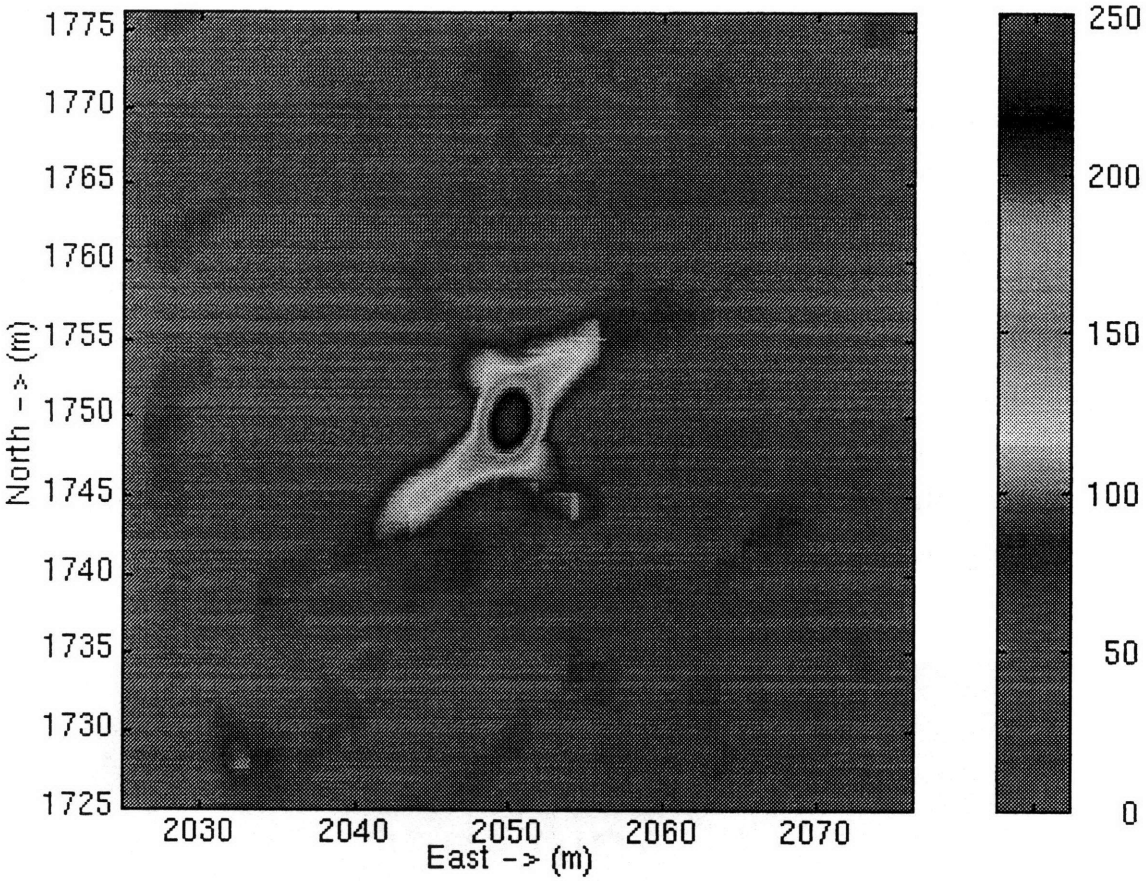

Figure 3-10 Close-up of Cylinder

The "X" shape of the energy plot in Figure 3-10 is also noteworthy. The target strength profile characteristics for the cylinder determine this shape. A higher target strength for the sides and end-caps of the cylinder creates stronger detections in those directions. A higher SNR leads to a higher number of detections in those directions as well. The cylinder orientation in this map is 240 degrees. Man-made objects may often be characterized by 90 degree corners such as this and will have a similar shape. Thus the shape of the return may provide a classification cue.

3.2.4 Test Data

Additional problems arise when dealing with actual test data. Although the simulation includes the effects of underwater noise, other sources of error affect localization results. Large detections appear in multiple beams and increase the arc uncertainty beyond 17 degrees. Errors in position caused by

problems with the GPS also have a considerable effect on target localization. The largest source of error was caused simply by the high number of sonar targets. This problem, introduced in chapter 2, causes interference among arcs in the energy domain. These problems will be explained in greater detail later in this section along with proposed solutions.

The subset of data used in this discussion comes from the October 5, North-South transit #1. An energy plot using the algorithm displayed in Figure 3-7 is shown in Figure 3-11. The white dots in the picture correspond to the locations of the buoy during pings. As the receive array for the prototype buoy is populated entirely on its left side, the sonobuoy is this example moved in a counter-clockwise direction. A comparison of this plot to the one in Figure 3-9 shows several key differences. The most obvious difference is that instead of a single peak with a well-defined structure, there are numerous peaks and a more complex structure. These differences are caused primarily by the presence of numerous targets of different amplitudes. A major concern is how to reduce this interference between various sonar targets.

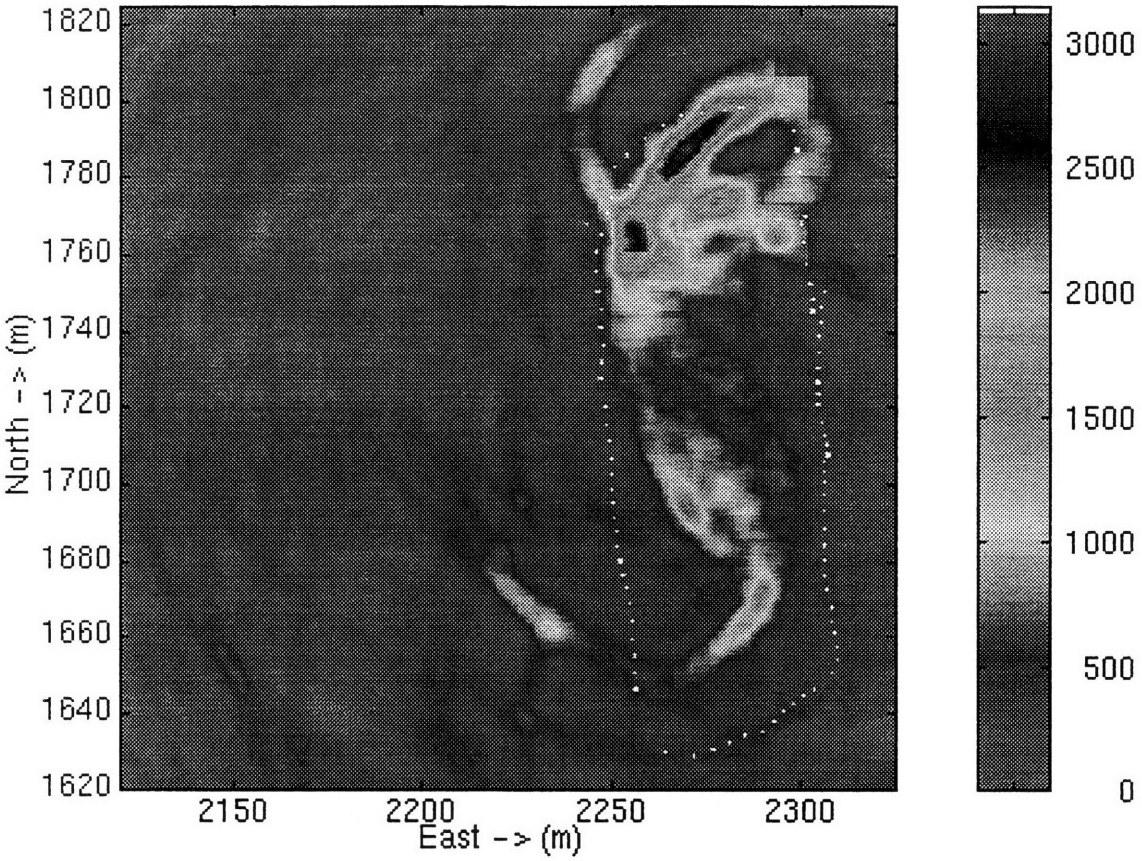

Figure 3-11 Energy Map using Actual Data

One reason why multiple targets have this interference problem is because of the wide azimuthal uncertainty. A major difficulty when using real data is that strong detections of the same object appear on multiple beams. This phenomena causes the angle uncertainty of the measurement to increase by 11.25 degrees for every additional beam in which the measurement occurred. In other words, a detection present in 6 adjacent beams creates an arc which is 73.25 degrees wide. In Table 2, a sample of the detection data is shown. This sample clearly shows that detections at a given range are present for multiple beams.

Ping #	Beam #	Range (m)	Bearing (degrees)	SNR (dB)	Echo Level (dB)
883	1	40.56	203.80	13.10	111.48
883	1	277.46	210.77	12.40	92.33
883	2	277.41	214.83	17.32	96.66
883	2	40.58	209.33	13.30	108.26
883	3	277.44	219.41	15.20	92.76
883	3	42.34	221.45	11.85	103.89
883	3	40.61	229.94	11.37	102.96
883	4	277.33	244.27	13.38	89.96
883	4	40.64	243.86	13.03	105.30
883	5	277.38	249.86	14.69	91.32
883	5	40.66	244.16	13.83	104.49
883	6	40.74	259.38	12.67	103.02
883	6	277.62	254.58	11.60	89.24
883	7	277.30	265.45	11.82	88.72
883	7	40.79	274.16	10.85	100.44
883	8	40.79	281.15	11.31	100.91
883	8	277.59	284.71	10.73	88.44
883	9	277.67	292.88	15.43	91.40
883	10	277.57	298.33	14.19	91.79

Table 2 Detection list array for real data

Long arcs cause several problems in the map building process. Foremost among these is the interference between detections of multiple targets. Another problem is the increase in uncertainty of the target location. Obviously, it is desirable to know the azimuth to the target as accurately as possible. For this problem, the resolution is desired to within the width of one beam.

Fortunately, the width of the beams helps to determine the proper location of the target. While detections exist on multiple beams for the same target, the beampattern causes the detection to be highest for the beam whose sector contains the target. Since the SNR also depends on the noise level for a given beam, the appropriate beam is the one which has the highest echo level, which is the maximum value of the signal for the detection.

An algorithm employed to reduce the problem of multiple detections for the same target is shown in Figure 3-12. Within the ping, detections which have approximately equivalent ranges are compared. Then, the detection with the highest echo level is chosen as the only detection for the given range bin.

The resolution of the range bin has been chosen to coincide with the range variance. The effective beamwidth has now dropped to 11.25 degrees, the distance between beam centers, because the ambiguity caused by the beam overlap has been removed.

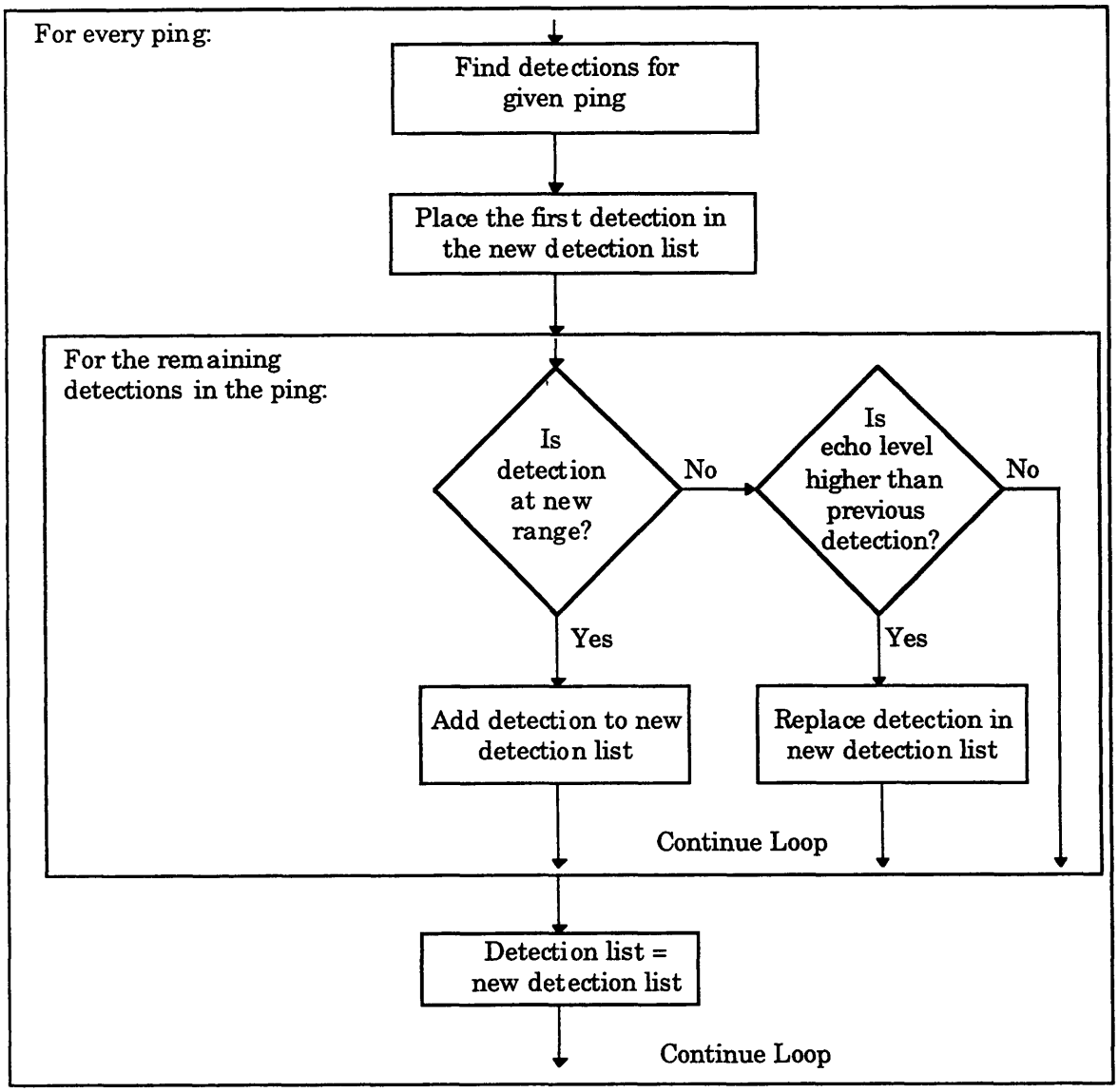

Figure 3-12 Local Ping Maximum Algorithm

Using this algorithm, the number of detections shown in Table 2 is reduced from 19 to only 2. The resulting map created after using this technique is shown in Figure 3-13. A comparison of this map with the map in

Figure 3-11 shows several key differences. First, the maximum value of the map has dropped considerably from 3100 to just over 1000. The number of detections which contributed to making the map decreased by a factor of 5, from 26002 to 5436. This reduction creates favorable results in the map domain. The amount of background noise in Figure 3-13 has also decreased considerably. Even more significant is the presence of an additional peak at location [2277, 1772]. In Figure 3-11, this peak was suppressed by the larger peak at [2282, 1766].

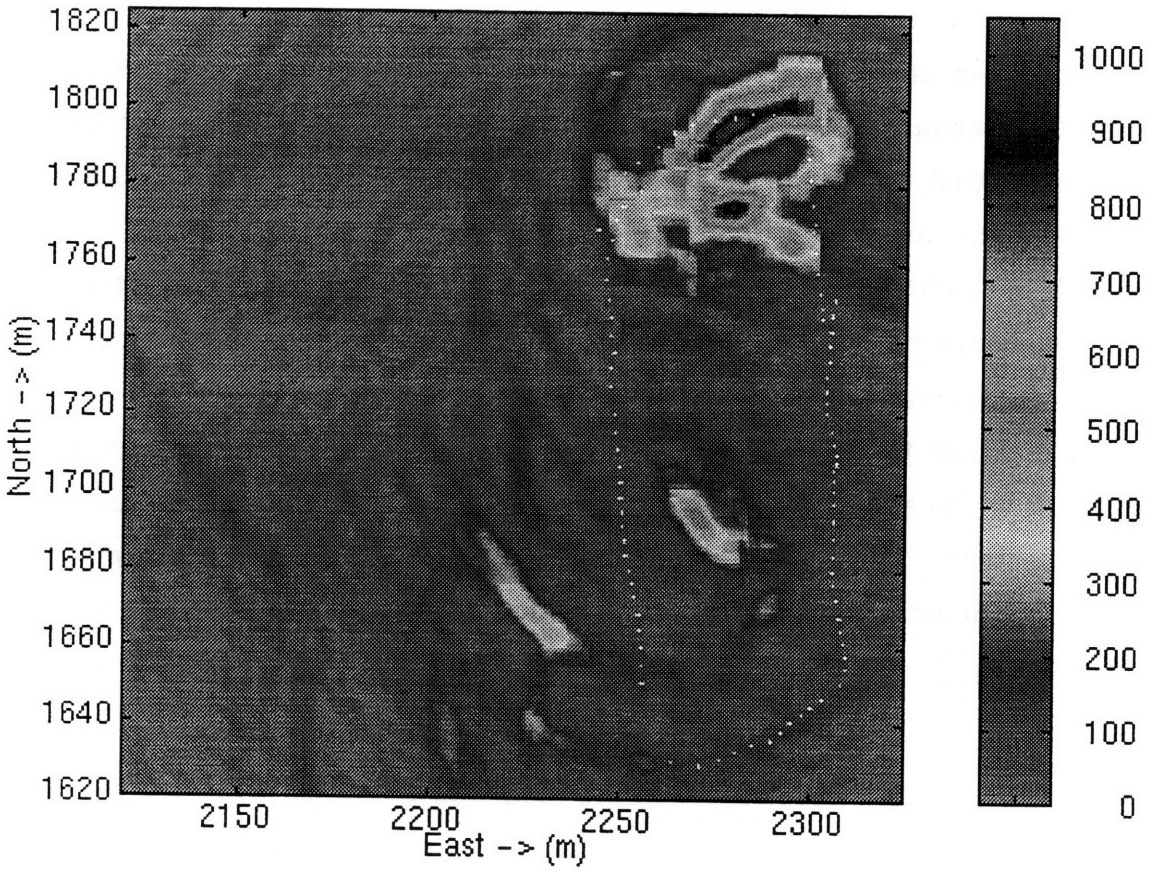

Figure 3-13 Map after Filtering Multiple Detections

Another problem is evident from the B-Scan data shown in Figure 2-11. The problem is that the maximum SNR of the arcs depends greatly on range. This causes targets with higher SNR values to completely overshadow those with lower SNR values. To counteract this effect, an additional modification has been to limit the SNR of all the detections which exceed the detection

threshold to the same value. Though this technique may not be optimal in a theoretical sense, the limiting has been observed to be useful on real data. A map showing the SNR limiting modification is pictured in Figure 3-14. The background only appears to be noisier in this picture because the color map has been scaled to the peak, which has dropped to approximately 270. The map in Figure 3-15 reflects a more comparable color map to the previous maps.

Again, several dissimilarities are worth noting. First, the value of the peak has again been reduced--this time by a factor of four from the previous map. The same algorithm described above to reduce the effect of multiple beams has been employed for this figure as well. The number of pings used in the past two examples has remained the same. The increased resolution of this map is owed, in part, to the decrease in SNR to the limiting value. Since the width of the arc is directly proportional to the SNR of the detection, a decrease in the SNR causes the arcs of energy to be narrower. This factor helps reduce the interference between arcs. Also, the desired objective to reduce the dominance of stronger detections has been achieved. In essence, the modifications to the original algorithm now involve adding the number of detections which exceed a given threshold, instead of the energy contribution of those detections. The peak values in the map are now roughly proportional to the number of detections passing through the peak location rather than the sum of energy.

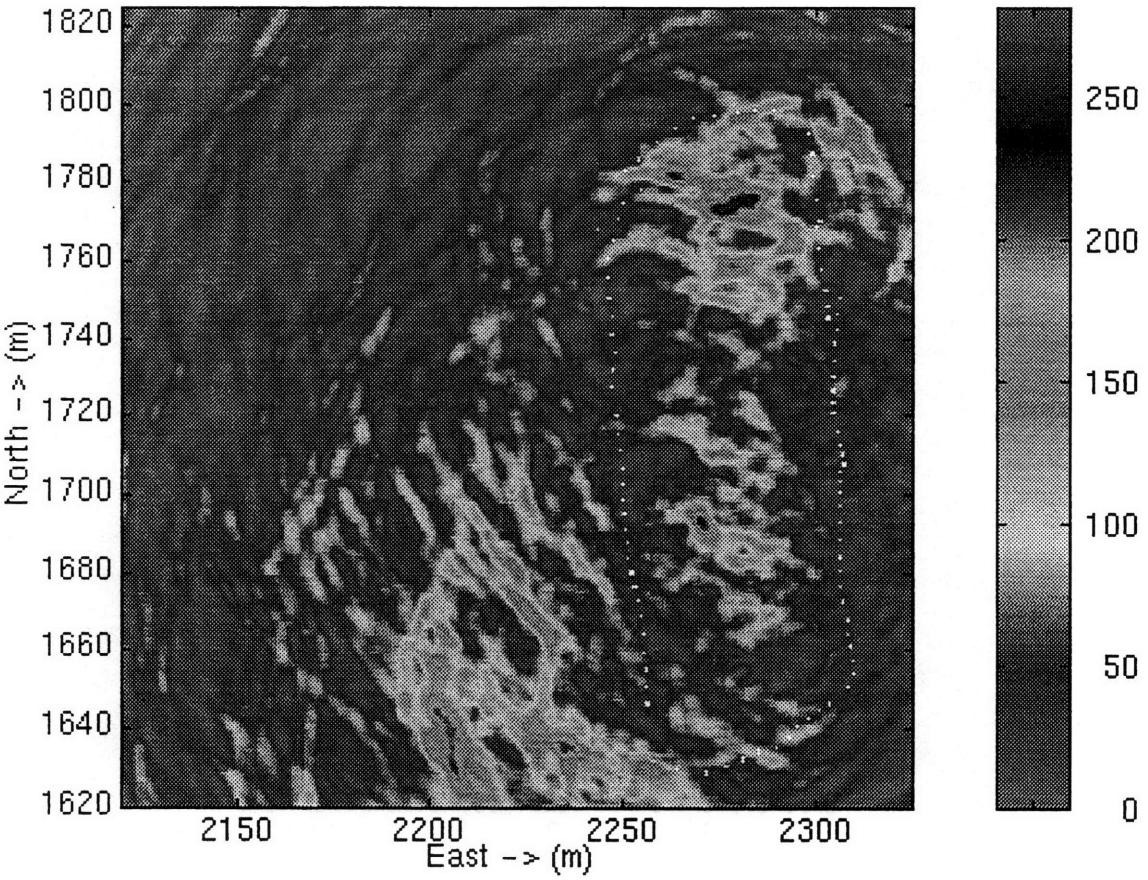

Figure 3-14 Map after SNR Limiting

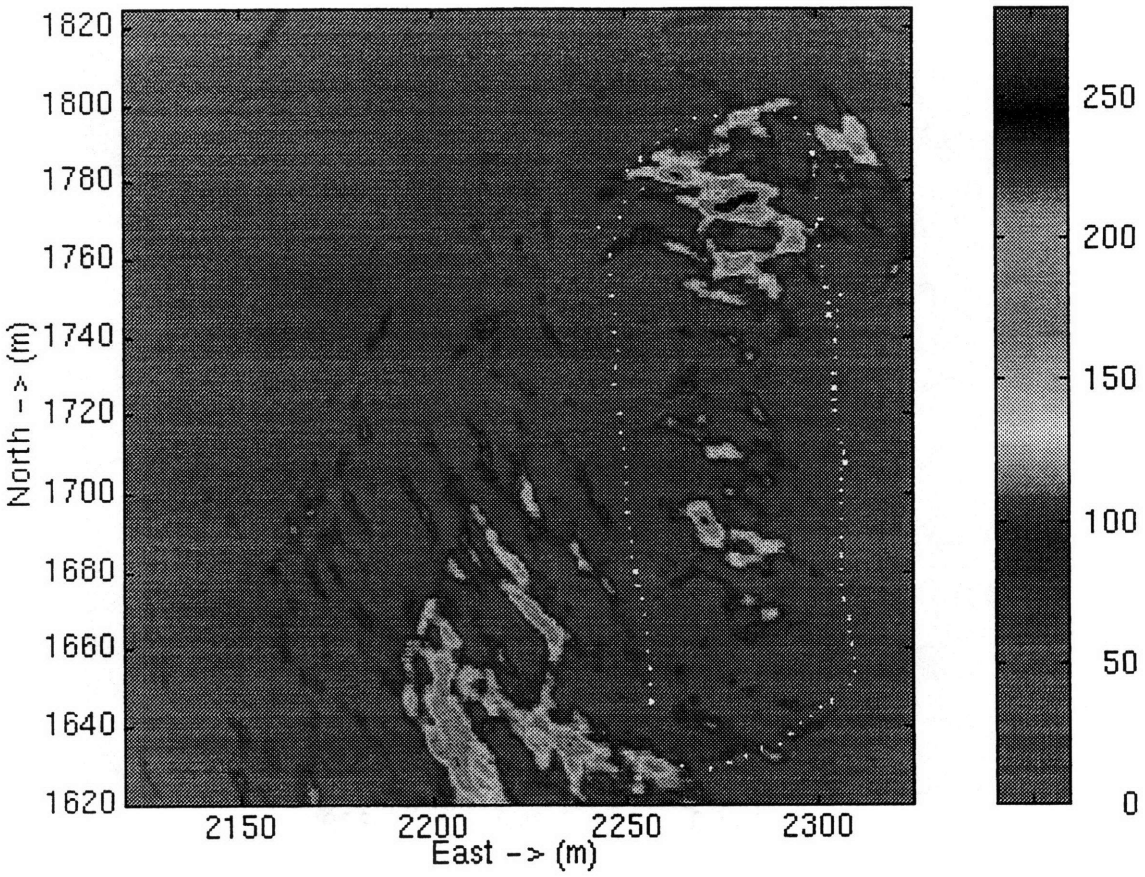

Figure 3-15 SNR Limiting with Thresholded Color Map

3.3 Monopulse Estimate

Until now the energy-integration algorithm has ignored the existence of the monopulse estimate. The monopulse estimate attempts to calculate the angle to the target to within the horizontal beamwidth.

The monopulse estimate is determined by first finding the complex ratio between the sumbeam and difference channels. The sumbeam channel is roughly equivalent to the sum of energies from all 6 receive staves which comprise the beam. The difference channel is the difference between the left half and right half of the beam. This ratio has a linear relationship to the direction cosine estimate in the horizontal direction. [15] For a complete discussion, the reader is advised to see [15].

With the conventional sensor, object resolution was limited the beamwidth of the individual beams. The monopulse sensor has improved upon that by estimating the angle to the target within the beam.

This new technique is simply a variation of the energy integration algorithm used in section 3.2. The derivation is also simply an extension of the algorithm previously covered.

3.3.1 Derivation of Algorithm

The derivation of the algorithm which uses the monopulse estimate is merely an extension of the previous algorithm in that now a measure of the angle uncertainty is given.

Example 4:

First assume a single measurement is made, range and angular estimate to the target are unknown.

In this case, the azimuthal uncertainty is shown to follow directly from examples 2 and 3. The hypotheses and assumptions remain the same and are listed below.

Hypotheses:

H_1: $Z_n = S_n + V_n$

H_0: $Z_n = V_n$

Assumptions:

S_n, V_n complex Gaussian signals

$E(S_n V_n) = 0$

$E(S_n) = E(V_n) = 0$

$\mathrm{Var}(Z_n \mid H_1) = \sigma_s^2 + \sigma_v^2$

$\mathrm{Var}(Z_n \mid H_0) = \sigma_v^2$

$\mathrm{Var}(\mathrm{Range}) = \sigma_r^2$

$\mathrm{Var}(\mathrm{Bearing}) = \sigma_\theta^2$

Detections are independent

The next step is the only major change. For a single detection the probability density function under H_1 becomes:

$$p_{z|H_1,\sigma_r}(Z \mid H_1) = \frac{1}{(2\pi)^2 \sigma_r \sigma_\theta (\sigma_s^2 + \sigma_v^2)^{1/2}} \exp\left(-\frac{1}{2(\sigma_s^2 + \sigma_v^2)} (|Z|^2) \right) \exp\left(-\frac{1}{2\sigma_r^2} (r_i - r(x,y))^2 \right) * \exp\left(-\frac{1}{2\sigma_\theta^2} (\theta_i - \theta(x,y))^2 \right) \quad (28)$$

After extending the hypothesis to multiple detections, such as was shown in the transition from example 2 to example 3, the probability density function for z given H_1 is:

$$p_{z|H_1,\sigma_r}(Z \mid H_1) = \prod_{i=1}^{N} \left\{ \begin{array}{l} \frac{1}{2\pi\left(\sigma_s^2+\sigma_v^2\right)^{1/2}} \frac{1}{\sqrt{2\pi}\sigma_r} \frac{1}{\sqrt{2\pi}\sigma_\theta} \exp\left(-\frac{1}{2\left(\sigma_s^2+\sigma_v^2\right)} \left(|Z_i|^2 \right) \right) * \\ \exp\left(-\frac{1}{2\sigma_r^2} \left(r_i - r(x,y) \right)^2 \right) \exp\left(-\frac{1}{2\sigma_\theta^2} \left(\theta_i - \theta(x,y) \right)^2 \right) \end{array} \right\} \quad (29)$$

The probability density function for z given H_0 is:

$$p_{z|H_0}(Z \mid H_0) = \prod_{i=1}^{N} \left\{ \frac{1}{2\pi\sigma_v} \exp\left(-\frac{1}{2\sigma_v^2} \left(|Z_i|^2 \right) \right) \right\} \quad (30)$$

Thus the likelihood ratio function for this example may be expressed as:

$$\Lambda(Z) = \frac{\prod_{i=1}^{N} \left\{ \begin{array}{l} \frac{1}{2\pi\left(\sigma_s^2+\sigma_v^2\right)^{1/2}} \frac{1}{\sqrt{2\pi}\sigma_r} \frac{1}{\sqrt{2\pi}\sigma_\theta} * \\ \exp\left(-\frac{1}{2\left(\sigma_s^2+\sigma_v^2\right)} \left(|Z_i|^2 \right) - \frac{1}{2\sigma_r^2} \left(r_i - r(x,y) \right)^2 - \frac{1}{2\sigma_\theta^2} \left(\theta_i - \theta(x,y) \right)^2 \right) \end{array} \right\}}{\prod_{i=1}^{N} \left\{ \frac{1}{2\pi\sigma_v} \exp\left(-\frac{1}{2\sigma_v^2} \left(|Z_i|^2 \right) \right) \right\}} \begin{array}{c} H_1 \\ > \\ < \\ H_0 \end{array} 1 \quad (31)$$

Applying the natural logarithm to both sides yields:

$$\ln \Lambda(Z) = N \ln \frac{1}{2\pi\left(\sigma_s^2+\sigma_v^2\right)^{1/2}} + N \ln \frac{1}{\sqrt{2\pi}\sigma_r} + N \ln \frac{1}{\sqrt{2\pi}\sigma_\theta} - N \ln \frac{1}{2\pi\sigma_v} - \frac{1}{2\left(\sigma_s^2+\sigma_v^2\right)} \sum_{i=1}^{N} |Z_i|^2 +$$

$$- \frac{1}{2\sigma_r^2} \sum_{i=1}^{N} \left(r_i - r(x,y) \right)^2 - \frac{1}{2\sigma_\theta^2} \sum_{i=1}^{N} \left(\theta_i - \theta(x,y) \right)^2 + \frac{1}{2\sigma_v^2} \sum_{i=1}^{N} |Z_i|^2 \begin{array}{c} H_1 \\ > \\ < \\ H_0 \end{array} 0 \quad (32)$$

Combining like terms:

$$-\frac{1}{2}\left(\frac{1}{\sigma_s^2+\sigma_v^2}-\frac{1}{\sigma_v^2}\right)\sum_{i=1}^{N}|Z_i|^2$$

$$-\frac{1}{2}\sum_{i=1}^{N}\frac{\left(r_i-r(x,y)\right)^2}{\sigma_r^2}-\frac{1}{2}\sum_{i=1}^{N}\frac{\left(\theta_i-\theta(x,y)\right)^2}{\sigma_\theta^2}\underset{H_0}{\overset{H_1}{\gtrless}}-N\ln\left(\frac{\sigma_v}{2\pi\sigma_r\sigma_\theta\left(\sigma_s^2+\sigma_v^2\right)^{1/2}}\right) \quad (33)$$

Finally:

$$\sum_{i=1}^{N}\left[\frac{|Z_i|^2}{\sigma_v^2}-\frac{\left(r_i-r(x,y)\right)^2}{\sigma_r^2}-\frac{\left(\theta_i-\theta(x,y)\right)^2}{\sigma_\theta^2}\right]\underset{H_0}{\overset{H_1}{\gtrless}}-2N\left(\frac{\sigma_s^2+\sigma_v^2}{\sigma_s^2}\right)\ln\left(\frac{\sigma_v}{2\pi\sigma_r\sigma_\theta\left(\sigma_s^2+\sigma_v^2\right)^{1/2}}\right) \quad (34)$$

This formula may also be expressed in terms of the detection SNR:

$$E(x,y)=\sum_{i=1}^{N_{det}}\left[snr_i-\frac{\left(r_i-r(x,y)\right)^2}{\sigma_r^2}-\frac{\left(\theta_i-\theta(x,y)\right)^2}{\sigma_\theta^2}\right]\underset{H_0}{\overset{H_1}{\gtrless}}\gamma_{map} \quad (35)$$

3.3.2 Description of Algorithm

Once again, the algorithm requires integrating energy in the x-y plane. The orientation of the arc is now determined by the monopulse angle estimate instead of the beam number. The shape of the arc has also changed considerably. Now the shape of the arc is defined completely by equation [35]. The peak position of the arc is determined by the measured range and monopulse angle estimate and the height at this point is equal to the SNR of the detection. Both the width and cross-section of the arc decrease

quadratically at a rate according to the appropriate variances in those directions. Thus along the centerline of the arc, the height of the arc is determined solely by the deviation in angle from the monopulse estimate. Figure 3-16 illustrates the structure of these arcs. The position of the buoy in this picture is the same as before, but the shape of the arc is considerably different than the arc shown in Figure 3-5. For this arc, the signal to noise ratio is 10, the range standard deviation is .75, and the azimuthal standard deviation is set at 3 degrees.

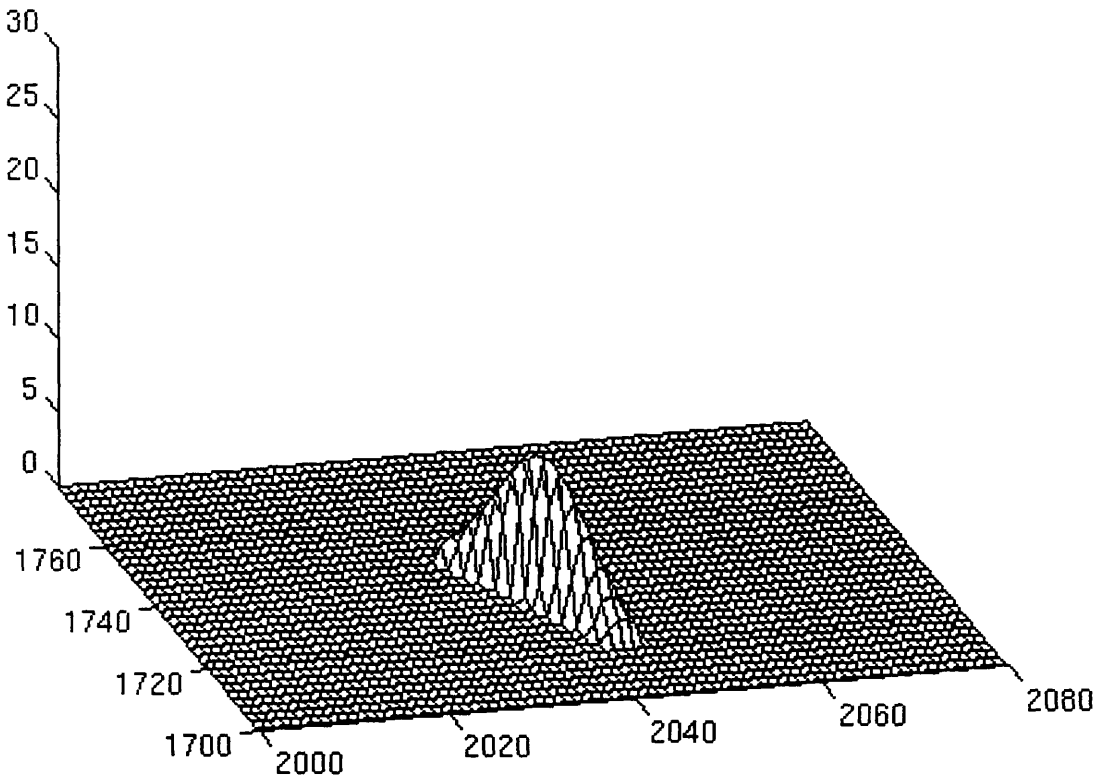

Figure 3-16 Three-dimensional View of Monopulse Arc Structure

A major change with this new technique is that the target location can be determined exactly with only one detection. This is a big improvement over the previous method, but obviously depends on the accuracy of the monopulse estimate in addition to the other measurements. Additional detections of the same target again tend to intersect at the same point and provide resilience to noise in the measurements.

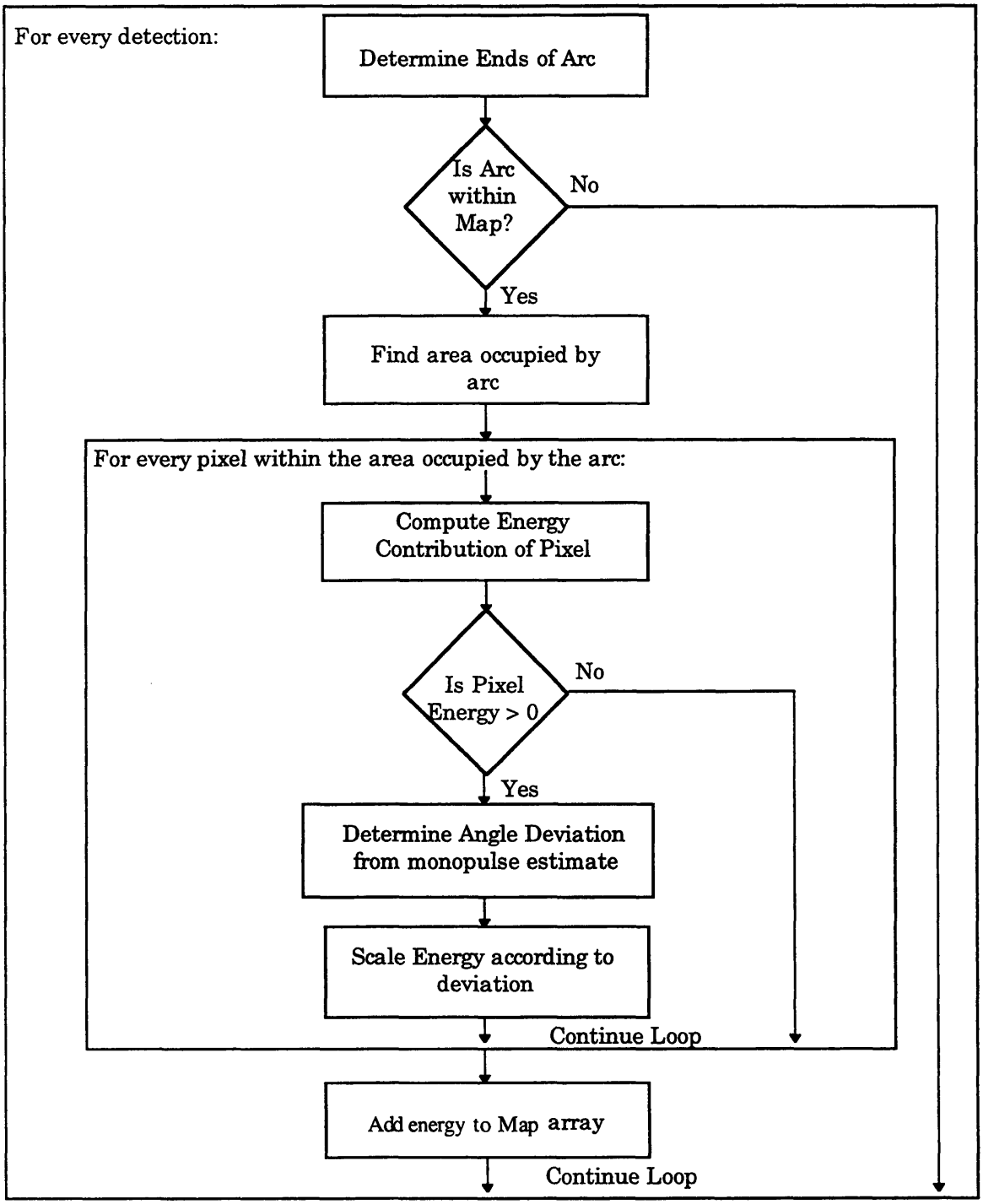

Figure 3-17 Monopulse Energy Integration Algorithm

The algorithm implemented in software for the modified technique is shown in Figure 3-17. This flowchart is very similar to the one in Figure 3-7, however the major difference is that for each pixel with positive energy, the

energy contribution is reduced according to the deviation in angle between the pixel to the buoy and the monopulse estimate.

3.3.3 Simulated Data

For comparison purposes, the simulation environment has been kept the same as before. This environment is portrayed in Figure 3-8. Once again, the simulation takes into account the effects of various sources of sonar noise, while assuming there is no positional error. The same detection list is used in this simulation as in the previous one.

The resulting energy-domain map made from this simulation is shown in Figure 3-18. This plot once again clearly shows the position of the cylinder at the proper location, [2050, 1750]. The plot also exhibits a similar noise structure as before, with the background noise distributed evenly throughout the plane. The peak has dropped slightly from about 250 to just over 200. The reason for this is that the amount of energy contained in the new arcs has decreased. This has caused the peak energy in the background to drop considerably from 100 to less than 50, and has created an even larger signal to noise ratio between the target and the background. This difference is again more evident in a close-up of the target area in which a threshold has been applied to the color map of the image. This threshold is set at 20% of the peak value, or approximately 45.

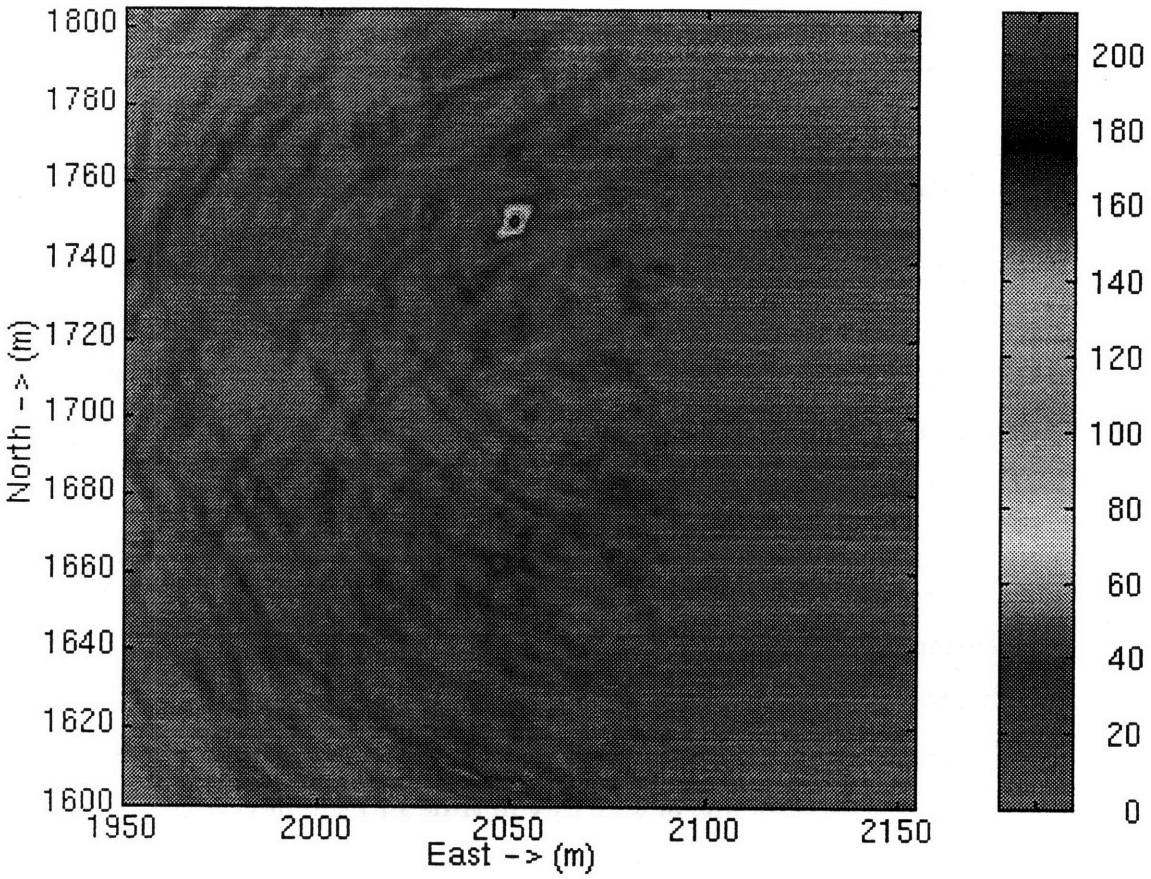

Figure 3-18 Energy Map using Monopulse Estimate

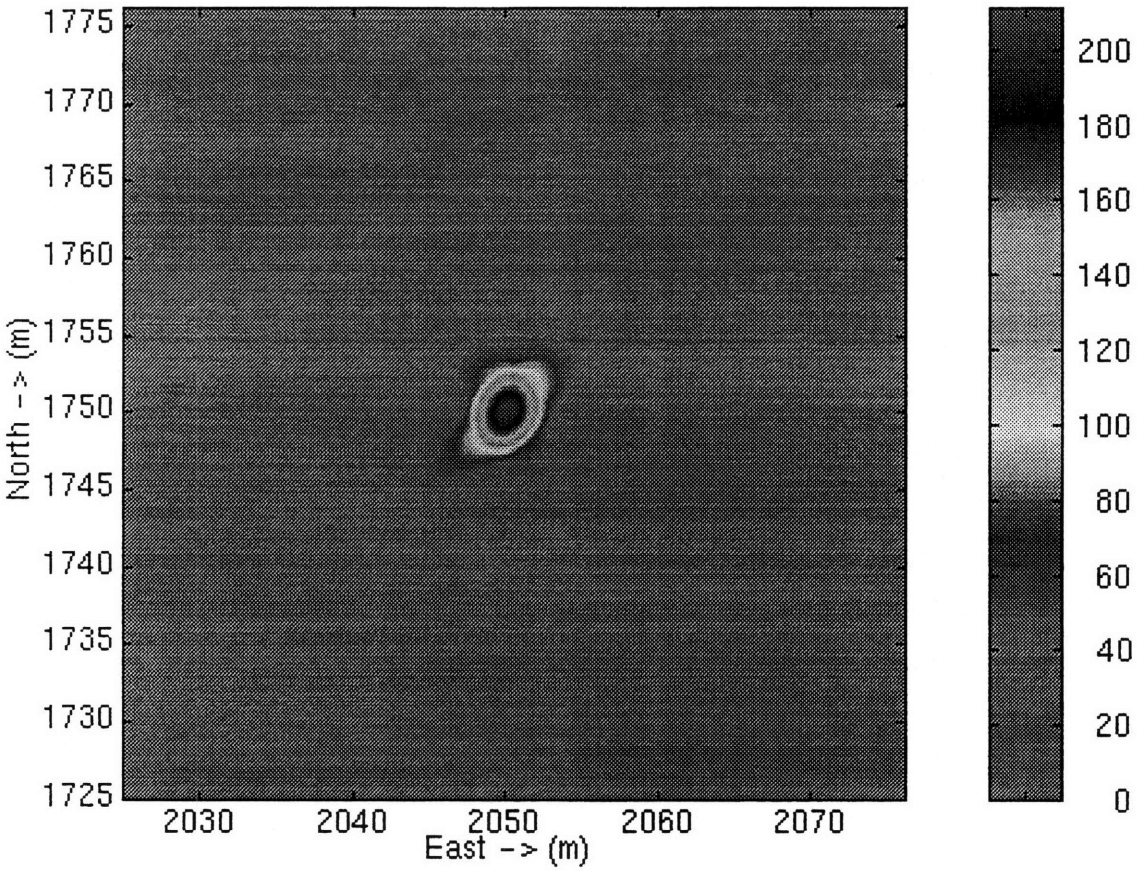

Figure 3-19 Close-up Using Monopulse

The close-up image in Figure 3-19 shows the clear the distinction between target and background for this image. With the background threshold set at only 20%, almost all the visible energy in the plane is associated with the target. One change in Figure 3-19 as compared to Figure 3-10 is that the characteristic "X" shape is now less noticeable. This is due to the fact that the individual arcs which make up the image are now considerably narrower. The close-up image also shows that the image is now much smoother since the jagged edges at the ends of the arcs have been removed.

3.3.4 Test Data

With the actual test data, there are again problems due to multiple detections of the same target with different beams. Instead of a continuous arc such as in section 3.2, the spurious detections instead are now spread at various angles for the given range. While this poses less of a problem to the map building algorithm, these detections still interfere with the background

noise and can create false peaks or mask smaller, true peaks. For these reasons, the local ping maximum algorithm described in Figure 3-12 and the SNR limiting have again been applied.

A resulting map created using the monopulse estimate is shown in Figure 3-20. This map should be compared with the map in Figure 3-14. Next a threshold was applied to the background of this map and the new map is shown in Figure 3-21. This map is closely comparable to Figure 3-15, the thresholded version without using the monopulse estimate. Comparing these two maps, the map created using the monopulse estimate does not have the same jagged edges that the map without the monopulse estimate exhibits. These jagged edges are artifacts of the map-building process which result from the discontinuities at the ends of those arcs. The maps created with the monopulse estimate use arcs which have been smoothed in both directions and therefore do not suffer from these problems.

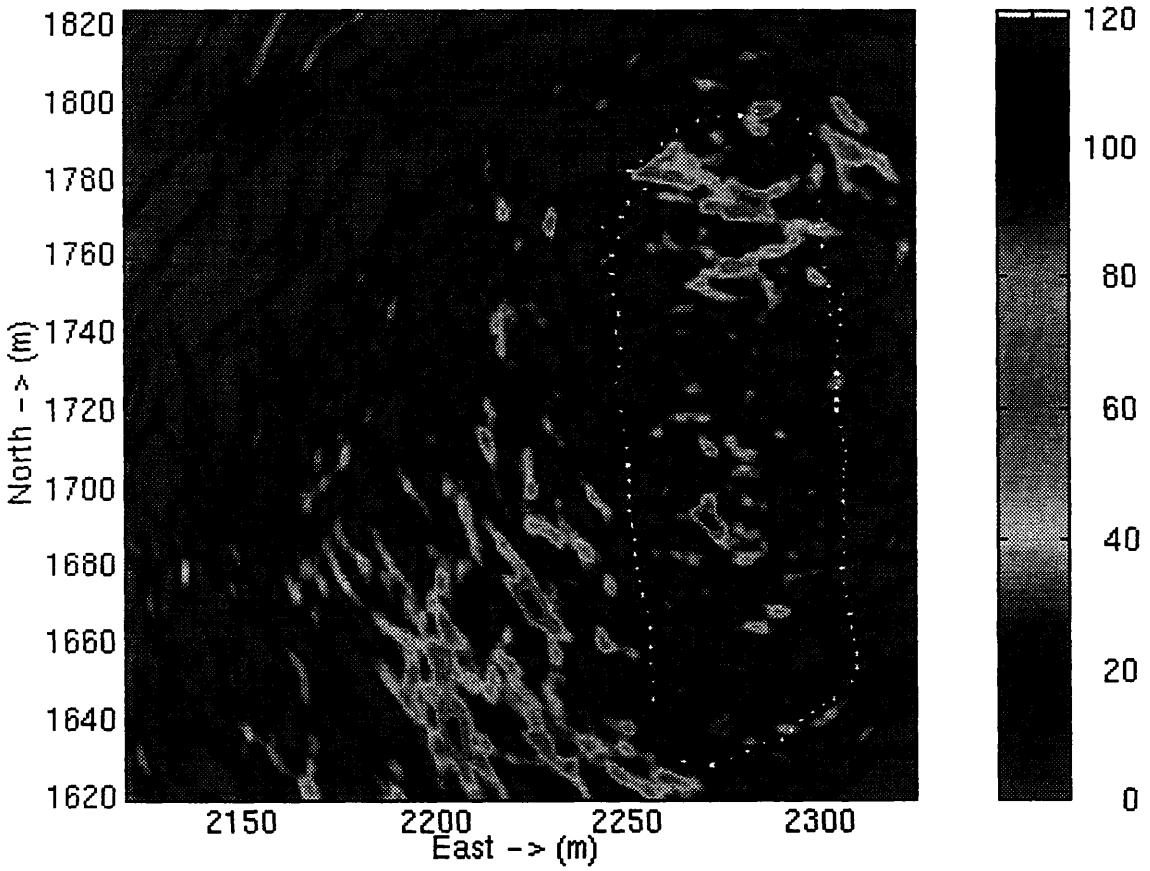

Figure 3-20 Energy Map using Monopulse Estimate

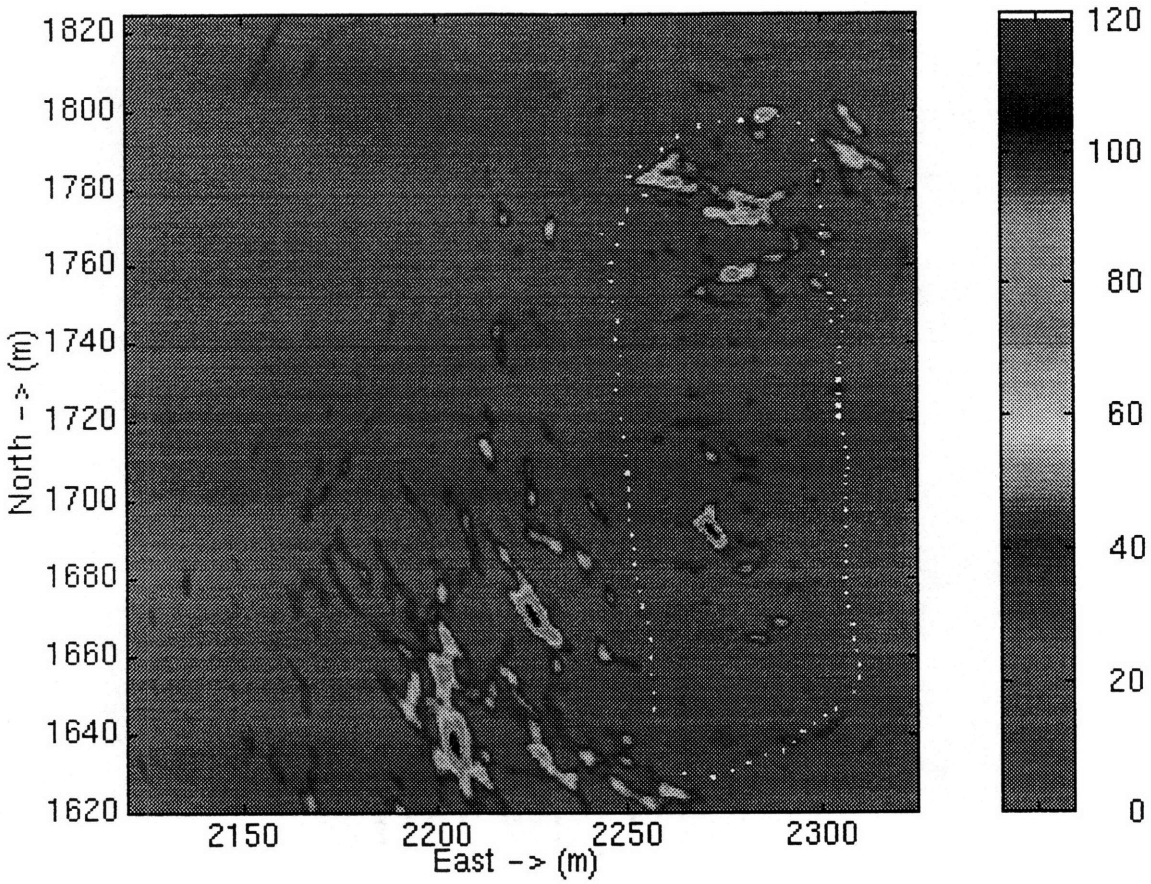

Figure 3-21 Monopulse Estimate with Thresholded Color map

The map created with the monopulse estimate has a more well-defined structure than the map created without using the estimate. This results primarily because of the smaller arcs and less jagged structure. The benefits of these characteristics include higher signal to noise ratio and less interference between arcs and are visible in Figure 3-21.

3.4 Hough Transform

The Hough Transform will next be used as a comparison to the energy integration method. The Hough Transform is a clustering algorithm commonly used in computer vision problems. Lately, it has received use in such wide-ranging applications as silicon wafer fault detection and target tracking. The Hough Transform was first introduced as a method of detecting complex curves in binary image data. It operates on the notion that the parameters of the curves and the resulting image space are mutually constrained by the

same equation. Points which lie along a common curve are characterized by the same parameters. The global curve detection problem in the image space has transformed into a peak detection problem in the parameter space. A common and straightforward application of the Hough transform has been to find straight lines in images.

3.4.1 Derivation of Algorithm

A series of collinear points may be described by the relation, f, such that:

$$f\left((\hat{m},\hat{c}),(x,y)\right) = y - \hat{m}x - \hat{c} = 0 \tag{36}$$

where $\hat{m}$ and $\hat{c}$ are the slope and intercept of the line connecting those points.

The Hough transform shows that equation [36] defines a mutual constraint between the parameter space and the image space. So, instead of using a set of parameters such as the slope and intercept to map from the parameter space to the image space, a single point (x,y) can be used to map from the image space to the parameter space. The possible parameter values are those which define the set of all possible lines which pass through the image point. This operation is called backprojection of the image point and is given by the relationship shown below:

$$g\left((\hat{x},\hat{y}),(m,c)\right) = \hat{y} - \hat{x}m - c = 0 \tag{37}$$

Thus for straight lines, each point in the image space defines a straight line in the parameter space. Points which are collinear in the image space intersect at a single point in the parameter space. This coordinates of this point in the parameter space then defines the straight line which connects the points in the image space. [16]

A problem with the slope-intercept parameterization scheme is that both the slope and intercept are unbounded. In an influential paper, Duda and Hart modify Hough's technique to use the normal parameterization. [17] This parameterization, shown in Figure 3-22, describes a straight line by the angle,

theta, of its normal and the distance, rho, from the origin. The equation of this line is given by:

$$x \cos\theta + y \sin\theta = \rho \tag{38}$$

Once again, every point in the image space corresponds to a line in the parameter space. This time the lines in the parameter space are sinusoidal curves, as shown in Figure 3-23.

In order to find a straight line through a series of points (x_i, y_i) the same process is followed as before. The points must first be converted to sinusoidal curves in the parameter space. These curves are given by:

$$\rho = x_i \cos\theta + y_i \sin\theta \tag{39}$$

Curves corresponding to a straight line in the image space have a common point of intersection in the parameter space. This point in the parameter space is the normal parameterization for the line connecting those points. Figure 3-22 shows a set of collinear points in the image space and the line which connects those points. After performing the Hough Transform, the corresponding lines in the parameter space are shown in Figure 3-23. The point of intersection for those lines is defined by the parameters, ρ and θ, for the normal parameterization of the straight line which connects the points in the image space.

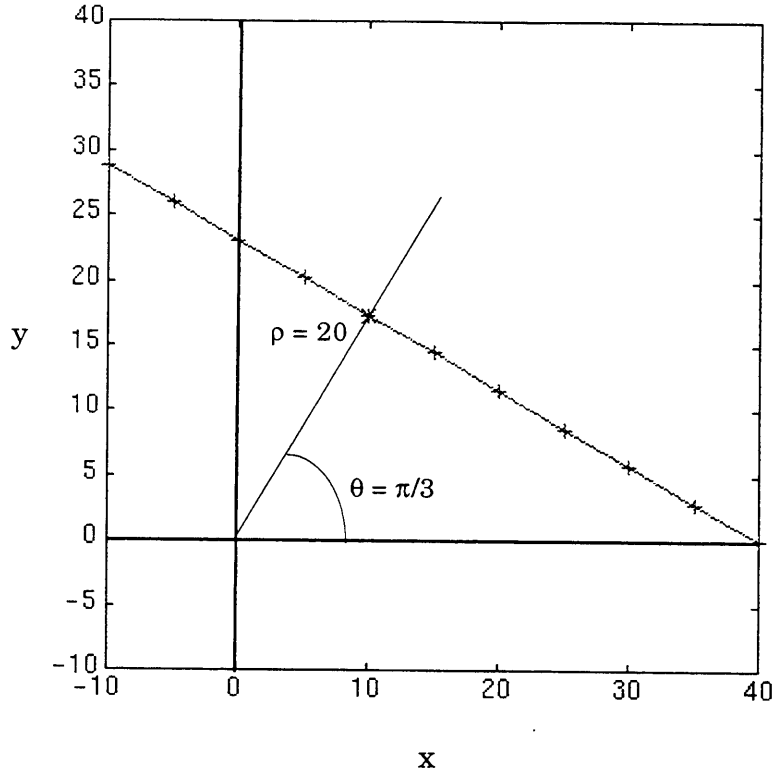

Figure 3-22 Collinear Points in Image Space

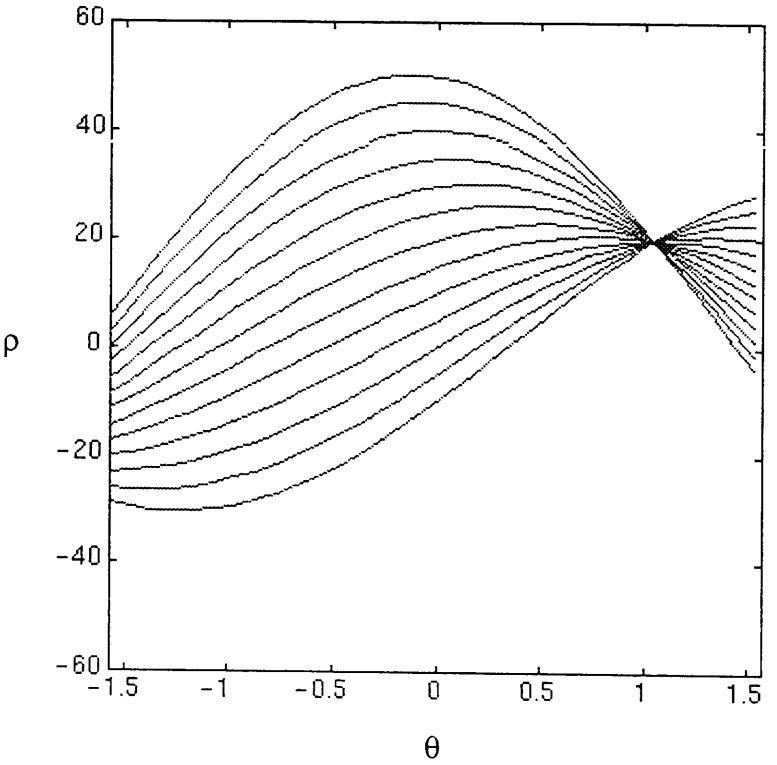

Figure 3-23 Sinusoidal Curves in Parameter Space

A summary of the transformation between image space and the normal parameterization space follows:

Property 1. A point in the image plane corresponds to a sinusoidal curve in the parameter plane.

Property 2. A point in the parameter plane corresponds to a straight line in the image plane.

Property 3. Points lying on the same straight line in the image plane correspond to curves through a common point in the parameter plane.

Property 4. Points lying on the same curve in the parameter plane correspond to lines through the same point in the picture plane.

Using the method described above, exactly collinear sets of image points can be found. A set of n points in the image space are transformed into n curves in the parameter space. These n curves intersect in n(n-1)/2 points, which correspond to the set of all possible lines between pairs of points. The problem becomes quite cumbersome as the value of n increases. Also, many times in images, the points are only approximately collinear and a linear approximation is required. Both problems can potentially be solved by properly quantizing the parameter space.

In order to quantize the parameter space, it is first necessary to determine the acceptable amount of error in both the range and in angle. The parameter space is then treated as a two dimensional array of accumulators. A discrete curve in the parameter space is created for every point in the image space. The value in the accumulators which lie along the curve are then incremented. This process is repeated for every detection. Multiple curves intersecting at a common point cause the accumulator value for the bin containing that point to be a local maximum.

The accumulator for the quantized version of the previous example appears in Figure 3-24. The white area in the image corresponds to all 13

curves passing through that point. The light gray areas correspond to areas containing 2 curves, and the dark gray areas contain only one curve. The bin size used in this example is relatively coarse with a single bin corresponding to 2 units of range resolution and 10 degrees of angular resolution. The peak of this graph is at a value of 60 degrees or pi/3 for the angle and 20 for the range. These numbers agree with the predicted values from the earlier graphs.

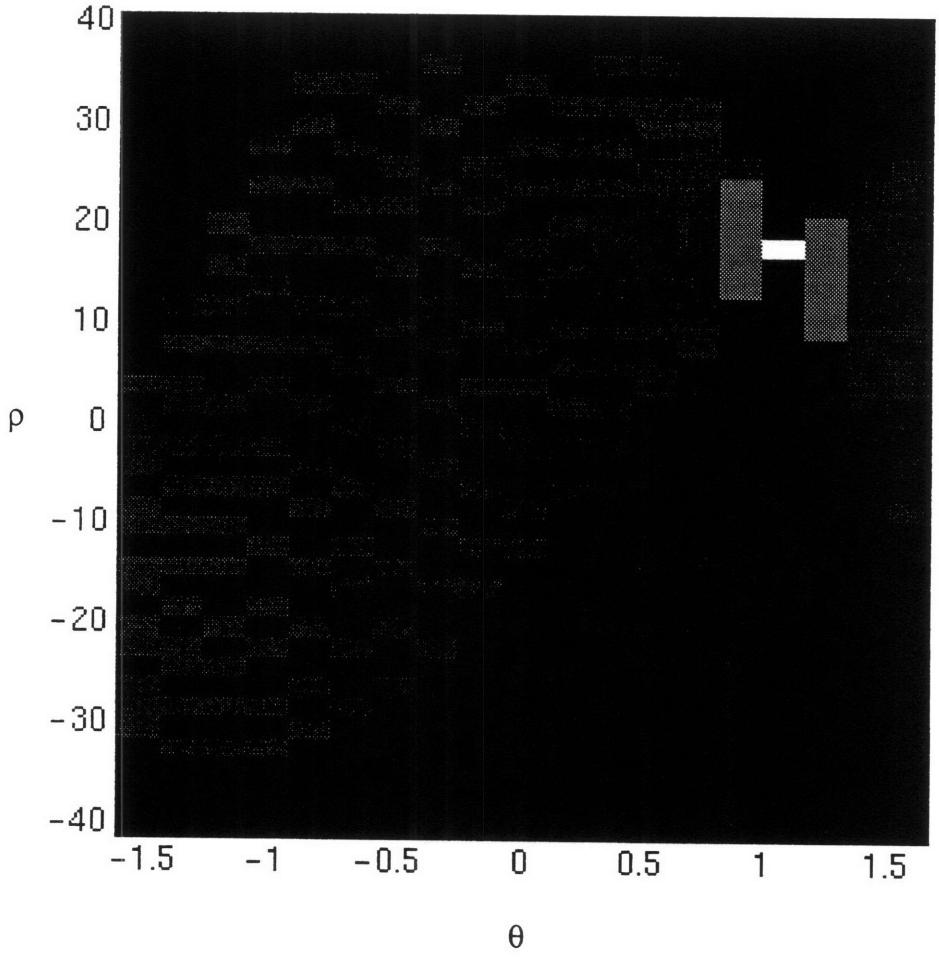

Figure 3-24 Two-dimensional Accumulator Array

3.4.2 Application to Sonar Problem

The Hough Transform has been shown to be useful as a clustering technique for collinear image points. The targets in the sonar problem described in section 3.1 do not move, though. If the buoy position is assumed to be fixed, however, the targets 'move' in a manner according to the path of the

buoy. This reference frame was first introduced in Figure 2-4. In this reference frame every detection creates a new point in the image space. We will assume for now that the buoy moves only in straight lines. The Hough transform can then be used to determine the straight line created by the targets. These lines are also convenient in that they are parallel to the buoy track and thus the angle of the target track is known. This reduces the number of operations which must be performed to calculate the accumulator array.

The algorithm used to apply the Hough Transform to this sonar problem is shown in Figure 3-25. After computing the Hough Transform of the sonar data, additional post-processing must be accomplished to determine the position of the target. This is because the straight line only tells the x-offset from the buoy and not the y-offset from the fixed buoy location.

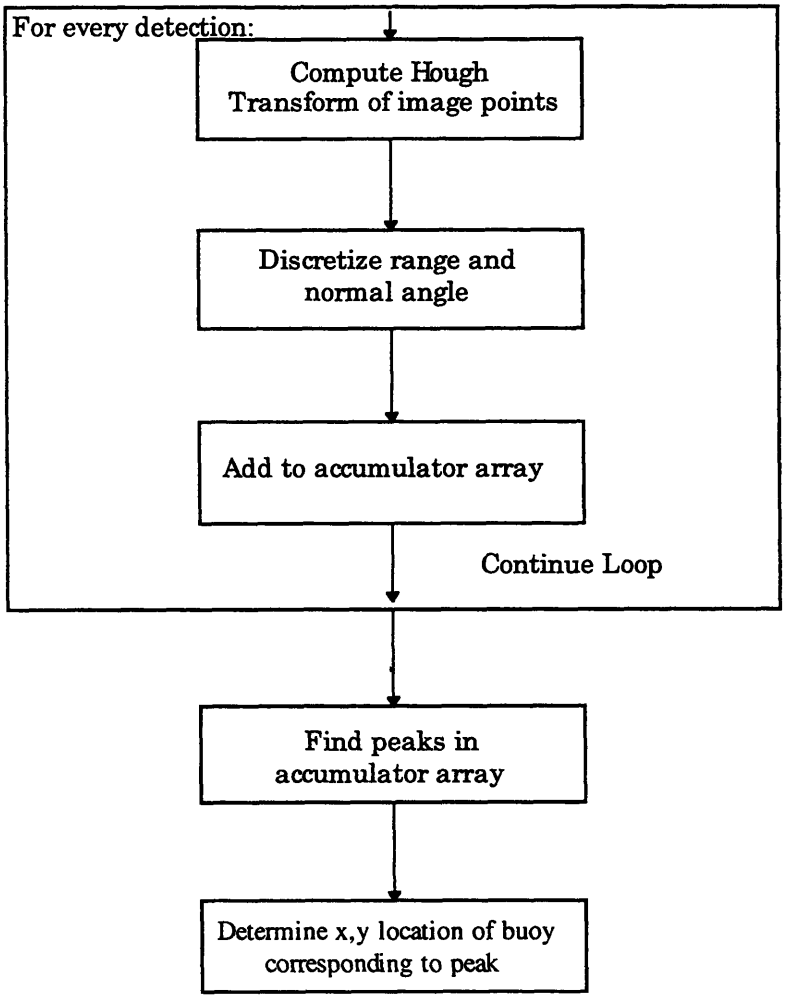

Figure 3-25 Target Localization Algorithm

3.4.3 Simulated Data

Now we will apply the Hough Transform to the same simulation described in section 3.2. This simulation consists of a cylinder at location [2050, 1750]. The buoy in the simulation moves along a vertical line from 1600 meters north to 1800 meters north. Assuming a fixed location for the buoy, the cylindrical target then moves along a vertical line.

A plot of the accumulator array in the parameter space for this simulation is shown in Figure 3-26. The bright spot in the bottom center of the image denotes the peak number of detections in the map at (0°, -50 m). This means that the line passing through the target points is vertical and 50 meters

to the left of the buoy location. This result is verified by the simulation geometry.

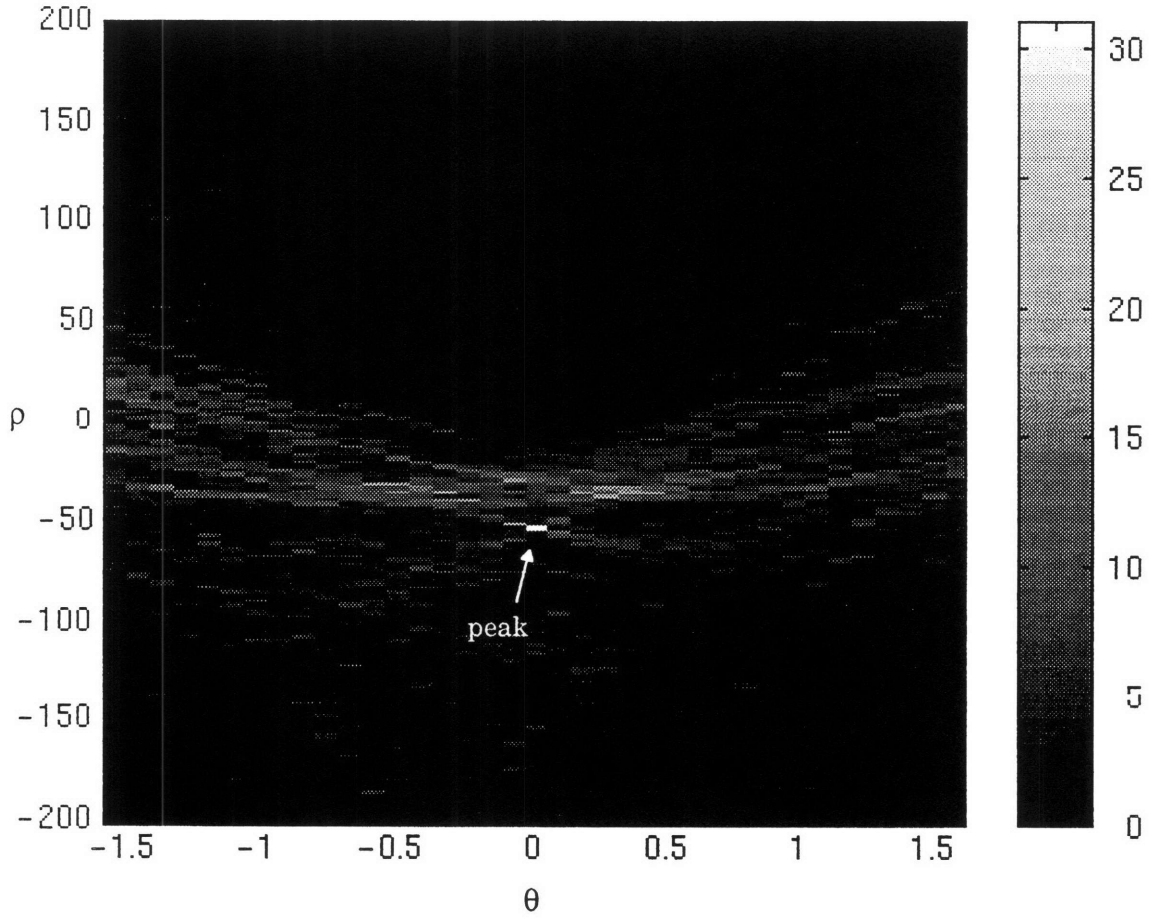

Figure 3-26 Accumulator Array for Simulation

A two-dimensional display of the number of intersections along the rho axis is shown in Figure 3-27. This plot once again shows the peak of 30 intersections with a range of -50 meters. This means that 30 points in the image space lie along that same vertical line.

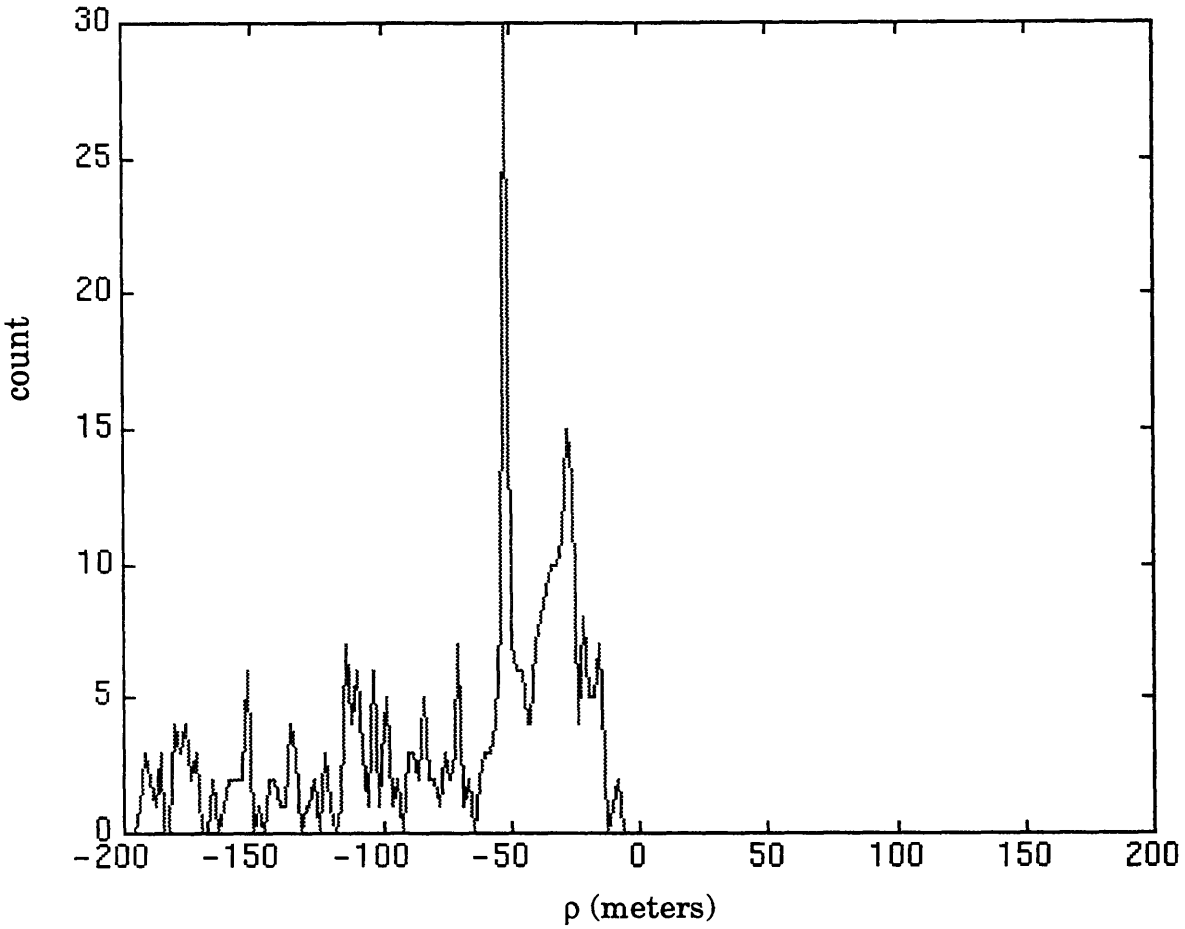

Figure 3-27 Accumulator Array at Rho Axis

As the flow chart in Figure 3-25 indicates, the task is not yet finished. While the Hough transform yields the cross-track offset from the buoy's track, it does not contain information concerning the vertical offset of the target. Once the peak in the accumulator array is found, the detections contributing to that point are next isolated. A plot of the range vs. ping number for those points is displayed in Figure 3-28. This plot is similar to the B-Scan plot, except that the clustering algorithm has already automatically filtered these points from the main detection list. The vertical offset can then be determined as the minimum value of the hyperbola. The range value at this point is approximately equivalent to the value of rho determined earlier. In this example, ping 31 corresponds to that range value and this buoy location at this

point is [2100, 1750]. Thus the target location has been correctly identified at [2050, 1750].

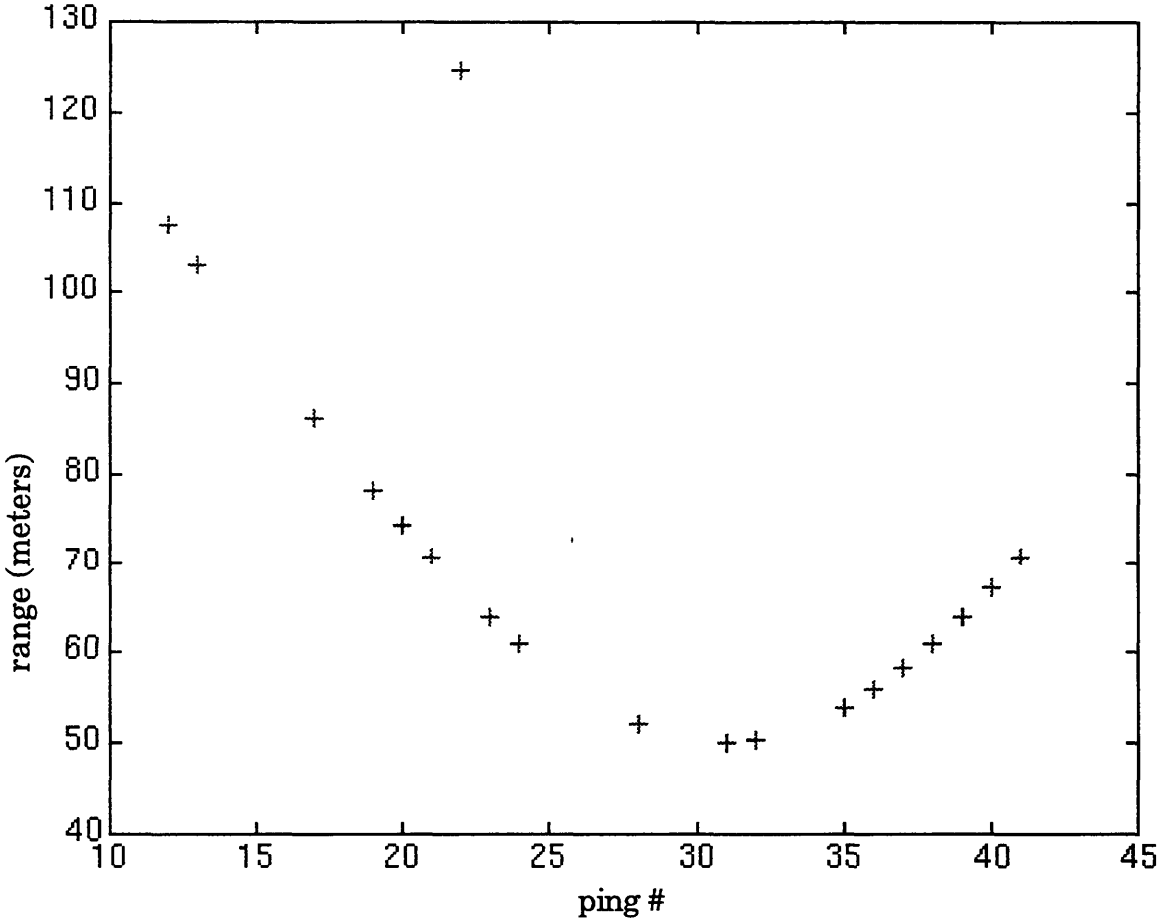

Figure 3-28 Range vs. Ping Number

3.4.4 Test Data

Lastly, the Hough Transform will be applied to actual test data. The subset of data used for this test is pings 895-934 from the October 5, North-South transit #1. A plot of the accumulator array for this test is shown in Figure 3-29. The data in this image is much noisier than in the simulation. Also, several peaks are evident in this figure. Although some of the peaks appear at aspect angles away from the rho axis, a majority of the energy is concentrated along that line.

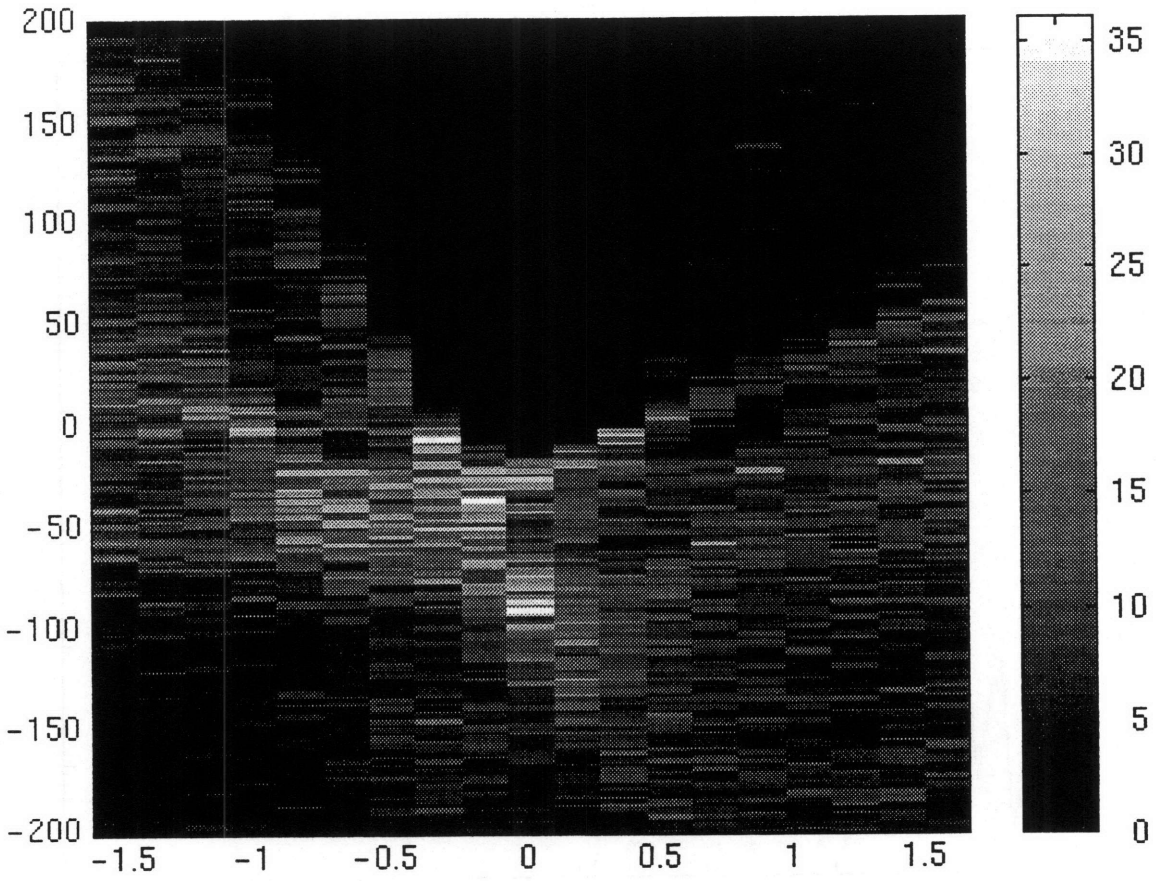

Figure 3-29 Accumulator Array for Test Data

The energy at the rho axis can be seen more clearly in Figure 3-30. This plot differs from the one in Figure 3-27 in that several peaks are evident in the data. This is expected because there are several known and many more unknown targets in the target field.

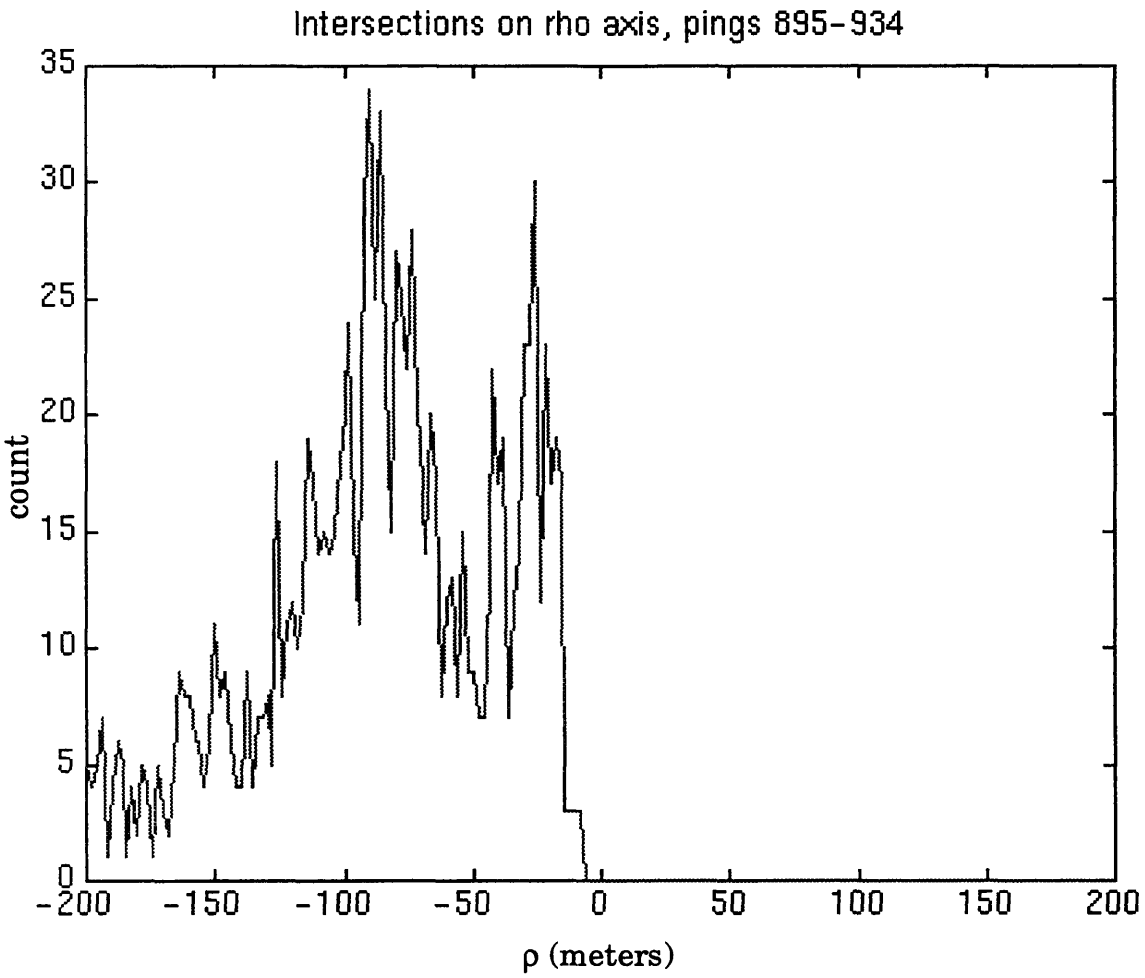

Figure 3-30 Accumulator Array at Rho Axis

The high number of detections and targets cause the most problems when attempting to complete the final step which is to determine the exact position of the targets from the peaks in the accumulator array. Figure 3-31 shows a plot of the range vs. ping number for the detections contributing to the peak at -24 meters. It is difficult to find the classic hyperbola shape in this image and thus determine the target location. Additional processing needs to be accomplished in order to increase the performance of the system. One option is to use the Hough Transform to find the hyperbolic shapes in the B-Scan data directly.

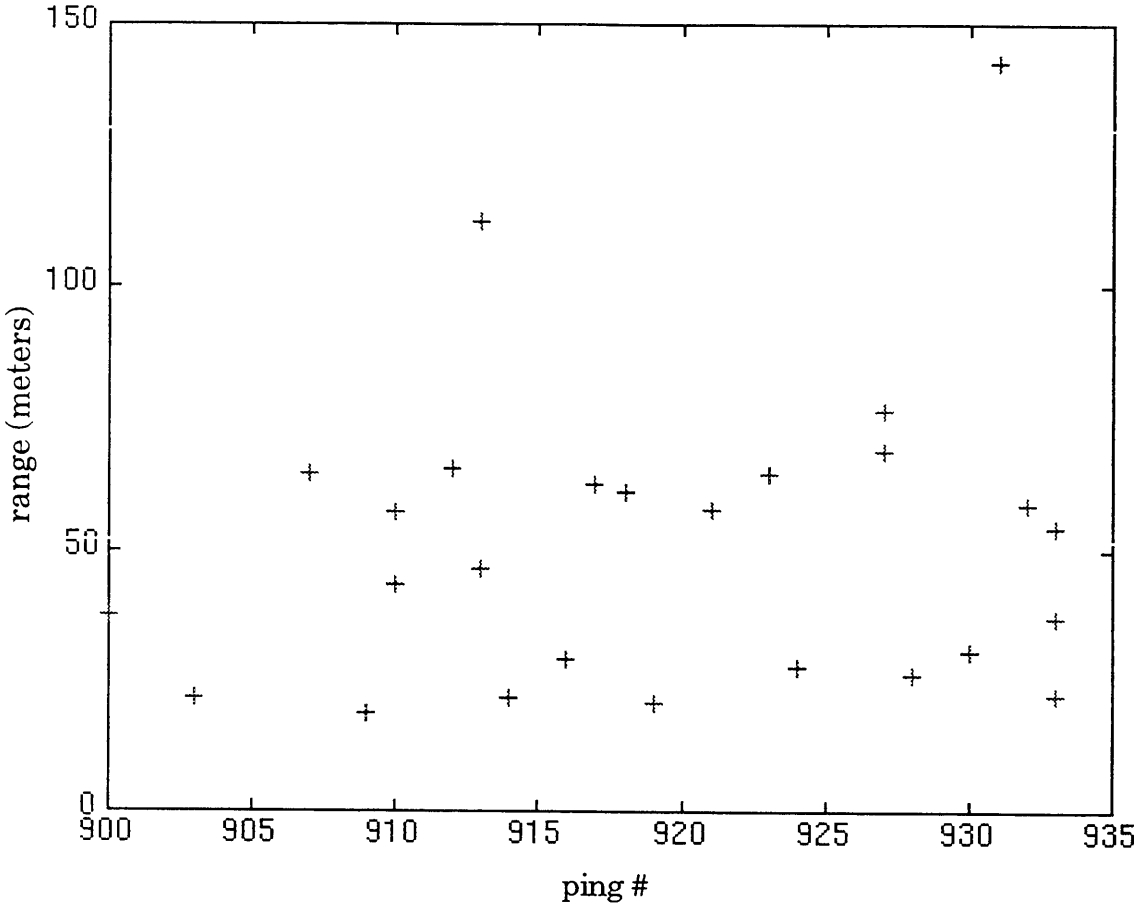

Figure 3-31 Range vs. Ping Number

4. Performance Analysis

Now that the algorithms have been defined, it is necessary to test how well they work and compare their relative advantages and disadvantages. Since the algorithms are designed for target localization, an obvious and highly critical test of performance is determining whether the targets are properly identified. Comparisons will also be made on several other key characteristics, such as resilience to noise and positional errors and the effects of detection thresholds.

4.1 Detection Capability

The ability to properly locate targets of interest is the most important measuring stick for these algorithms. Unfortunately, the ground truth knowledge of the target field at Mendum's Pond is not well known. While the approximate positions of several mine-like objects are known, the location and size of other sonar targets are unknown. This problem hampers attempts at quantifying the results. An analysis of the structure of the energy in the plane caused by both the noise alone case and the noise plus cylinder case will also be used to help determine performance capability.

There were five known targets of interest in the Mendum's Pond test range. These objects are of different sizes and shapes and are located both on the bottom of the lake and moored in mid-water column. These objects and their locations are listed in Table 3.

Target	Actual	Monopulse Energy Integration
Northwest	(2143,1783)	(2148,1787)
Southeast	(2266,1695)	(2268,1694)
Southwest	(2169,1679)	Not Located
-11 dB	(2270,1777)	(2270,1773)
-20 dB	(2230,1736)	(2231,1735)

Table 3 Target Localization Comparison

Table 1 shows that the sonobuoy seemed to locate the target positions quite accurately. The one exception is that the Southwest target was not found. This target also was not found in a side-scan survey of the target field. The map in Figure 4-1 shows several target locations which are denoted by the black arrows. This map was created using only 378 of the 977 pings for the run, because the map appears more cluttered as the number of pings increases. The -20 dB target does not appear in this map, but is found quite clearly using some of the remaining pings. Close-up maps of the areas surrounding each target are stored in the appendix as Figures A-2 through A-6. These maps were used to establish the locations listed in Table 1.

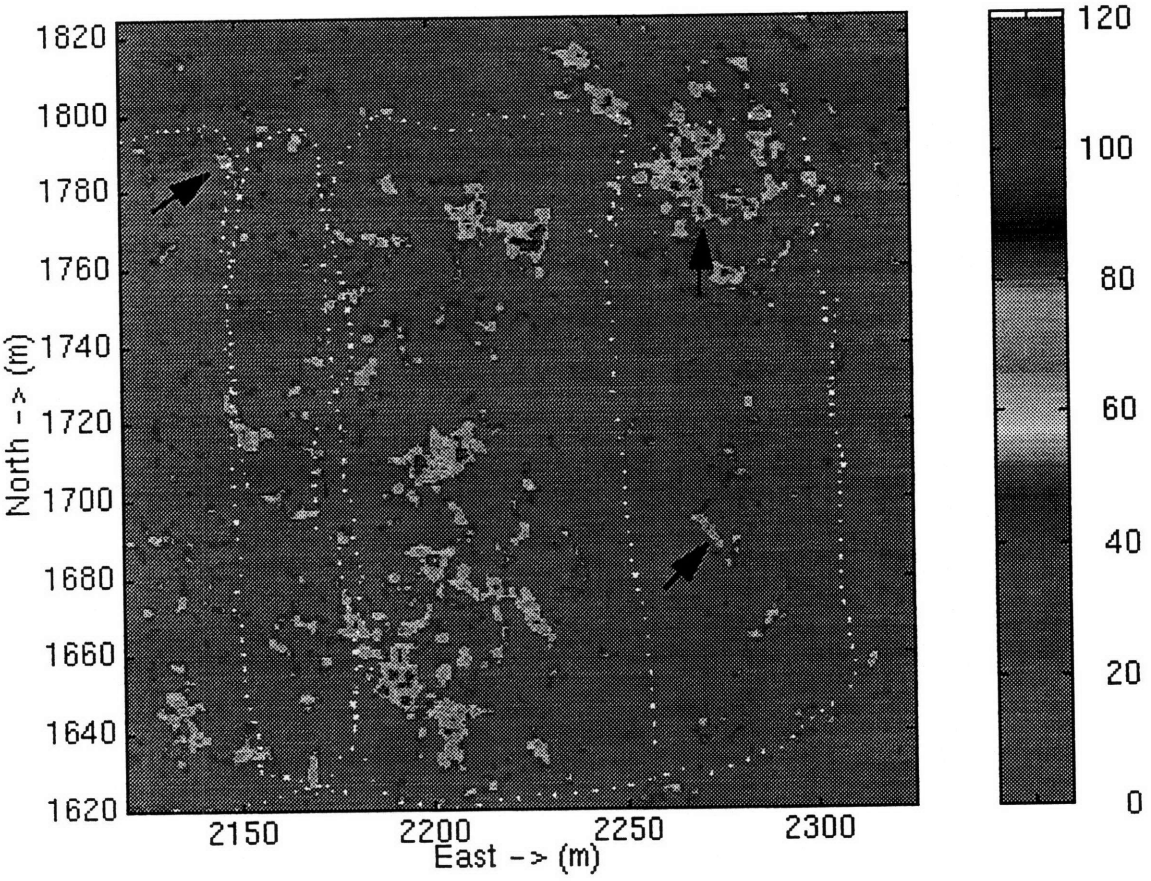

Figure 4-1 Energy Map of Overall Target Field

Another significant characteristic of the map in Figure 4-1 is the high number of sonar targets present. This problem has been addressed in previous

sections. Various methods have been adopted to reduce the interference between these targets, but the targets themselves remain. A side-scan sonar image of a segment of the target field is shown in Figure 4-2. While it is difficult to localize targets in this figure, areas of difficult topography are readily observed and these corroborate the results displayed in Figure 4-1. For example, the area from 2175 East to 2225 East and 1600 North to 1700 North is shown to contain a high number of clutter objects in both images. The Hough transform technique did not work well with the large number of targets and noise in the sonar environment. There were simply too many detections which created many collinear points that were not all related to the same target.

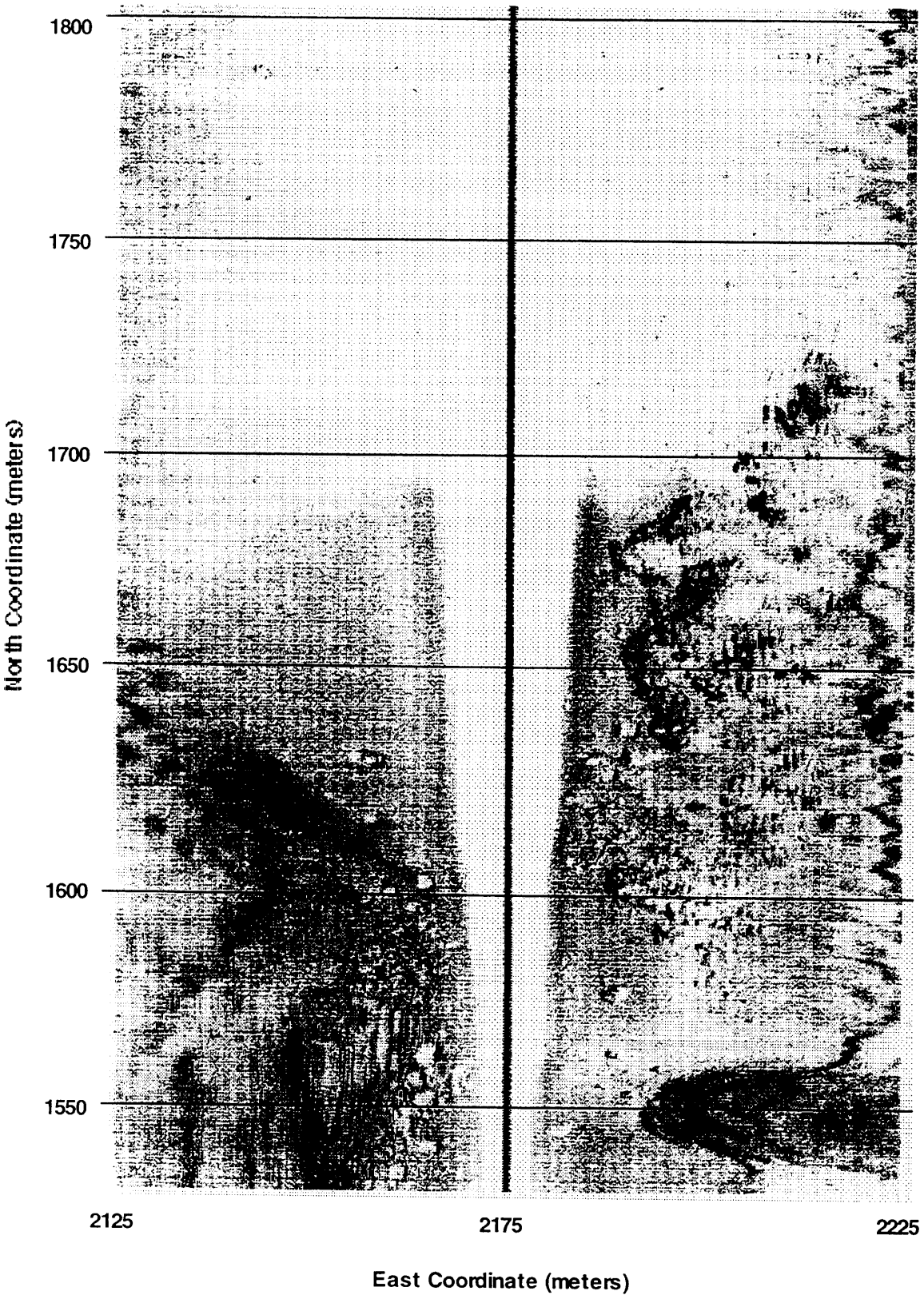

Figure 4-2 100 KHz Side Scan Survey of Target Segment

4.2 Energy Distribution

It is difficult to quantify the actual test results due to the significant amount of clutter objects, so additional analysis of the simulated data will be used to demonstrate the detection capability of the energy integration method. One way in which this can be done is through an analysis of the structure of the noise and targets in the energy plane. While the exact probability distribution regarding the nature of the energy is rather complex because of the number of targets, an approximation can be made using histograms of the energy in the plane for both the noise only and noise plus target cases. Figure 4-3 displays various histograms comparing the data for both cases. Separate plots are created for different detection thresholds. In each of these plots, the solid line corresponds to the noise only case, while the dashed line depicts the cylinder plus noise case. The image plane is a square with 1024 pixels per side and each pixel represents 0.2 meters. So, the resulting image is approximately 200 meters on a side. In creating the histograms, the monopulse energy integration algorithm was utilized with both the SNR limiting and beam filtering features turned on, as this configuration has produced the best results for detecting objects. These energy maps are contained in the appendix as Figures A-8 through A-15.

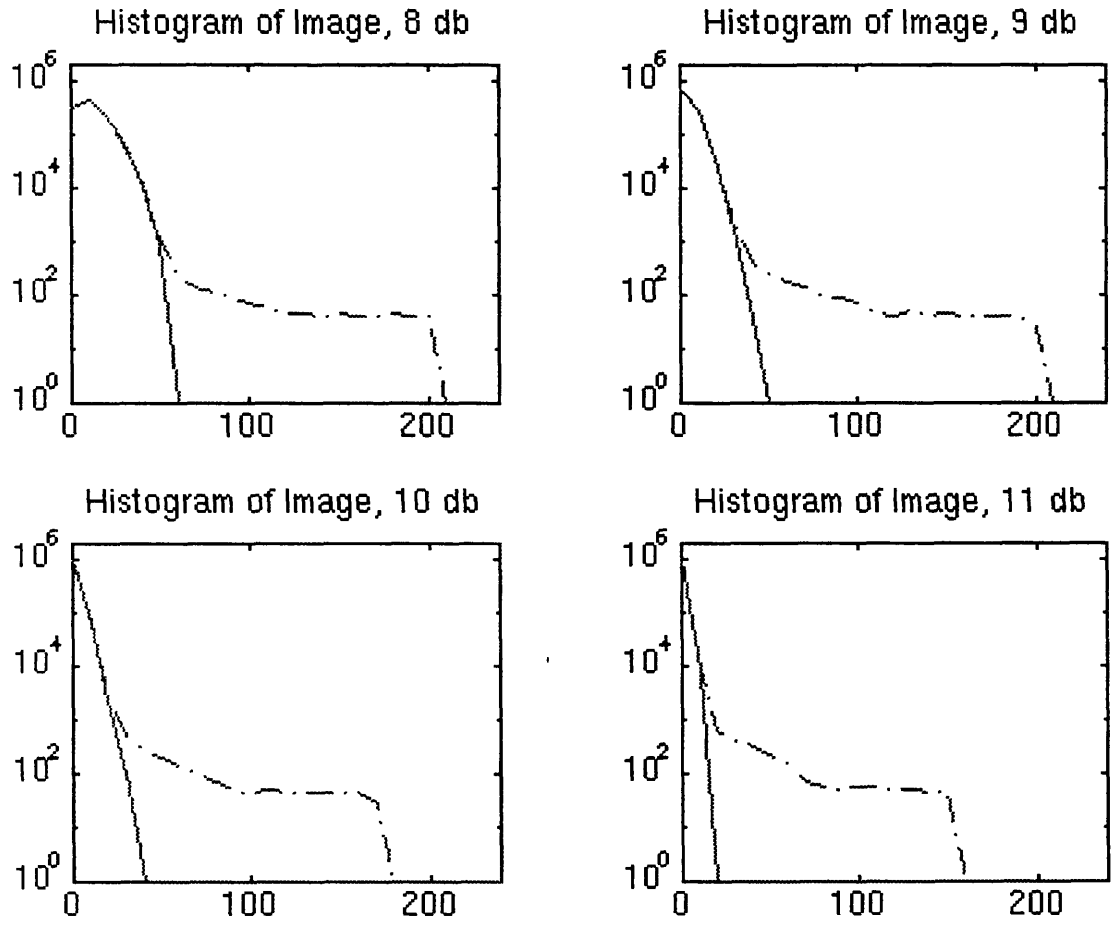

Figure 4-3 Histograms of Energy in Plane for Simulated Data

These images show remarkable differences between the two cases which simplify target detection tremendously. The peak values of the noise only case range from a high of 50.46 at 8 dB to only 10 at 12 dB. Incidentally, the maximum value at 11 dB is also only 10. This means that none of the arcs intersected at either level. The peaks values using the cylinder and noise case range from a high of 204.25 at 8 dB to 146.91 at 12 dB. Clearly, these results indicate the great integration gain which may be achieved using this technique. The number of detections used to construct the various images are listed in Table 2. The target plus noise case added between 40 and 70 detections for the 41 pings. Some of the additional pings are caused by multipath reflections. While these detections are not randomly distributed like the noise, the arcs due

to the multipaths do not intersect with each other because of the range separation.

SNR Threshold (dB)	*Noise Only*	*Cylinder and Noise*
8	6847	6905
9	1890	1963
10	334	392
11	47	96
12	5	46

Table 4 Number of Detections for Given Detection Thresholds

4.3 Map Parameters

Several parameters have an affect on the appearance of the map. These include the range variance, monopulse estimate variance, map threshold, and detection threshold. The range variance and monopulse estimate variance affect the shape of the arc. More accurately, the range variance affects how much the energy in a given pixel decreases due to the deviation from the measured range and the monopulse estimate variance controls the decrease in energy due to the deviation from the monopulse estimate. While these values are adjustable, typically they are set to reflect the model of the detection data.

The map threshold, or background threshold, does not affect the creation of the map, but is used to detect targets after the map has been created. The thresholded map images essentially display the result of the map threshold. After applying the threshold to an image, a local maximum routine would then be used to determine the peak locations.

The detection threshold has perhaps the greatest affect on map appearance. As the detection threshold is raised, the number of detections decreases drastically. This relationship is displayed in Table 4. A smaller number of detections considerably reduces the number of computations which

must be performed to create a map. This also decreases the storage requirements on the buoy and the amount of time necessary to uplink to a host platform. Also seen in Table 4 is that the proportion of detections associated with a target also increases with the detection threshold. This characteristic helps explain why the distance between the peak due to the target and the peak due to the background in the histograms of Figure 4-3 first increases as the detection threshold increases. Thus it would seem to be wise to set the detection threshold as high as possible.

A high detection threshold is not always desirable, however. Obviously, a high threshold may cause weaker targets to remain hidden. Figure 4-4 displays an energy map of the -11 dB calibrated sphere. The sphere location is denoted by the arrow. Figure 4-5 is a plot of the same area, except in this plot the detection threshold has been raised from 8 dB to 12 dB. The calibrated sphere has disappeared from view. Spherical objects, such as in the plots just mentioned, are characterized by a uniform return instead of strong detections in any particular direction. While the peak target strength may be lower than for a similarly sized cylinder, the integration gain is much higher. For a target such as this, a lower threshold works better. Thus a tradeoff exists on where to place this threshold. The optimum position allows a majority of target information to pass, while at the same time restricting the background noise. The exact location will depend on the desired probability of false alarm and probability of detection values. More experimentation in a cleaner sonar environment is necessary to determine this location.

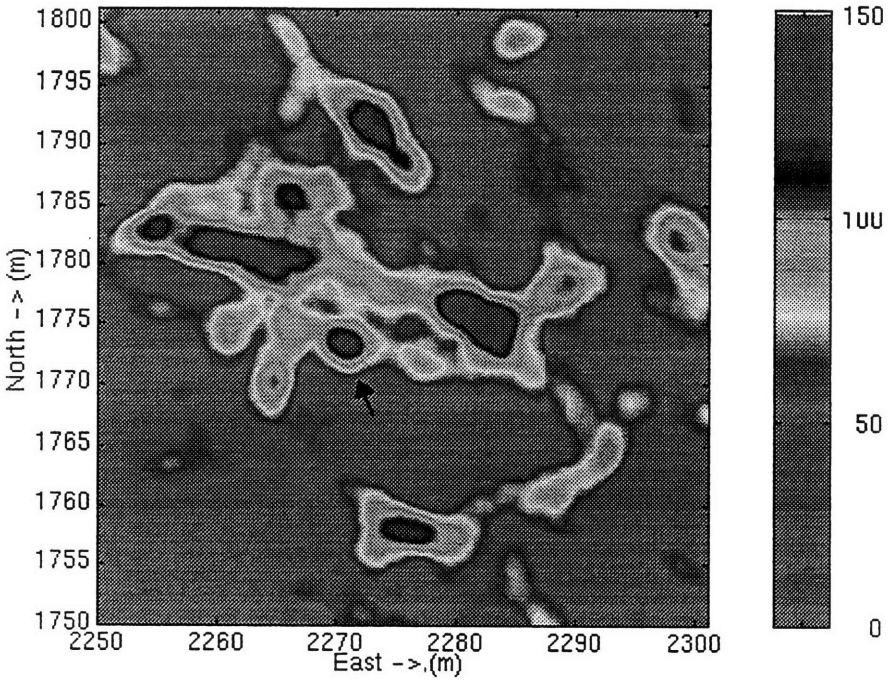

Figure 4-4 Detection Threshold: 8 dB

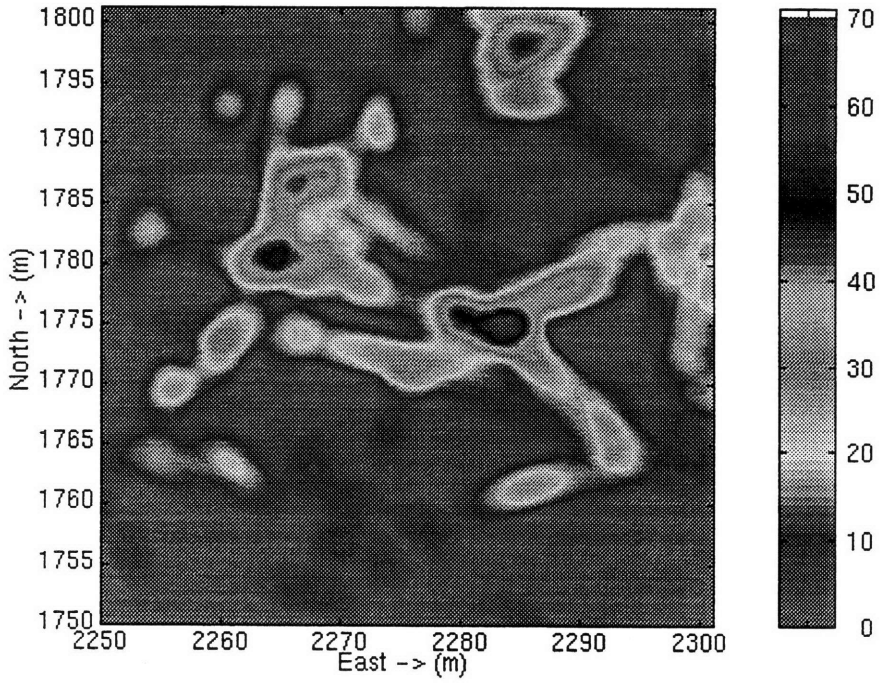

Figure 4-5 Detection Threshold: 12 dB

A similar tradeoff exists for the Hough transform. Several graphs showing the effect of the detection threshold on performance are shown in

Figure 4-6. These plots are all based on the same set of detections from the cylinder simulation used in section 3-4. As the threshold drops lower and the number of detections increases, the performance of the Hough transform decreases dramatically. A larger number of detections at a range close to the buoy creates a second peak which at 8 dB completely overshadows the desired peak at - 50 meters. From this data, the Hough transform does not appear to be as noise resilient as the maximum-likelihood method.

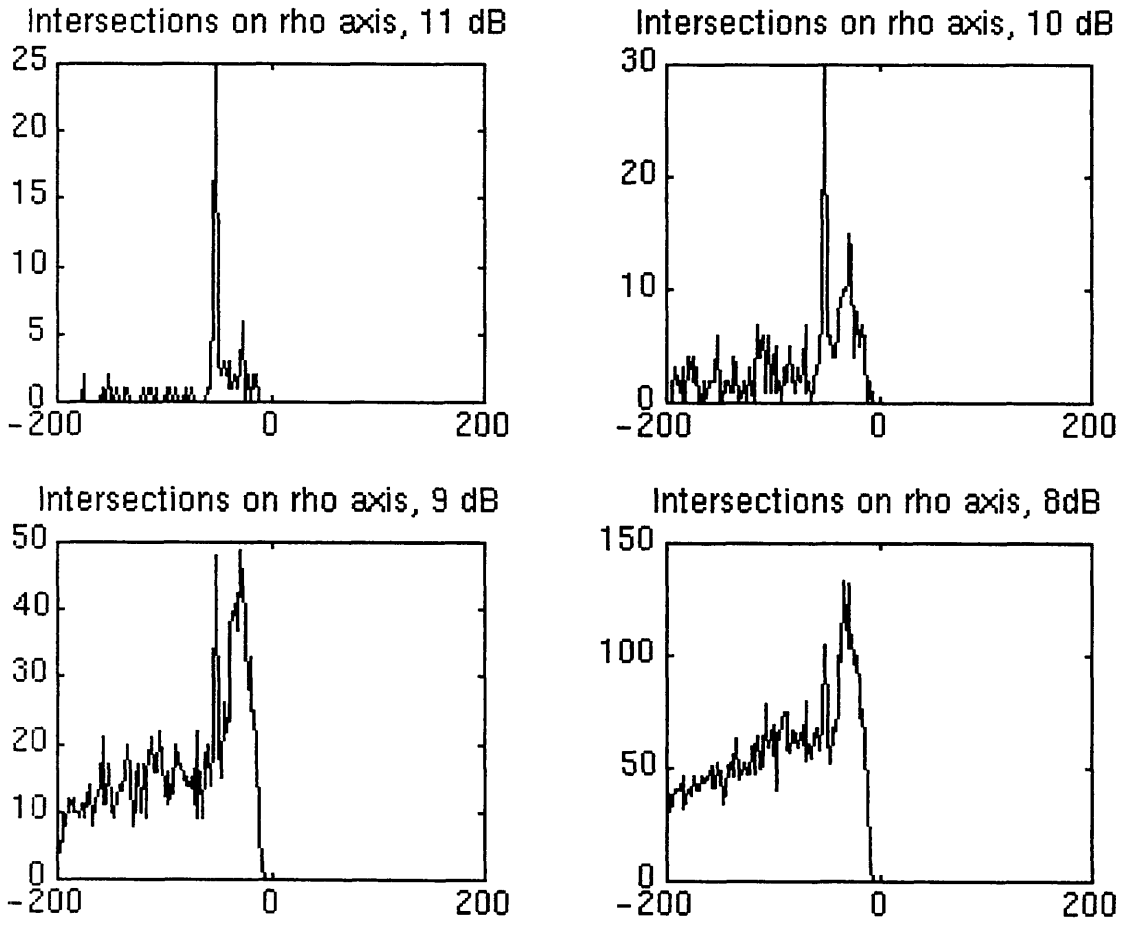

Figure 4-6 Effect of detection threshold on Hough transform

5. Conclusions

In response to shortcomings in current mine reconnaissance techniques, the Charles Stark Draper Laboratory developed a concept for a sensor platform called Intelligent Sonobuoy to detect and localize mines and mine-like objects. This sonar system is unique in that it uses a low frequency, wide azimuth sonar projector and cylindrical receive array. In addition, the sonobuoys themselves contain on-board processing to allow them to create lists of detections and map their surroundings. Detecting and localizing targets requires a fusion algorithm which takes into account the various characteristics of the data.

An algorithm based on maximum-likelihood techniques has been developed to process the detection lists. This algorithm amounts to integrating the energy contribution of each detection in an x-y plane of the target field. As the sonobuoy moves through the field, multiple detections of the same object tend to peak in one location, while detections attributed to background noise are spread evenly throughout the plane.

The theoretical results are supported with actual test data obtained during the summer and fall of 1994. While problems caused by inaccuracies in the GPS system reduced the effectiveness of the algorithm, it still proved to be robust enough to locate the desired targets. A high number of sonar targets also hampered the effectiveness of the algorithm; however, modifications which reduced the effective size of the arcs in the plane minimized the interference caused by those targets and allowed finer target resolution in the map domain.

The Hough transform was next studied as a competing approach. The Hough transform is similar in that it too involves accumulating the detections which pass through a given location. The Hough transform, though, assumes that the arcs are infinitely long and does not take into account the probability distributions which describe the data. While this technique worked for simulated data in a relatively clean sonar environment, the Hough transform

was not as able to accurately process the large number of detections found in the actual test data.

5.1 Future Work

The results to date from using the Intelligent Sonobuoy system have been promising, but future work needs to be performed to fully validate the concept. Chief among these would be to test in a sonar environment in which a more precise ground truth knowledge of sonar targets is known. This would allow the various error sources to be quantified and thus better study the effects of those errors. Exact knowledge of target locations and orientations also helps quantify the performance of the system and enables a more complete analysis of the tradeoffs concerning the detection threshold.

Another major step which is yet to be performed is classification of the various sonar targets. Ideally, this process differentiates between mine-like sonar targets and other clutter that had a high enough target strength to be detected. The shape of the target in the energy domain has already been described as a possible method. In addition, the measured target strengths associated with a mine-like target should be comparable to its theoretical model and have a definite structure, as opposed to the more random target strengths associated with rocks and other natural objects. The structure of the sonar reflection in the vicinity of the detection also provides clues as to the identity of the target.

Lastly, additional work is yet to be done with the Hough transform. Although it was less robust in the noisy environment as implemented, several other ideas deserve attention. For example, the Hough transform could be used on the B-Scan data directly to find the characteristic hyperbolic shapes. Another option would be to look for the inverse tangent shape associated with the plot of aspect angle as a function of ping number. This graph should correspond to the B-Scan and provide an additional source of information.

Appendix A. Maps

Several energy maps are placed here in the appendix. These maps have been previously referenced in the body of the thesis and are located here because they provide a reference for the reader and are not essential for the positions that were made.

Figure A-1 is a map of the entire target field. The color map has been altered to have a greater affect in color printing. These color plots are helpful in identifying targets in the maps.

Figures A-2 through A-6 are maps surrounding each of the known target areas. The target of interest in each plot has been identified with an arrow. These maps were used to find the target positions listed in section 4-1. Figure A-7 is a three-dimensional view of the Southeast target. The great separation between signal and background noise is especially evident in this plot.

Figures A-8 through A-15 are energy maps using the simulated data. A pair of maps have been created for each of four different detection thresholds. For each detection threshold there is a plot of the noise only case and the cylinder plus noise case. These maps were used to create the histograms in section 4-2.

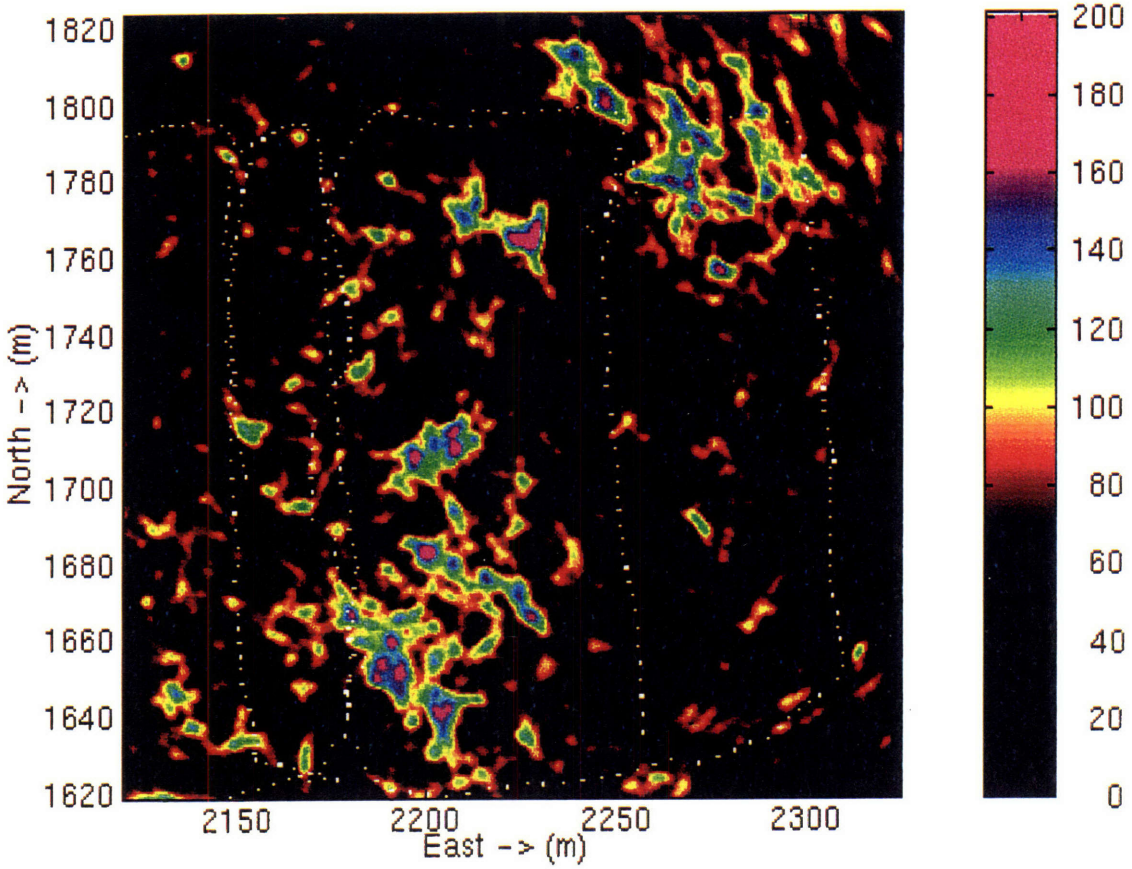

Figure A-1 Entire Target Field

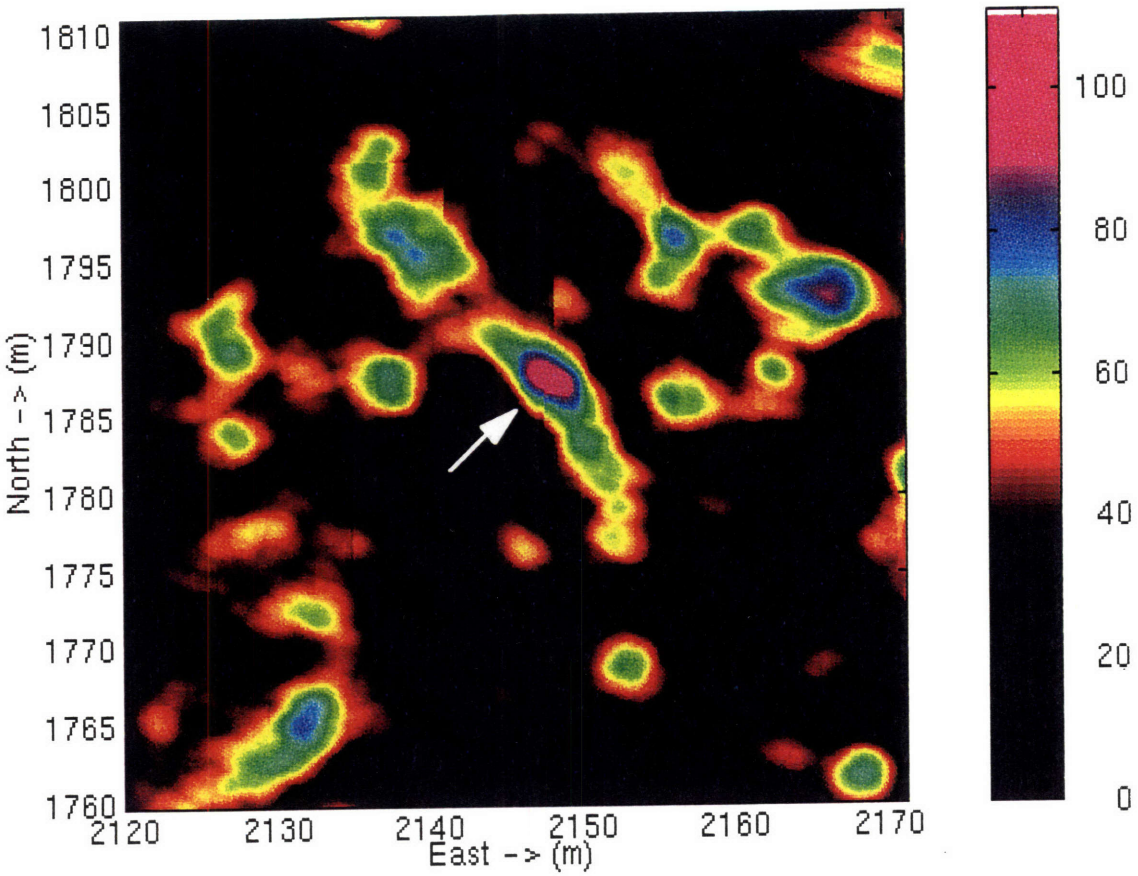

Figure A-2 Northwest Target

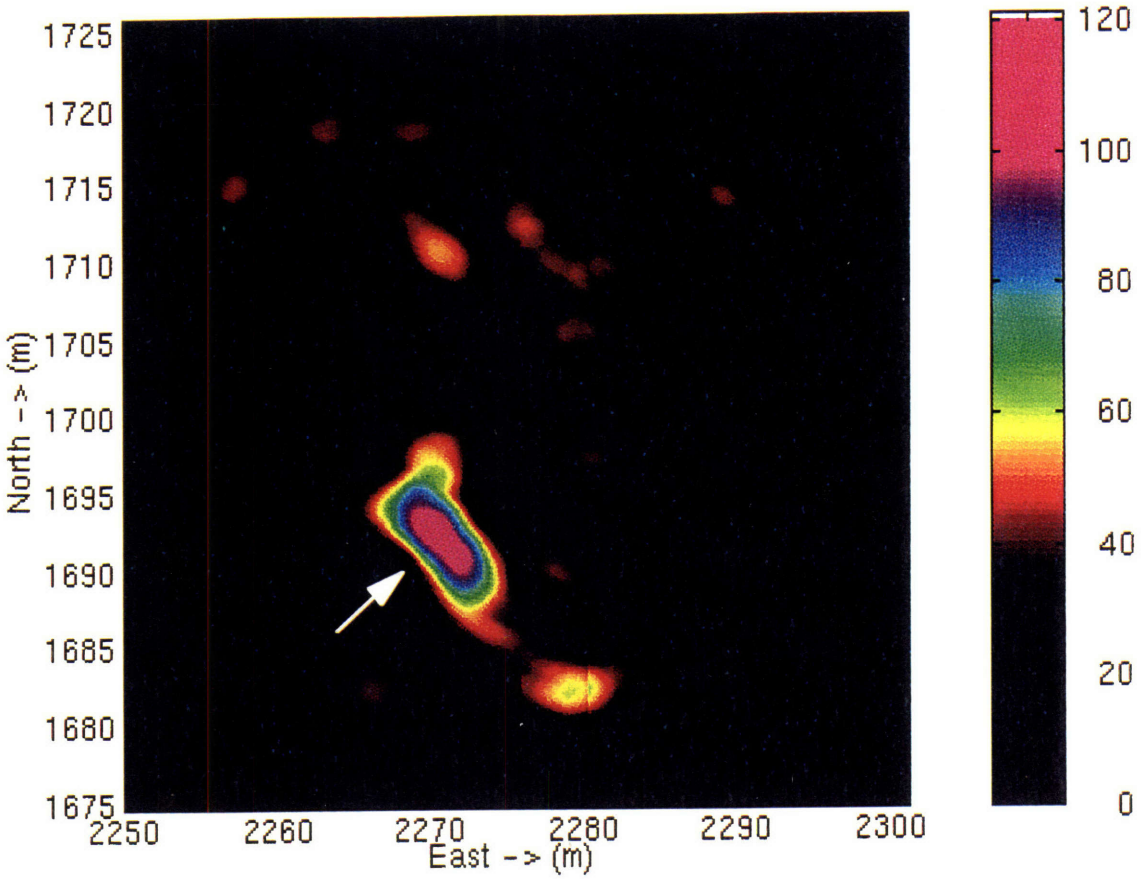

Figure A-3 Southeast Target

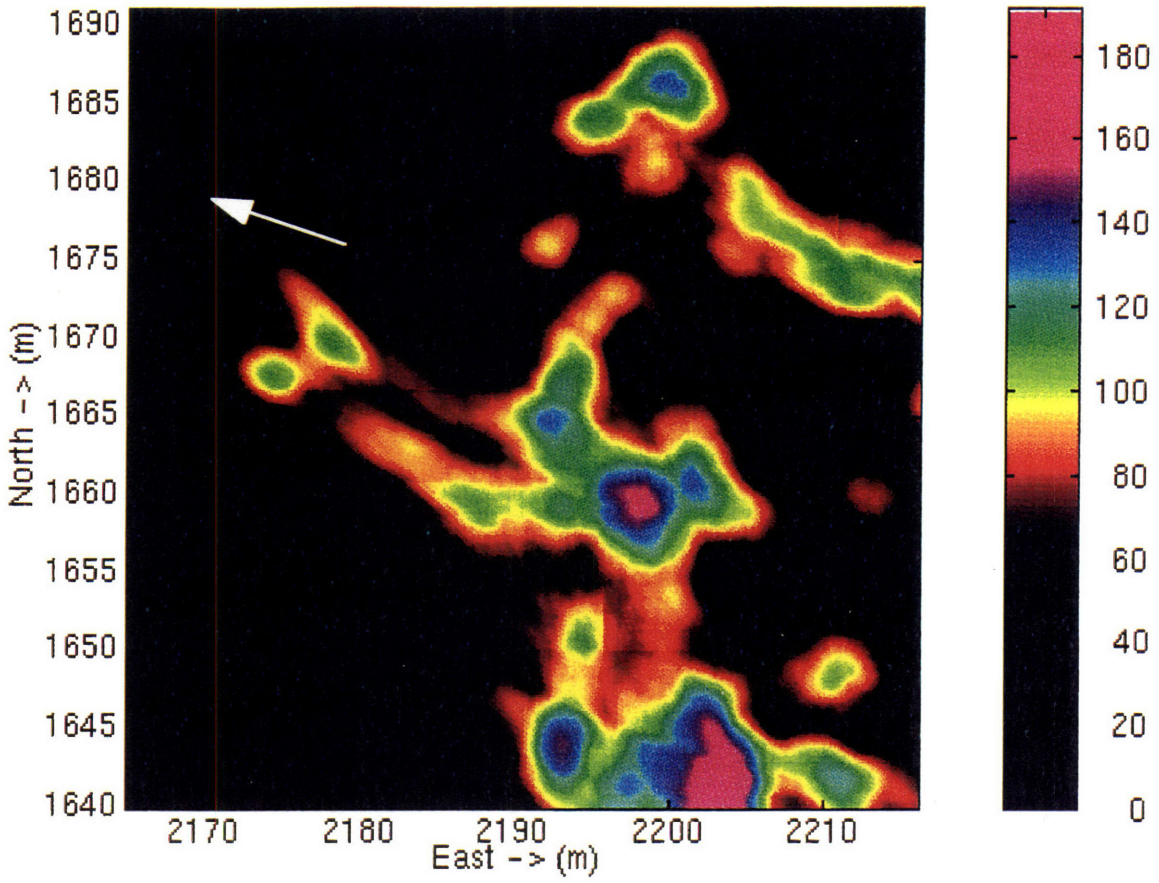

Figure A-4 Southwest target (Not Found)

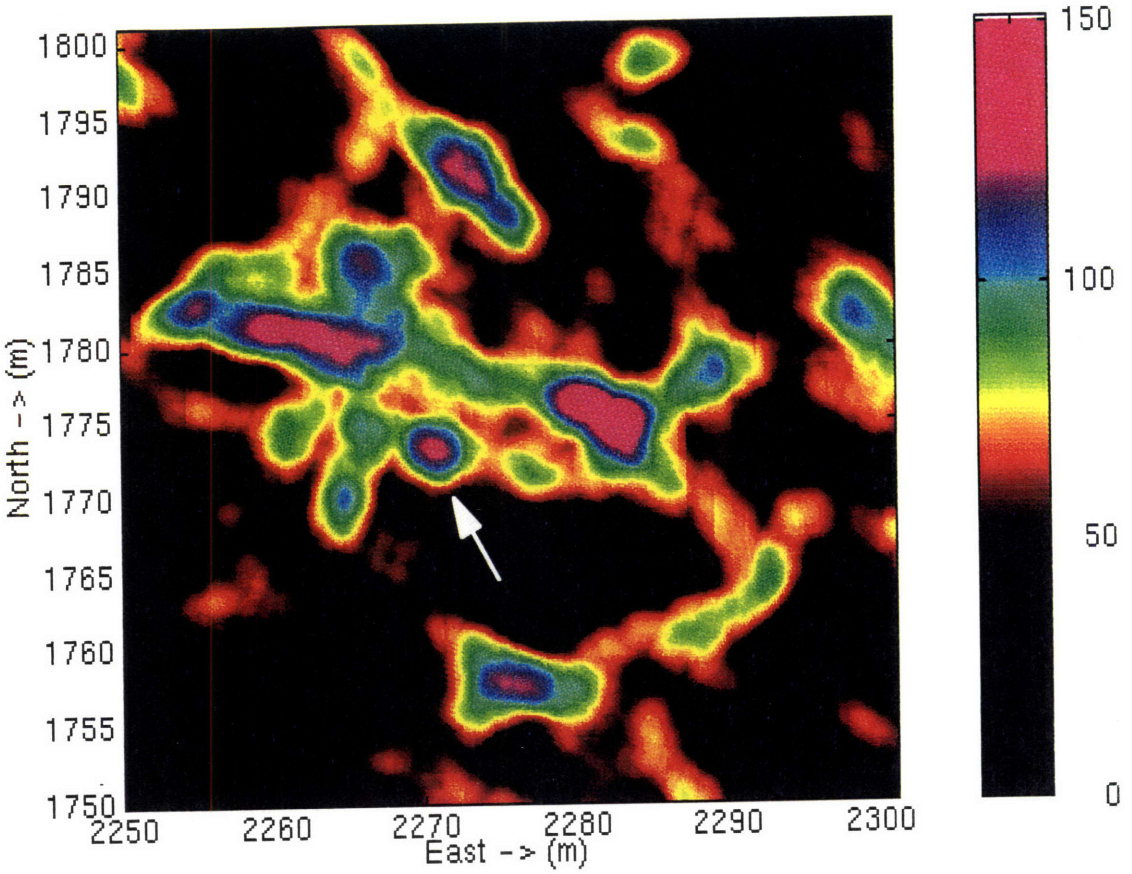

Figure A-5 Calibrated Target, -11 dB

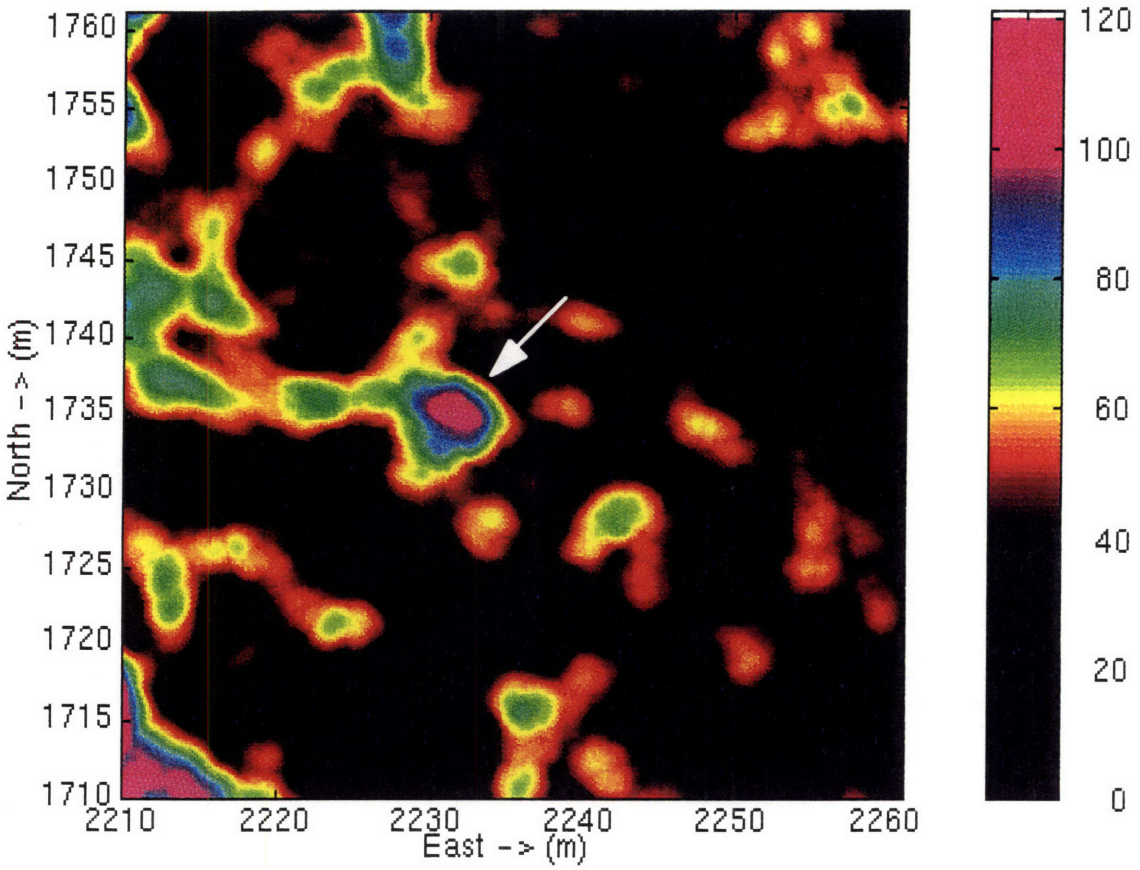

Figure A-6 Calibrated Target, -20 dB

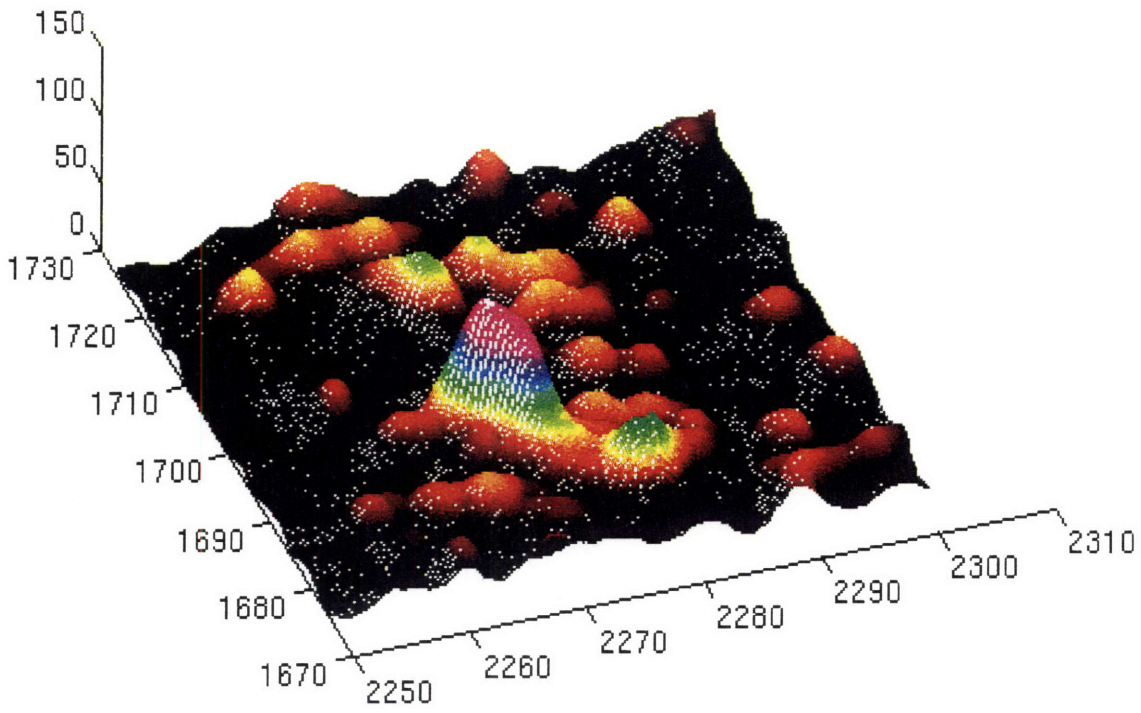

Figure A-7 Surface Plot of Southeast Target

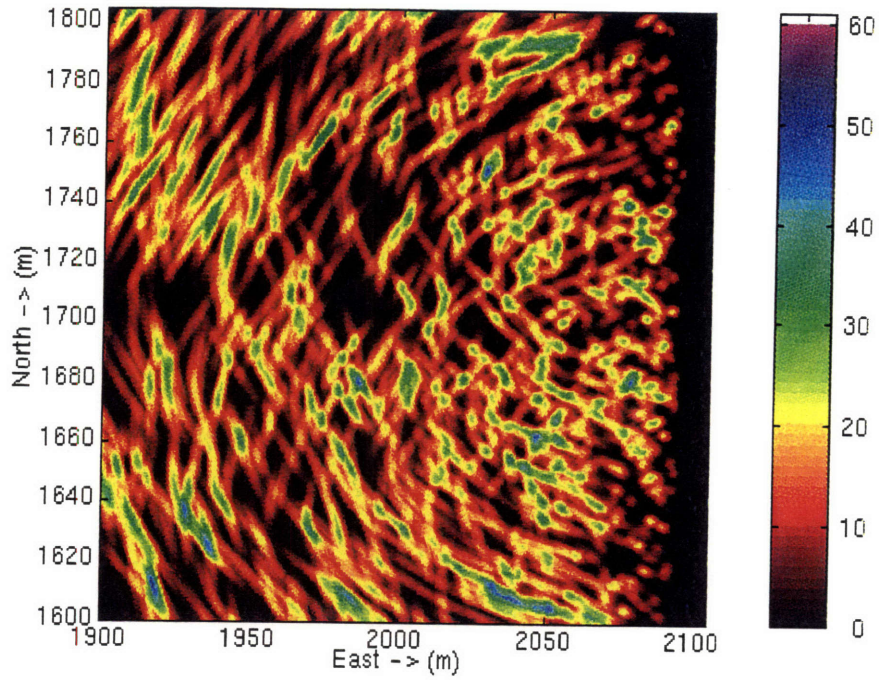

Figure A-8 Noise Only, 8 dB Threshold

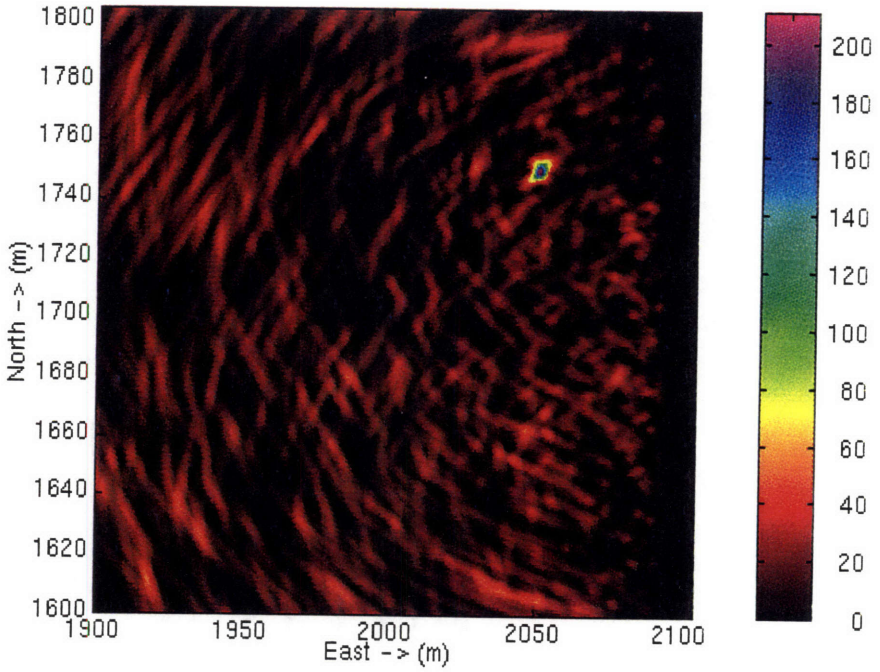

Figure A-9 Cylinder and Noise, 8 dB Threshold

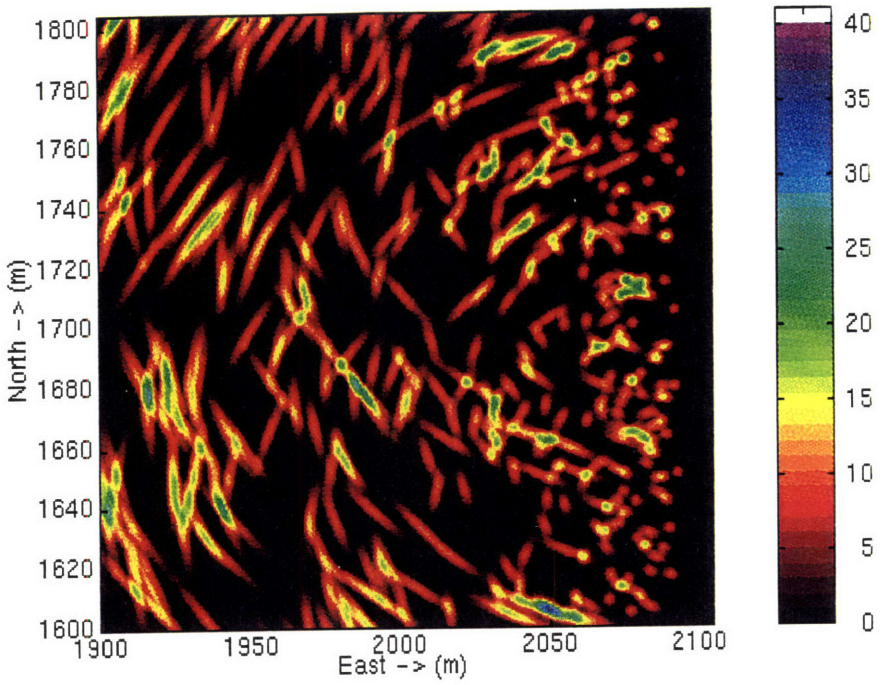

Figure A-10 Noise Only, 9 dB Threshold

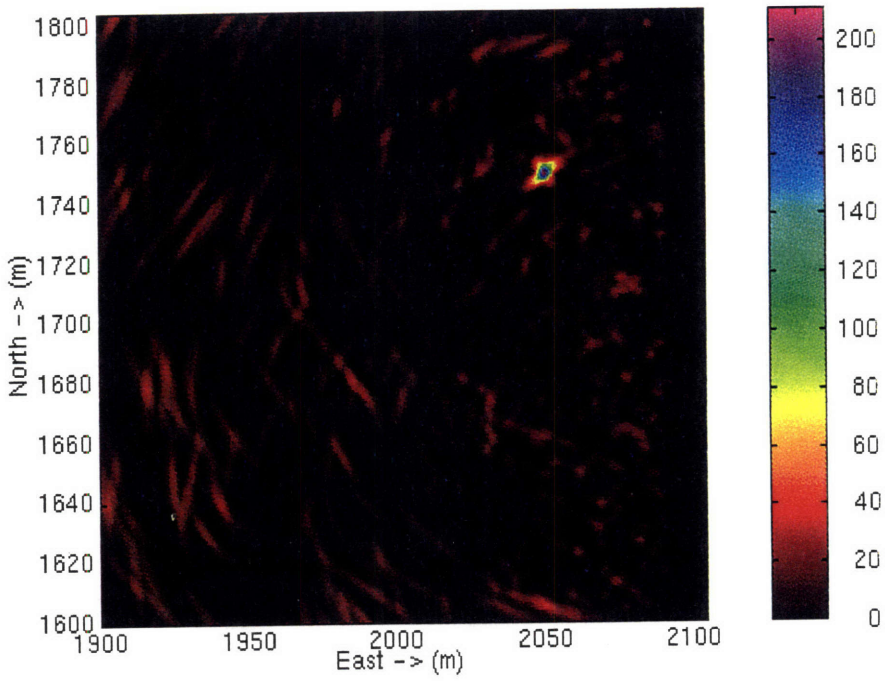

Figure A-11 Cylinder and Noise, 9 dB Threshold

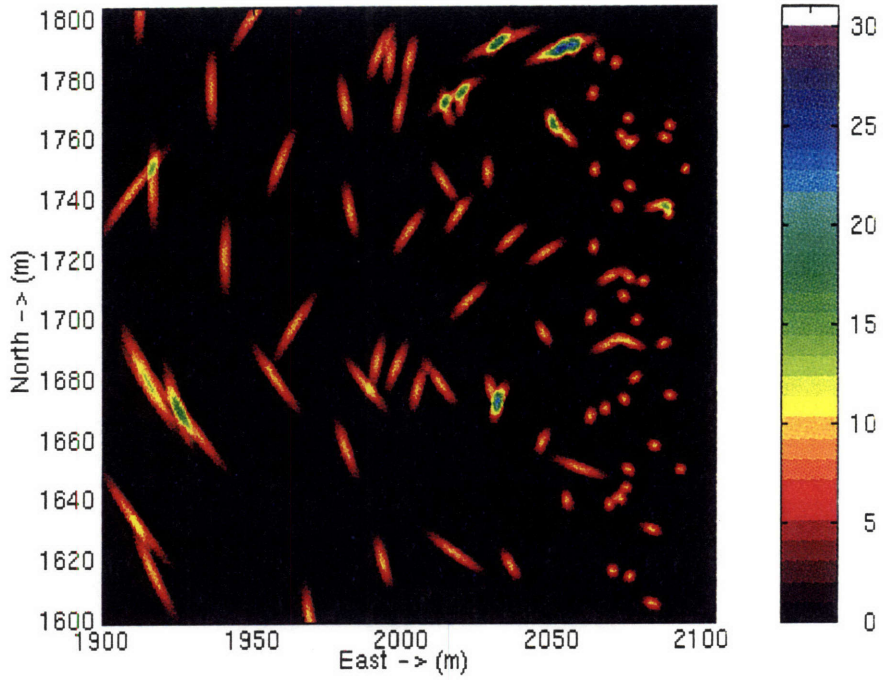

Figure A-12 Noise Only, 10 dB Threshold

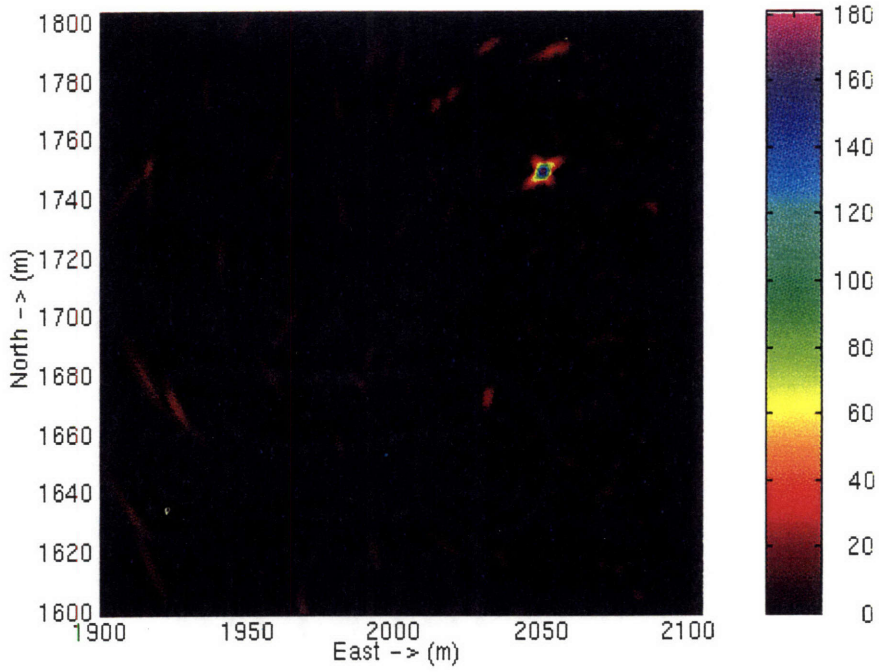

Figure A-13 Cylinder and Noise, 10 dB Threshold

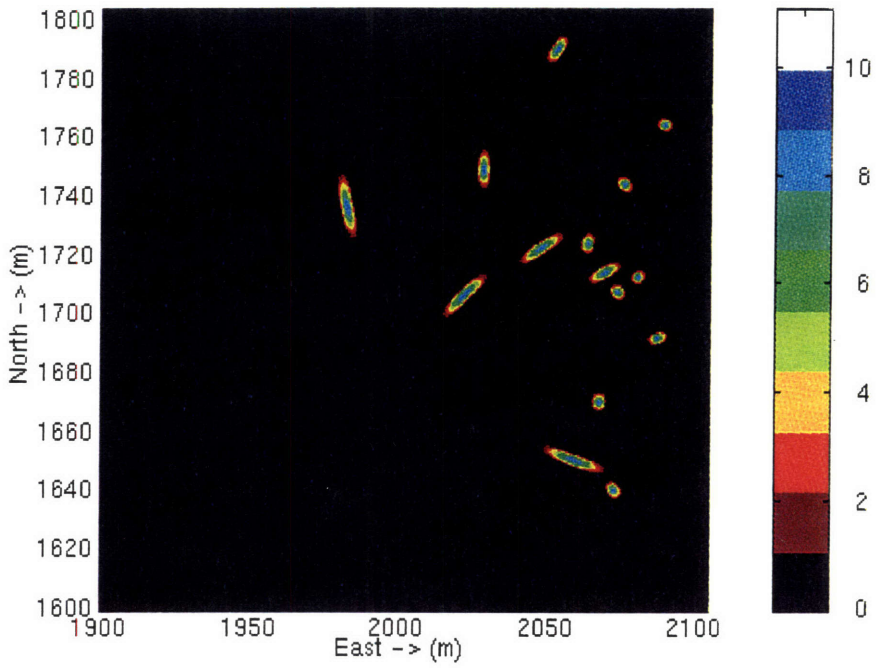

Figure A-14 Noise Only, 11 dB Threshold

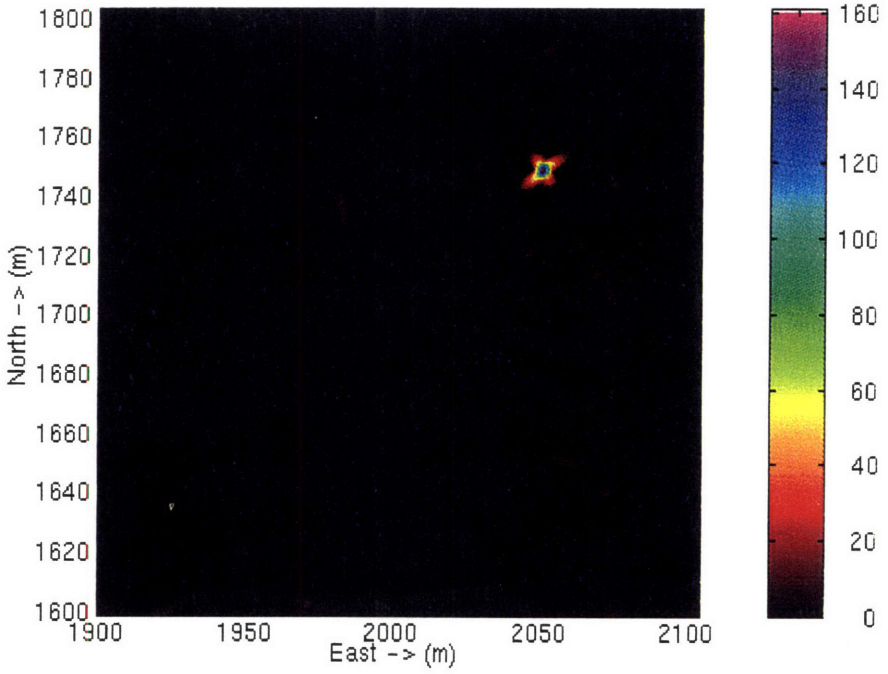

Figure A-15 Cylinder and Noise, 11 dB Threshold

Bibliography

[1] "U.S. Navy Mine Warfare Plan," Second Edition, Fiscal Year 1994-1995 Programs, February 1994.

[2] "Navy Ship 'Finds' Cleared Mines," Navy Times, March 4, 1991.

[3] "Intelligent Sonobuoy Interim Report," Global Associates, LTD, July 11, 1994.

[4] Houston, Kenneth M., and Engebretson, Kent R., "The Intelligent Sonobuoy System - A Concept for Mapping of Target Fields," CSDL Paper CSDL-P-3429, March 1995.

[5] Volberg, Bud, Herman, William A., and Kozak, Gary A., "Mine Warfare, Sonar & Unmanned Vehicles," 1993.

[6] Burke, Shawn, "Intelligent Sonobuoy Test Plan," CSDL Memorandum ETB-94-133, March 9, 1994.

[7] MSEL, "Mendums Pond Test Range Facility," Rev. May 1991.

[8] Urick, Robert J., *Principles of Underwater Sound*, 3rd Edition, New York: McGraw Hill, Inc., 1983.

[9] Houston, K., "Performance Analysis for a Wideband Monopulse Side-Scan Sonar," CSDL Memorandum ETB-93-166. May 7, 1993.

[10] Discussions with Mike McMahon, Navstar Engineer, June 1994.

[11] Waltz, E.L. and Llinas, James, *Multisensor Data Fusion*, Artech House, Norwood, 1990.

[12] Willet, Peter, Alford, Mark, and Vannicola, Vincent, "Detection Fusion with Similar Sensors," SPIE Vol. 1955, 1993.

[13] Smith, C. Ray, "A Bayesian Approach to Multisensor Data Fusion," SPIE Vol. 1699, 1992.

[14] Klein, Lawrence A., *Sensor and Data Fusion Concepts and Applications*, SPIE: Bellingham, Washington, 1993.

[15] Houston, K., "Performance Analysis for a Wideband Monopulse Side-Scan Sonar," CSDL Memorandum ETB-93-166, May 7, 1993.

[16] Illingworth, J. and Kittler, J., "A Survey of the Hough Transform," Computer Vision, Graphics and Image Processing, Vol. 44, 87-116, 1988.

[17] Duda, Richard O. and Hart, Peter E., "Use of the Hough Transformation to Detect Lines and Curves in Pictures," Communications of the Association of Computing Machinery, Vol. 15, 11-15, 1972.